Solution-Processed SnO_2 Electron Transport Layer: Advancement in Flexible Printed Perovskite Solar Cells

by

Muhammad Salman Kiani

A thesis is submitted in partial fulfilment of the requirement of the School of Science and Humanities, Nazarbayev University for the degree of Doctor of Philosophy in Physics

Supervisory committee:

Dr. Askhat Jumabekov, Nazarbayev University

Dr. Annie Ng, Nazarbayev University

Acknowledgements

In the name of Allah, the Most Gracious, the Most Merciful, who has taught man the use of the pen and granted knowledge of what was previously unknown. I am deeply grateful to everyone who has inspired and supported me throughout my PhD journey.

First and foremost, my heartfelt thanks go to my supervisor, Professor Askhat Jumabekov, and my co-supervisor, Professor Annie Ng, whose guidance and insightful feedback have been invaluable throughout this research journey. I am especially thankful to Professor Askhat Jumabekov for providing the necessary research facilities and financial support that enabled me to embark on, conduct, and complete my PhD. His mentorship and unwavering support have been instrumental in shaping the direction of my research and enhancing my understanding of the subject. His assistance in writing, refining, and publishing articles based on my research has been particularly beneficial. I am also deeply appreciative of Professor Annie Ng, whose expertise and critical feedback have significantly contributed to the depth and rigor of this thesis. Her dedication to academic excellence and continuous encouragement has been a constant source of motivation.

I would also like to extend my sincere gratitude to all my friends who have played significant roles throughout my academic journey. I am profoundly thankful to Abu Bakar Bhai, Rizwan Muneer Bhai, Basit Gulzar Bhai, Aidar Kemelbay, Marat Kaikanov, and Hryhorri Parkhomenko, who have been inspirational researchers and mentors. A special thanks to Abu Bakar Bhai for encouraging me to join an international university, which provided me with valuable research exposure, and to Rizwan Muneer Bhai, who has been a guiding force since I arrived in Astana. My first research partners, Aidar and Marat, have been an integral part of my initial research experiences, while Hryhorri, as my longest-serving colleague, has been a constant source of kindness and support. I am also grateful to my roommate Alshyn Abduvalov, along with my labmates, particularly ‘Rodnoy’ Alibek Kakim and Zhandos Sadirkhanov, and all my

colleagues, for their companionship and collaboration. At this stage, I missed my beloved friend Hafiz Shamsher ul Islam (Late), who was with me when I was travelling to Astana for the first. May Allah grant him the highest place in Jannah and bring his family peace and comfort, Ameen.

Pursuing a PhD is not solely dependent on individual effort; it is also shaped by the support and environment provided by those around you, both inside and outside the lab. I am fortunate to have had Professor Abdul Wahab as a mentor during this time. The time I spent working with him was one of the most productive phases of my life. His guidance instilled in me the motivation to work diligently, achieve meaningful results, and continuously strive for self-improvement. During the final stages of my PhD, particularly the thesis writing process, the time spent with Professor Zohaib Latif was filled with valuable learning experiences, for which I am sincerely thankful.

With this, I would like to thank the Chair of Physics Department, whole faculty, and the staff for their support. The support I received from the entire Department of Physics at Nazarbayev University has been invaluable, particularly from Professor Ernazar Abdikamalov, the Director of Graduate Programs of the Physics Department, whose dedication to guiding all graduate students is truly commendable. I wish him all the best in his future endeavors. My thanks also go to Maulen Yergaziyev, Kasym Khan, and Sandra Real for their professionalism and tireless efforts in assisting international students. Their dedication to their work has ensured that we never felt far from home.

Above all, I owe my deepest gratitude to my mother, whose prayers and unwavering support have been the cornerstone of all my achievements. Her love and encouragement have been an immeasurable blessing in my life. I am also grateful to my siblings for their constant involvement and support. I would like to honor the memory of my grandmother, Miss Khalida Begum. Her prayers have been a guiding force in my life, and I will always cherish her memory. This accomplishment would not have been possible without her influence and would be incomplete without her presence. May Allah grant her the highest place in Jannah. Ameen.

I would like to express my deepest gratitude to all my teachers and mentors who have guided me throughout my academic journey. Their wisdom, dedication, and encouragement have been instrumental in shaping my knowledge and skills. I am also profoundly grateful to be part of all of these institutions, for providing me with a nurturing environment that fostered my growth both academically and personally. The support and resources offered by the institutions have been crucial to the successful completion of this work.

Lastly, I would like to acknowledge the significant role of the Rahimia Institute of Quranic Sciences in shaping my commitment to using my abilities for the betterment of humanity. The institute has instilled in me the understanding that life's true purpose is to make a positive impact on others, a lesson that continues to inspire my efforts to work with sincere intentions for the greater good.

Abstract

The burgeoning field of flexible and printed perovskite solar cells (PSCs) presents a promising future for renewable energy applications, especially in wearable electronics and smart infrastructure. Realizing their potential hinges on developing functional layers processed at low temperatures. Due to its favorable properties, tin oxide (SnO_2) has emerged as a potential material for the electron transport layer (ETL). This study delves into synthesizing and utilizing SnO_2 quantum dots (QDs) for ETL fabrication in flexible and printed PSCs.

SnO_2 QDs are synthesized via a solvothermal method and formulated into aqueous and printable ETL ink solutions with varying QD concentrations. The electrical conductivity of the resultant ETL films largely depends on the concentration of SnO_2 QDs in the ETL inks. A compact layer of SnO_2 QD-based ETL can facilitate effective electron transfer from the perovskite layer to the transparent conducting oxide (TCO) layer in PSCs. Achieving an ideal thickness of SnO_2 QD-based ETL can reduce charge recombination losses and increase charge extraction efficiency in PSCs, thus improving the overall performance of devices. PSCs are fabricated on flexible plastic substrates using the slot-die coating technique. Notably, ETLs fabricated using 2 wt.% SnO_2 QD inks exhibit superior performance, yielding high mean power conversion efficiency (PCE) and showcasing a champion device with 10% PCE. This investigation underscores the potential of SnO_2 QDs for the scalable production of PSCs.

Despite the prevailing use of SnO_2 nanoparticle (NP) dispersion solutions in current PSC manufacturing processes, a comparison is made between the as-synthesized SnO_2 QDs-based ETL and the SnO_2 NP-based ETL inks. Our findings reveal an 11% enhancement in average device performance, attributed to SnO_2 QD-based ETLs' ability to reduce trap states in the perovskite layer and facilitate charge extraction.

In conclusion, this scientific work emphasizes the transformative potential of SnO_2 QDs in advancing flexible and printed PSC technology. The study contributes to the fundamental

understanding of PSCs and paves the way for practical applications in renewable energy generation. Continued research in this domain promises to propel the development of sustainable energy solutions and shape the future of solar technology.

List of Publications

Published

Kiani, Muhammad Salman, Zhandos T. Sadirkhanov, Alibek G. Kakimov, Hryhorii P. Parkhomenko, Annie Ng, and Askhat N. Jumabekov. "Solution-processed SnO_2 quantum dots for the electron transport layer of flexible and printed perovskite solar cells." *Nanomaterials* 12, no. 15 (2022): 2615. (Chapter # 4)

Kiani, Muhammad Salman, Hryhorii P. Parkhomenko, Mayuribala Mangrulkar, Sabina Aigarayeva, Assylan Akhanuly, Erik O. Shalenov, Annie Ng, and Askhat N. Jumabekov. "Stepping toward portable optoelectronics with SnO_2 quantum dot-based electron transport layers." *ACS omega* 8, no. 23 (2023): 21212-21222. (Chapter # 5)

Azamat, Aidana K., Hryhorii P. Parkhomenko, **Muhammad Salman Kiani**, Annie Ng, and Askhat N. Jumabekov. "Self-Powered Printed Flexible Bifacial Perovskite Photodetector." *ACS Applied Optical Materials* 2, no. 1 (2023): 149-157.

In progress

Reduced hysteresis of SnO_2 QDs-based ETL via UV-ozone treatment for application in scalable and flexible optoelectronics.

Table of Contents

List of Acronyms

4 tBp	4-tert-butylpyridine
ACN	Acetonitrile
Ag	Silver
Al	Aluminium
a-Si	Amorphous silicon
Au	Gold
BSE	Backscattered electrons
CB	Chlorobenzene
CdTe	Cadmium telluride
CIGS	Copper indium gallium (di)selenide
DI	De-ionized
DSSC	Dye-synthesized solar cell
EDX	Electron dispersion X-ray spectroscopy
EQE	External quantum efficiency
ETL	Electron transport layer
FA	Formamidinium
FF	Fill factor
FPSCs	Flexible perovskite solar cells
FTO	Fluorine-doped tin oxide
FWHM	Full width at half maximum
HPSC	Hybrid perovskite solar cell
HTL	Hole transport layer
ICDD	International center diffraction data
IPA	2-Propanol

ITO	Indium tin oxide
JCPDS	Joint committee on powder diffraction standards
J_{sc}	Short-circuit current density
J-V	Current density-voltage
LEDs	Light-emitting diodes
Li-TFSI	Bis(trifluoromethane)sulfonimide lithium salt
MA	Methylammonium
MAI	Methylammonium iodide
MoO_x	Molybdenum oxide
NASA	National aeronautics and space administration
NP	Nanoparticle
OCVD	Open-circuit voltage decay
OPV	Organic photovoltaic
PET/ITO	Poly(ethylene terephthalate)/indium-doped tin oxide
P3HT	Poly(3-hexylthiophene)
PCE	Power conversion efficiency
PEEDOT:PSS	Poly(3,4-ethylenedioxythiophene) polystyrene sulfonate
PET	Poly(ethylene terephthalate)
PL	Photoluminescence
PSCs	Perovskite solar cells
PTAA	Poly[bis(4-phenyl)(2,4,6-trimethylphenyl)amine]
PV	Photovoltaic
PW	Petawatt
QDs	Quantum dots
R_s	Series resistance
R_{sh}	Shunt resistance

SCLC	Space-charge-limited current
SDC	Slot-die coated/Slot-die coating
SEM	Scanning electron microscopy
SnO_2	Tin oxide
Spiro-MeOTAD	2,2',7,7'-Tetrakis[N,N-di(4-methoxyphenyl)amino]-9,9'-spirobifluorene
TCO	Transparent conducting oxide
TEM	Transmission electron microscopy
TiO_2	Titanium oxide
UNCTAD	United nations conference on trade and development
UNFCCC	United nations framework convention on climate change
UV	Ultraviolet
UV-Vis	Ultraviolet-Visible
V_{oc}	Open-circuit voltage
XPS	X-ray photoelectron spectroscopy
XRD	X-ray diffraction
ZnO	Zinc oxide

List of Figures

List of Tables

Chapter#1

Introduction

1.1. Background

The world is witnessing an unprecedented surge in energy demand driven by population growth and industrialization. According to the United Nations Conference on Trade and Development (UNCTAD), the global population surpassed 8 billion people by mid-November 2022, marking a staggering increase of 1 billion individuals since 2010, with developing nations playing a pivotal role in this demographic shift.[1] To meet the energy requirements of this burgeoning population, reliance on fossil fuels has intensified significantly. However, this reliance comes at a considerable cost to the environment. National Aeronautics and Space Administration's (NASA) research indicates an alarming average rise in the Earth's temperature, currently recorded at approximately 1.1 °C.[2] This temperature escalation has precipitated a myriad of natural calamities, including heightened temperatures, rising sea levels, and the accelerated melting of glaciers, culminating in widespread flooding.[3] An enduring consequence of the Industrial Revolution, dating back to the 18th century, is the phenomenon of global warming.[4] The combustion of fossil fuels releases significant amount of carbon dioxide into the atmosphere, exacerbating the greenhouse effect and consequently driving global warming. This phenomenon not only engenders adverse climate changes but also catalyzes the onset of various diseases, profoundly impacting life on Earth.

In response to these pressing environmental challenges, international accords have been forged to curb greenhouse gas emissions and mitigate long-term climate change. The Kyoto Protocol, implemented by the United Nations Framework Convention on Climate Change (UNFCCC) in 2005, aimed to curtail emissions. Subsequently, the landmark Paris Agreement was ratified with the primary objective of limiting the global temperature increase to below 2 °C, with aspirations

to restrict it even further, ideally to 1.5 °C.[5,6] Despite concerted efforts, projections suggest that cumulative carbon dioxide emissions are poised to surpass decarbonization targets, emphasizing the imperative for more robust action.[7] Amendments to these agreements were introduced during the Doha Amendment in 2013, initiating a second commitment period extending from 2013 to 2020. Furthermore, Figure 1.1, sourced from Statista, illustrates the alarming trajectory of carbon dioxide emissions from energy generation via fossil fuels, emphasizing the urgency of transitioning to cleaner, sustainable energy alternatives.[8]

In summary, the escalating energy demand and concomitant depletion of fossil fuels have precipitated a global environmental crisis marked by rising temperatures, extreme weather events, and ecological disruptions. International agreements such as the Kyoto Protocol and the Paris Agreement serve as critical frameworks for collective action, yet more concerted efforts are requisite to avert the looming climate catastrophe.

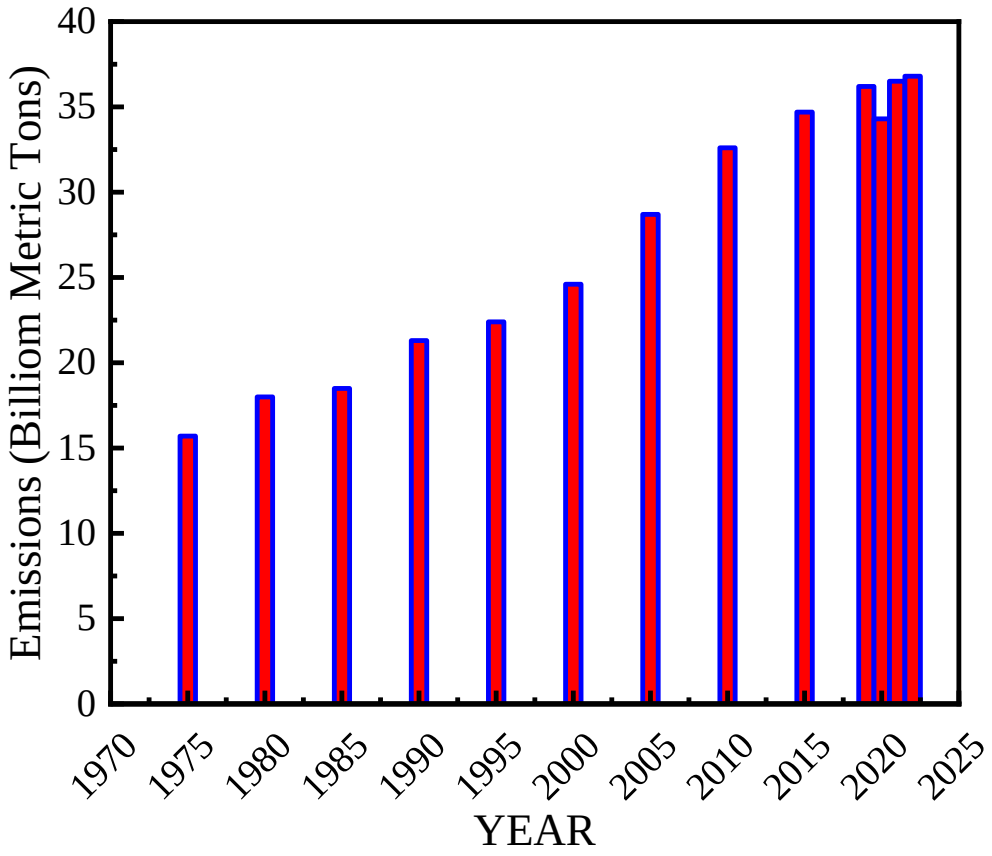

Figure 1.1: Worldwide carbon dioxide emission from 1975 to 2022

Keeping these in mind, it's the need of the hour to develop alternative energy sources that should be renewable and pollution-free compared to traditional fossil fuel-based sources. Switching to renewable energy sources will be expected to generate energy with less of an environmental impact than fossil fuels.[9] Different countries have started research on developing much-needed renewable energy alternatives to replace traditional ones.[10] Renewable energy sources can be utilized to generate energy repeatedly, such as solar energy, wind energy, geothermal energy, etc.[11] These sources are believed to meet the growing energy needs with zero or negligible carbon dioxide emission.[12] One of the key advantages of these energy sources is their installation in developed and remote areas such as deserts. The decentralized harvesting of renewable energy sources is one of the options for meeting energy needs in a reliable, sustainable,

and affordable manner. Till now, solar energy, being cost-effective and efficient, is leading among all renewable energy sources competitors.[13] It is the energy generated from the sunlight, and the device used for this purpose is referred to as a solar or photovoltaic (PV) cell.[14] The possibility of obtaining more than 2.5 petawatts (PW) from the Sun over a large area of the earth makes this source attractive. Solar energy is leading the race from other renewable energy sources by a magnitude of several orders. According to an estimate, the energy that can be extracted from the recoverable oil resources is around 1.7×10^{22} joules (J), which the Sun delivers in only 1.5 days.[15] The energy supplied by the Sun in just an hour is enough to meet the overall energy needs of humanity, which are around 4.6×10^{20} J.[16,17] Solar energy offers numerous advantages, including near-zero greenhouse gas emissions, the stabilization of degraded land, increased energy independence, job creation, enhanced rural electrification, and improved standards of living in developing countries. These benefits make it an appealing option across various regions globally.

1.2. Solar Cells

A solar cell operates on the principle of the 'Becquerel effect,' named after the French physicist Edmond Becquerel, who discovered the PV effect in 1839.[18] The energy conversion process in solar cells entails two primary steps: 1) light absorption, leading to the creation of an electron-hole pair, and 2) the subsequent separation and movement of the electron and hole to the respective terminals, thereby generating electrical power.[19] As solar cell technology has evolved, it has progressed through several generations, each marked by advancements in materials, cost-effectiveness, and efficiency. Figure 1.2 illustrates the different generations of solar cells.

The first generation of solar cells predominantly utilizes silicon-based PV devices. Among these, crystalline silicon-based solar cells, whether monocrystalline or polycrystalline, remain the earliest and most widely employed.[20] Monocrystalline silicon cells are fabricated from a single crystal, whereas polycrystalline cells are composed of multiple crystals. These cells exhibit moderate efficiency levels and have firmly established themselves in the market.[21] In contrast, the

second generation of solar cells is characterized by thin-film technology. Thin-film solar cells employ a diverse range of materials, including amorphous silicon (a-Si), cadmium telluride (CdTe), and copper indium gallium selenide (CIGS). They earn the moniker "thin-film" due to their significantly thinner active material layers than crystalline silicon cells. This feature endows thin-film cells with greater flexibility and reduced weight, expanding their potential applications across various sectors.[22,23]

The third generation of solar cells, often denoted as Advanced Thin-Film and Emerging Technologies, represents a diverse array of innovations aimed at surmounting the limitations of previous generations. This category encompasses advanced thin-film technologies, dye-sensitized solar cells (DSSC), organic PV (OPV), perovskite solar cells (PSCs), and more. Among these, PSCs stand out for their significant potential in enhancing efficiency and reducing production costs, marking a promising advancement in solar technology.[24] Furthermore, the term "Fourth Generation" has been used in speculative contexts to denote concepts and innovations still in their nascent stages of research and development.

Depending on the era and the scope for improvement, PSCs have sparked considerable debate within the PV community. Remarkably, within just a decade, PSCs have achieved a photon-to-electrical energy conversion efficiency comparable to traditional silicon solar cells, reaching up to 26.1%.[25] This class of solar cells boasts advantages such as tunable band gaps and the feasibility of solution processing, making them amenable to fabrication under ambient conditions.

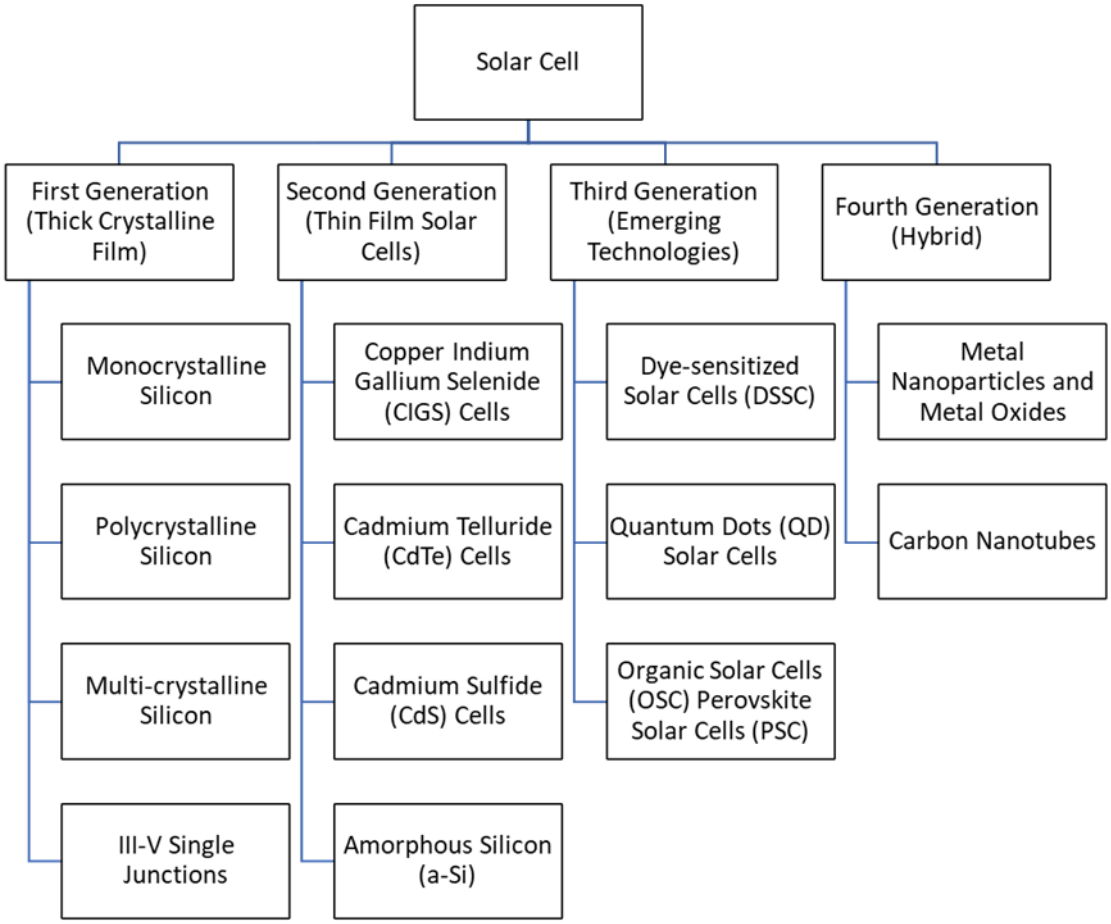

Figure 1.2: Classification of solar cells according to different generations

1.3. Perovskite Solar Cells

Perovskite materials have emerged as promising candidates for light absorption in solar energy conversion. Initially, oxide-based perovskites like $SrTiO_3$ garnered considerable attention for their potential as photocatalysts in water splitting.[26,27] Subsequently, halide-based perovskites, particularly those incorporating iodide, bromide, and chloride, emerged as focal points in research due to their exceptional optoelectronic properties. These perovskites have captivated the research community's interest in solar cell technology owing to their remarkable optoelectronic characteristics, including:

- **Efficiency:**

The PSCs have shown outstanding power conversion efficiencies (PCEs) comparable to traditional silicon-based solar cells.[28]

- **Tunability:**

By varying the composition of the composite materials, the band gap and properties such as processing temperature, stability, and hydrophobicity can be varied.[29]

- **Cost of Fabrication:**

The solution processibility of PSCs made them depositable at low temperatures and in a vacuum-free environment, resulting in a lesser fabrication cost than traditional silicon-based solar cells.[30]

- **Flexibility:**

Due to their solution processibility, PSCs can easily be deposited on flexible plastic substrates compared to rigid glass substrates, making them light-weight and portable.[31,32]

- **Printable:**

Due to solution processibility and low processing temperature, PSCs are printable. In addition to the perovskite material, PSC printing necessitates careful selection of constituent layers, such as the electron transport layer (ETL) and hole transport layer (HTL).[30]

PSC's functional layers are discussed in detail in Chapter 2.

1.4. Problem Statement

Compared to other advanced solar cells, PSCs can achieve high efficiency at a relatively moderate cost. Their ability to respond to a wide range of light wavelengths and convert a significant portion of incident radiation into electricity makes PSCs particularly advantageous over

traditional photovoltaic technologies.[33] It may be applied in various ways since it can be deposited over a flexible substrate. In the realm of PV, silicon solar cells continue to be dominating. There are opportunities for developing solar cells that have the potential for either a considerable reduction in fabrication costs or a dramatic increase in PCE. PSCs show promising results on both fronts. PSCs are the first solar cells in history to attain a remarkable 26.1% PCE in a short period.[34] A considerable improvement in surpassing the traditional solar cells in efficiency made PSCs a potential replacement for traditional Silicon solar cells. PSCs are highly efficient in terms of cost of production, with limitations such as stability, portability, and health hazards.

For scalable and portable PSCs fabricated on cheap plastic substrates, device layers should be processed below 150 ^{o}C. This is due to the thermal instability of commonly used plastic substrates for fabricating scalable and portable PSCs. Among all its functional layers, ETL, usually, has the highest processing temperature. Thus, achieving stable and portable PSCs using scalable fabrication techniques requires solution and low-temperature processible ETLs, ideally < 150 ^{o}C.[35,36] The most commonly reported ETLs for PSCs are zinc oxide (ZnO), titanium oxide (TiO_2), and tin oxide (SnO_2) based ETLs. Among these, mesoporous-TiO_2 has historically been the favored ETL material. However, it is associated with drawbacks such as requiring higher annealing temperatures, exhibiting low electron mobility, and being susceptible to negative photocatalytic processes under UV light.[37] ZnO, on the other hand, earned the attention of the researchers due to its lower temperature processibility. However, poor thermal stability of ZnO results in fast degradation of the perovskite layer, which limits its applications.[38] SnO_2, due to its excellent charge extraction, better band alignment with perovskites, desired charge carrier concentration, and better light transmission, has been preferred ETL in the recent past.[39] In the context of flexible optoelectronic devices, such as flexible solar cells, a key challenge with using SnO_2-based ETLs is their need for higher annealing temperatures during fabrication. Annealing is a heat treatment process used to enhance the properties of materials, like improving the crystallinity and conductivity of SnO_2. However, flexible substrates, typically made from plastic or other polymers,

cannot withstand high temperatures without deforming or degrading. Consequently, the high annealing temperature required for SnO_2-based ETLs limits their integration into flexible devices, which necessitates developing low-temperature processing methods or alternative materials that can achieve similar performance without compromising the flexibility and integrity of the substrate. Till now, different SnO_2 nanoparticle (NP)-based aqueous commercial solutions are employed as ETL ink in the fabrication of glass-based PSCs but are not found to be productive for the application in flexible optoelectronic device fabrication.[40] Exploring alternatives, such as switching from SnO_2 NPs to SnO_2 quantum dots (QDs)-based ETLs, may prove effective in overcoming these challenges and enhancing the applicability of PSCs in flexible optoelectronic device fabrication. Further research and optimization in this direction are warranted to realize the full potential of PSCs in the renewable energy landscape.

1.5. Research Objective

The widespread adoption of PSCs hinges on their commercial viability, which relies heavily on scalable manufacturing processes. This scalability enables mass production at reduced unit costs, thereby enhancing the competitiveness of solar energy within the renewable energy landscape. PSCs are a pivotal solution to future energy demands, contingent upon their large-scale and cost-effective production. As the demand for renewable energy sources continues to rise, the need for scalable solutions becomes increasingly critical. However, a significant challenge lies in the applicability of metal oxide ETLs for fabricating scalable and flexible optoelectronic devices. This challenge stems from the inherent trade-off between device PCE and processing temperature. ETLs that can be deposited at lower temperatures via scalable techniques typically offer lower PCE, while those requiring higher temperatures exhibit enhanced efficiency.

Given these challenges, our research aims to address this issue by proposing an alternative ETL composed primarily of SnO_2 QDs instead of conventional SnO_2 NPs. We present a detailed procedure for synthesizing SnO_2 QDs and explore their utilization as an ETL in fabricating slot-

die-coated (SDC) PSCs. We aim to develop low-temperature solution-processed SnO_2 QDs that exhibit performance comparable to their counterparts while remaining compatible with scalable synthesis methods. Through this approach, we seek to advance the commercial feasibility of PSCs and pave the way for their widespread adoption in the renewable energy sector. To accomplish this goal, the synthesis and use of SnO_2 QDs might be approached in numerous ways:

- Synthesis of SnO_2 QDs:

Use of solution-based synthesis methods to obtain SnO_2 QDs. Solution-based synthesis methods may involve sol-gel processes, chemical precipitation, or hydrothermal/solvothermal synthesis tailored to yield colloidal NPs of the desired size and properties.

- Solution Processing of SnO_2 QDs as an ETL:

Development of a solution processing method for depositing prepared SnO_2 QDs inks onto flexible substrates.

- Optimization of Processing Parameters:

Exploring various processing parameters such as solution concentration, deposition temperature, and processing conditions to optimize the morphology and performance of the SnO_2 QD layers as ETLs.

- Characterization and Performance Evaluation:

A comprehensive characterization study will analyze the structural, optical, and electronic properties of SnO_2 QD ETLs. Evaluate the performance of SDC PSCs incorporating SnO_2 QD ETLs through PV measurements, efficiency calculations, and bending tests.

By adopting a solution-processible approach and optimizing the performance of SnO_2 QD ETLs at lower processing temperatures, this proposed method offers a feasible and effective solution for fabricating efficient and flexible PSCs (FPSCs).

1.6. Thesis Organization

The outlines of this thesis are as follows.

Chapter 2 presents a thorough literature review, discussing the fundamental aspects of PSCs. It particularly emphasized the discussion of the advancements and obstacles to development in PSCs.

Chapter 3 contains the material and device characterization technique for analyzing SnO_2 QDs and the fabricated device.

Chapter 4 explains the synthesis of SnO_2 QDs, the development of SnO_2 QDs-based ink and its optimizations. Optimization is done by fabricating corresponding slot-die-coated flexible PSCs with varying concentrations of SnO_2 QDs in ETL ink.

Chapter 5 compares the performance of synthesized SnO_2 QDs-based ink with the commercially available SnO_2 NPs-based dispersion solution. The chapter discusses the advantages of switching from SnO_2 NP-based ink to SnO_2 QDs-based ink.

An overview of its original contributions and important conclusions is provided in Chapter 6. It also provides a view of prospective future studies in the field.

Figure 1.3 presents the schematic distribution of the chapters presented in this thesis.

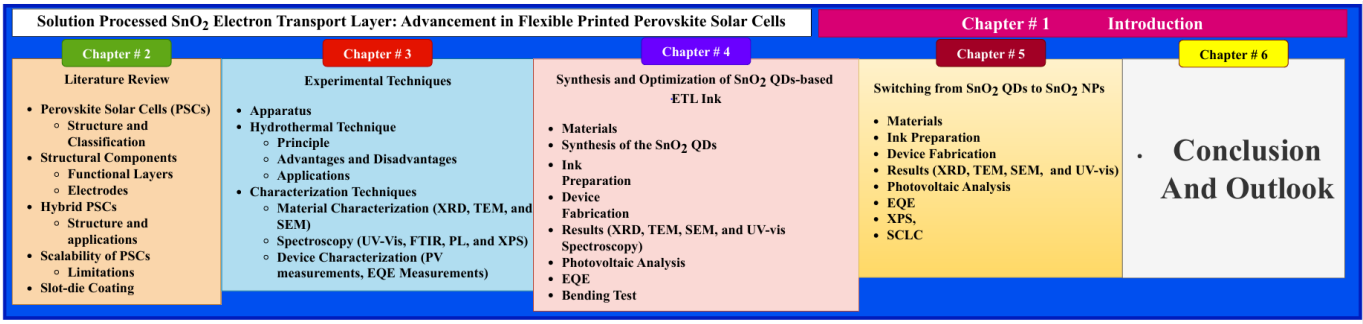

Figure 1.3: Diagram showing the organization of thesis

Chapter#2

Literature Review

2. Perovskite Solar Cells

2.1. Perovskite Materials

Perovskites constitute one of the most intriguing classes of materials, with characteristics that extend from ferroelectricity to superconductivity.[41] It refers to the crystal structure of calcium titanate ($CaTiO_3$), first coined by German mineralogist Gustav Rose (1839) and named after Russian mineralogist Lev Perovski.[42,43] Lately, in 1926, it was used by Victor Goldschmidt as a general term for the crystal structure group ABX_3.[44]

2.1.1. Structure and Classification of Perovskite Materials

A general perovskite has an ABX_3 structure. In this structure, the smaller B cation of the perovskite is octahedrally coordinated by X anion, sharing the corner of the 3D lattice. "A" cation fills vacancies between the octahedra.[45] Figure 2.1 (a) shows the general structure of perovskite. The possibility and stability of a perovskite structure can be found by finding its Goldschmidt tolerance factor (t) and Jahn-Teller distortion (μ):[46,47]

$$t = \frac{r_A + r_X}{\sqrt{2(r_B + r_X)}} \qquad (2.1)$$

$$\mu = \frac{r_B}{r_x} \qquad (2.2)$$

Where r_A, r_B, and r_X represent the atomic radii of A, B, and X, respectively. [46] Generally, materials with t between 0.9 and 1.0, and $\mu > 0.442$ possess stable cubic perovskite structures, whereas materials in which t < 0.9 or $t > 1.0$ possess distorted or non-perovskite structures.[47] Depending upon the A, B cations, and X anion, the perovskites can be classified into inorganic oxide, halide, hybrid, and hydroxide perovskites and further as shown in Figure 2.1b.[48]

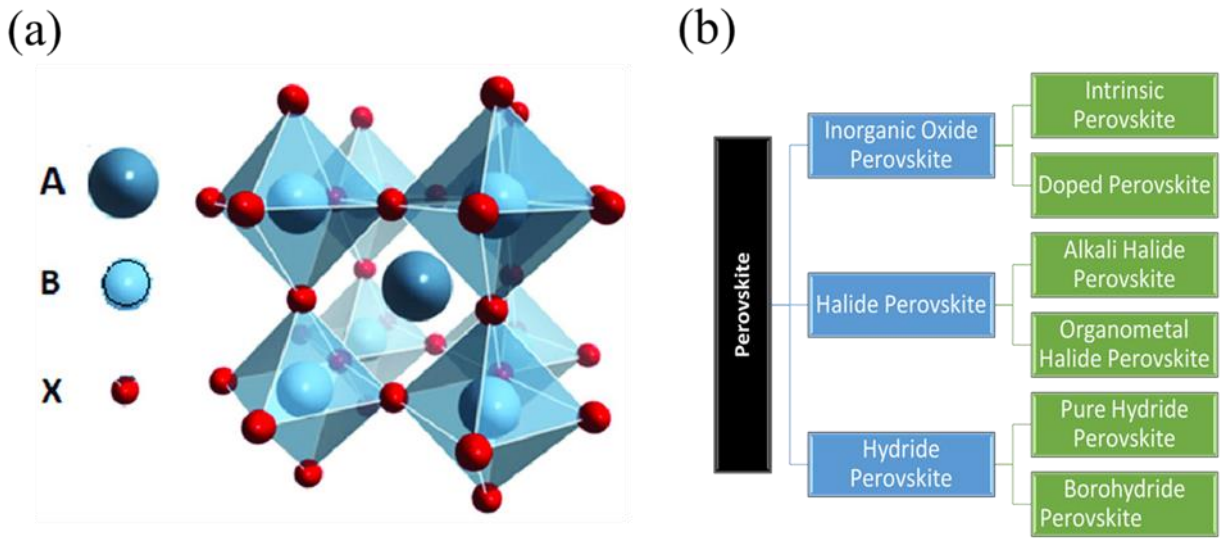

Figure 2.1: (a) Crystal structure and (b) classification of perovskite materials [49]

An inorganic-oxide perovskite consists of all inorganic materials with X-site occupied by oxygen (O). Electronic conductivity, mobility of oxide ions through the crystal lattice, electrically active structure, chemical and thermal stability, variations in oxygen content, and super-magnetic, thermoelectric, photocatalytic, and dielectric properties were among the attractive physical and chemical properties displayed by inorganic perovskite-type oxides. These are intriguing materials with various applications in electrochemical sensing, fuel cells, and catalysis. These oxides possess greater catalytic activity than many compounds, including transition metals and even certain oxides of precious metals.[50]

Another exciting class of perovskite materials is “halide perovskite,” which consists of perovskites, in which the A-site is occupied by either or both metals, a transition metal occupies the B-site, and the X-site is occupied by a halogen. The most common X-site halogens are iodide or bromide. Depending upon the constituent materials, halide perovskites are either organic-inorganic hybrid (or organometal halide) perovskites or alkali halide perovskites. Due to their exceptional photophysical qualities and ease of solution processing, metal-halide perovskites are widely employed in solar cells, photodetectors, light-emitting diodes (LEDs), and lasers.[51,52]

Halide perovskites exhibit various crystal structures, encompassing cubic, orthorhombic, trigonal, hexagonal, monoclinic, and tetragonal forms. The specific structure of a perovskite is determined by the constituent atoms occupying the A, B, and X sites and the processing conditions during formation. Typically, at elevated temperatures, the cubic phase prevails due to a reduced degree of rotation of the A-site cations. As the temperature decreases, the phase transitions sequentially to tetragonal and then orthorhombic configurations.[53]

Similarly, the bandgap of a perovskite is highly contingent upon its constituent atoms. Generally, halide-based hybrid perovskites, such as $MAPbX_3$ and $FAPbX_3$, exhibit direct bandgaps and superior semiconducting performance. These materials offer a range of bandgaps from 1.45 eV to 3.0 eV, which can be tuned by altering either the A-site organic cation or the X-site halogen anion. While the A cation primarily compensates for charges within the lattice and does not significantly influence the band structure, changes in its size can deform the BX_6 octahedron network, leading to variations in optical characteristics. The overall lattice dimensions can vary due to the presence of a smaller or larger A cation, influencing the B-X bond length, which is critical in defining the bandgap. Notably, the bandgap of a perovskite material decreases with the increase in (a) the BX_6 network dimensionality, (b) the angle of the B-X-B bonds, and with the decrease in the (c) electronegativity of anions, and (d) effective electronegativity difference between the metal cation and the anion. While the nature of the elemental atoms (molecules) directly influences the final two characteristics, external factors such as temperature

and pressure also impact the first two.[54] Table 2.1 illustrates the variations in bandgap associated with changes in the constituent atoms.[55,56]

Table 2.1: Perovskite materials and their bandgaps

Perovskite	Bandgap (eV)
$MAPbI_3$	1.55
$FAPbI_3$	1.48
$MAPbBr_3$	2.35
$FAPbBr_3$	2.23
$MAPbCl_3$	2.90
$MASnI_3$	1.30

For application in single-junction PV devices, iodide-based hybrid perovskites are preferred due to the bandgap's optimal values, i.e., 1.1 to 1.60 eV.[54] The halide *p*-orbitals strongly contribute to the optical transition; the inorganic framework primarily determines the bandgaps of the hybrid halide perovskites. On the other hand, the 1*s* orbitals of hydrogen and the 2*p* orbitals of carbon and nitrogen do not contribute much to the density of states close to the Fermi level when considering the influence of the A-site cations. However, the band gap may be indirectly varied by lattice expansion brought on by the steric impact of the A-site cations, which results in varied B-X bond lengths and bond angles.[57]

Perovskites can be inorganic or hybrid depending on the A-site. In this case, if the A-site cation is inorganic, e.g. cesium (Cs), the B-site is lead (Pb) or tin (Sn), and the X-site is iodide (I), then it will result in an inorganic perovskite ($CsPbI_3$ or $CsSnI_3$). Contrarily, if the A-site is occupied by an organic material such as methylammonium (MA) or formamidinium (FA) and the B-site is occupied by inorganic material, then it will result in hybrid perovskite material like $MAPbI_3$ or $FAPbI_3$. Hybrid perovskite materials can have multiple organic A-site cations, as in the case of $MA_{0.95}FA_{0.05}PbI_3$. A similar effect can be possible for an X-site halide or a mixed halide. They possess properties like direct band gap (higher absorbance than Si, GaAs), $p \rightarrow p$ transition, tunability of bandgap from 1.3 eV to 2.5 eV, low exciton binding energy, large absorption

coefficient, long diffusion length, high charge carrier lifetime, low-temperature solution processibility, and higher defect tolerance.[30] The most commonly reported perovskite for PSCs is $MAPbI_3$ due to its suitable bandgap, lower crystallization temperature, and compatibility with scalable techniques such as slot-die coating and blade coating.[58]

2.2. Structural Components of Perovskite Solar Cells

A typical structure of a PSC is depicted in Figure 2.2, showcasing three functional layers sandwiched between the top and bottom electrodes. However, it's worth noting that PSCs can vary in their structures depending on the specific design and materials used. For instance, some PSC configurations may include additional layers or interfaces to enhance performance or stability. Common variations include mesoporous structures, where a mesoporous layer is incorporated between the perovskite absorber and planar the charge transport layers. This can afford improved charge transport and minimized recombination losses. Additionally, inverted PSC structures, where the ETL is positioned above the perovskite layer, are gaining attention for their potential to enhance device stability. Each structure offers unique advantages and challenges, and researchers continue to explore novel designs to optimize PSC performance for various applications.[30]

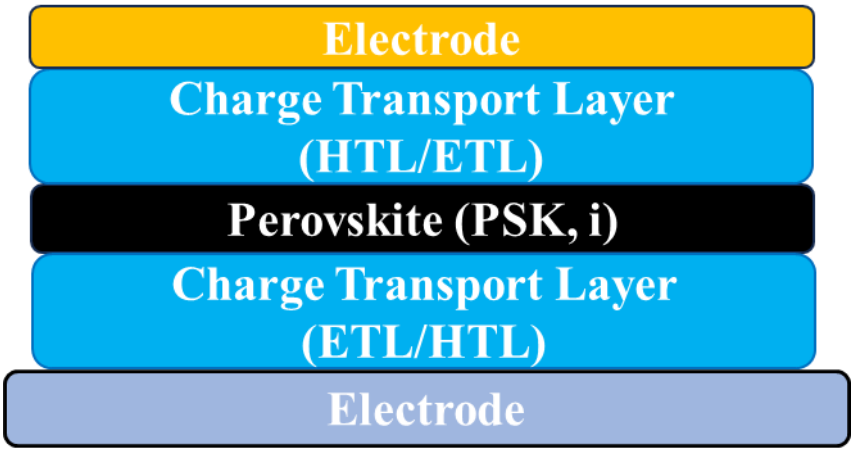

Figure 2.2: General device architecture for PSC

2.2.1. Functional Layers

Usually, a PSC consists of the following three functional layers:

- Electron Transport Layer

An ETL is an essential component in PSCs, facilitating efficient electron extraction and transportation from the photoactive perovskite layer to the corresponding electrode while blocking holes to enhance device performance. An ideal ETL should exhibit high transparency, high electron mobility and conductivity, good stability and compatibility with the perovskite layer, and proper band alignment with it. Commonly employed ETL materials include TiO_2, SnO_2, and ZnO.[59–62] This research highlights the ongoing efforts to optimize ETL design and fabrication processes to enhance the performance and stability of PSCs for practical applications.[63,64]

- Perovskite layer

A perovskite layer, sandwiched between the other functional layers, is the heart of the device and is responsible for the absorption of the incident light and the generation of charge carriers. An ideal perovskite should be stable and possess high optical absorption, weak exciton binding energy, high carrier mobility, longer charge carrier diffusion length, low defect density, and ease of processing.[65,66]

- Hole Transport Layer

The third functional layer in a PSC is the p-type HTL, which plays a crucial role in extracting and transporting holes generated within the device. An effective HTL should exhibit high charge carrier mobility and conductivity, as well as optimal Highest Occupied Molecular Orbital (HOMO) and quasi-Fermi levels, to facilitate efficient hole transfer from the perovskite layer to the HTL. Additionally, it should possess a higher Lowest Unoccupied Molecular Orbital (LUMO) to effectively block electrons, along with robust stability against moisture, thermal, UV, and chemical degradation. Morphologically, the HTL should be pinhole-free and seamlessly connected

with the perovskite layer for optimal performance.[67] Commonly utilized HTL materials include 2,2',7,7'-Tetrakis[N,N-di(4-methoxyphenyl)amino]-9,9'-spirobifluorene (Spiro-MeOTAD), Poly[bis(4-phenyl)(2,4,6-trimethylphenyl)amine] (PTAA), Poly(3-hexylthiophene) (P3HT), and Poly(3,4-ethylenedioxythiophene) polystyrene sulfonate (PEEDOT:PSS) among others. These materials are chosen for their compatibility with perovskite layers and their ability to promote efficient charge transport and extraction, contributing to PSCs' overall performance and stability.[30,68]

2.2.2. Electrodes

PSCs have bottom and top electrodes for extracting and transporting charge carriers from the functional layers to the external circuits. The widely used bottom electrodes are indium tin oxide (ITO) or fluorine-doped tin oxide (FTO); the top electrodes are silver (Ag), gold (Au), or aluminum (Al).[69] The selection of electrodes depends upon the used ETL and HTL materials. The electrode/ETL and HTL/electrode interface play an integral role in the overall device performance, governing the charge extraction and transport mechanism between the corresponding layers and the electrode.[70]

2.3. Hybrid Perovskite Solar Cells

The device design is one of the important considerations when evaluating the overall performance of PSCs. The architecture of hybrid PSCs (HPSCs) is classified as conventional or inverted according to which charge (hole/electron) transporting material is external to the cell or initially encounters the incident light. The term "conventional/regular" usually refers to the nip configuration, where the ETL is at the bottom, followed by the perovskite layer, and the HTL on top. Conversely, "inverted" generally refers to the pin configuration, where the HTL is at the bottom, followed by the perovskite layer, and the ETL on top.

These two structures may be further divided into planar and mesoscopic structures. "Planar" refers to a compact layered architecture without significant porosity, while "mesoporous" indicates a structure that includes a porous scaffold, enhancing the surface area and potentially improving efficiency. Figure 2.3 shows a schematic representation of all these structures.[71]

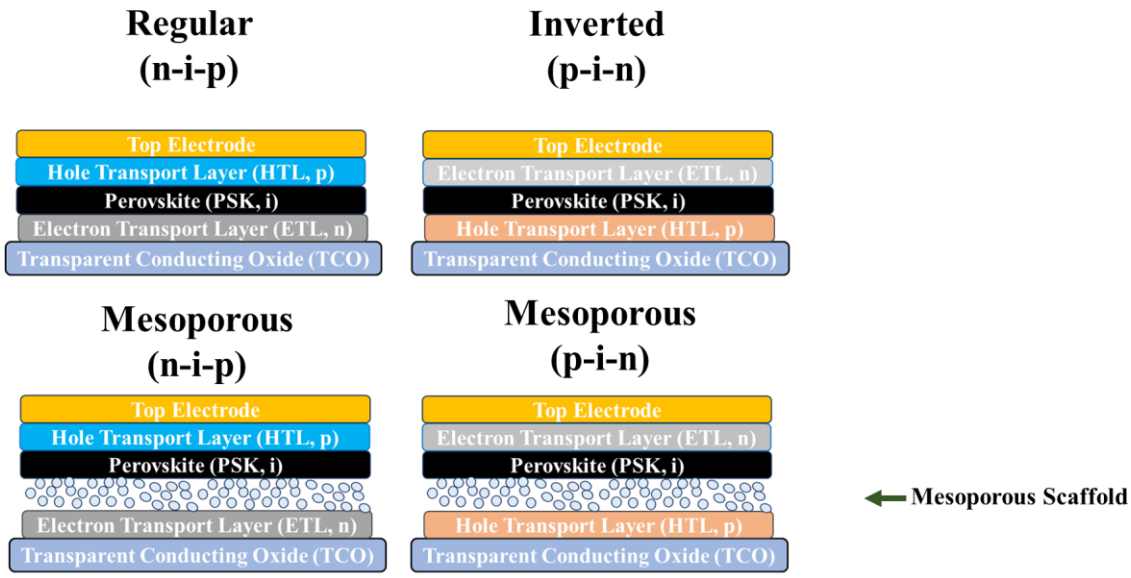

Figure 2.3: Different device architectures for PSCs

2.3.1.1. Regular Planar Structure

A typical regular planar PSC comprises multiple layers designed to convert sunlight into electricity. The structure begins with a substrate, commonly glass or polyethylene terephthalate (PET), which provides structural support while permitting light transmission. Above the substrate, there is a layer of transparent conducting oxide (TCO), which serves as the front electrode of devices. Above this layer lies the n-type layer, known as the ETL, which can be composed of materials such as TiO_2, SnO_2, or ZnO. This layer facilitates electron transfer to the electrode while preventing hole movement. The central layer is the perovskite absorber layer, also known as the intrinsic (i-type) layer. This layer is often made of compounds like $MAPbI_3$, which absorbs sunlight and generates electron-hole pairs. Above the perovskite layer is the p-type layer, referred to as the HTL. This layer consists of materials such as Spiro-MeOTAD, PTAA, and NiO_x, which

selectively transfer holes to the back electrode while blocking electrons. The final layer is the back electrode, which is typically made of Au, Ag, or other suitable metallic materials depending on HTL.[72]

In a regular planar PSC, illuminations occur from the glass and ETL side, which is why it is termed a 'n-i-p' structure. When sunlight enters the cell, the perovskite layer absorbs photons, generating electrons in the conduction and holes in the valence bands. These charge carriers are guided to the ETL and HTL, respectively, and collected at the electrodes, resulting in an electric current that may be utilized to generate electricity. This planar structure enables effective light absorption and charge transfer, contributing to PSCs' high efficiency.

2.3.1.2. Regular Inverted Structure

Inverted PSCs exhibit a structural configuration that contrasts with the conventional planar form by reversing the sequence of the electron and hole transport layers. These cells typically commence with a substrate that is coated with a TCO. Directly deposited on the TCO is the HTL, with common materials for this layer including PEDOT:PSS and nickel oxide (NiO_x). Subsequently, the perovskite absorber layer is deposited. Following this, the ETL is applied, which frequently consists of materials such as phenyl-C61-butyric acid methyl ester (PCBM) or ZnO. The structure is finalized with a metal electrode, typically composed of Al or Ag, which collects electrons. This inverted architecture can enhance the stability of PSCs, potentially offering advantages over the conventional planar design.[73,74]

2.3.1.3. Planar Mesoporous Structure

Planar mesoporous PSCs integrate both planar and mesoporous architectures to enhance light absorption and charge separation efficiencies. The fabrication of these cells begins with a substrate, typically glass coated with a TCO, which provides both structural support and optical transparency. A compact ETL, commonly TiO_2, is then deposited onto the substrate. This layer

facilitates electron mobility while serving as a barrier to hole transport. Following this, a mesoporous layer, also usually composed of TiO_2, is deposited to form a scaffold with a substantial surface area. The mesoporous scaffold is then infiltrated with the perovskite material, filling the pores and forming a continuous film over the scaffold. This design ensures intimate contact between the perovskite layer and the mesoporous structure, which significantly enhances the interface for charge transfer. Above the perovskite layer, an HTL is deposited. This layer, composed of materials like Spiro-OMeTAD or PTAA, selectively facilitates hole transport to the electrode while inhibiting electron transfer. The mesoporous architecture increases the surface area available for perovskite deposition, thereby improving the interface between the charge transport layer and the perovskite material. This configuration reduces recombination losses and enhances charge extraction, leading to improved PV performance.[75,76]

2.3.1.4. Inverted Mesoporous Structure

Inverted mesoporous PSCs integrate both planar and mesoporous structures to optimize light absorption and charge separation. The fabrication process begins with a substrate, usually glass coated with a TCO, which provides essential structural support and optical transparency. The next step involves depositing a compact HTL, typically composed of NiO_x, directly onto the TCO. This layer facilitates efficient hole mobility. Subsequently, a mesoporous NiO_x layer is deposited to form a scaffold with a high surface area. This mesoporous NiO_x scaffold is then infiltrated with the perovskite material, ensuring that the pores are filled and a continuous film is formed over the scaffold. This step is crucial for establishing intimate contact between the perovskite layer and the mesoporous structure, thereby optimizing the interface for charge transfer. Above the perovskite layer, an ETL is deposited. Materials commonly used for this layer include PCBM or ZnO. The ETL selectively facilitates the transport of electrons to the electrode while inhibiting the transfer of holes.[77]

The inverted mesoporous architecture increases the surface area available for perovskite deposition, enhancing the interface between the charge transport layers and the perovskite material. This configuration effectively reduces recombination losses and enhances charge extraction, resulting in improved overall PV performance.

2.4. Operational Principle

The conversion of sunlight into electricity by PSCs is governed by a sequence of four fundamental processes: 1) light absorption, 2) charge carrier generation, 3) charge separation, and 4) charge collection. These stages collectively define the operational mechanism of PSCs.

- Light Absorption: The process begins with the perovskite layer absorbing incident sunlight. The perovskite material's broad absorption spectrum allows it to effectively capture photons across a wide range of wavelengths, facilitating a high degree of photonic energy conversion.
- Charge Carrier Generation: Upon absorbing light, the perovskite material generates charge carriers, specifically electrons and holes. This occurs as photons excite electrons from the valence band to the conduction band, creating electron-hole pairs within the perovskite structure.
- Charge Separation: The generated charge carriers must then be effectively separated to prevent recombination. This separation is achieved through the interfaces between the perovskite layer and the adjacent charge transport layers, ETL and HTL. The intrinsic electric field at these interfaces aids in directing the electrons toward the ETL and the holes toward the HTL.
- Charge Collection: The final stage involves the collection of the separated charge carriers. Electrons are transported through the ETL to the cathode, while holes move through the HTL to the anode. This directed movement of charge carriers results in the generation of an electric current, which can then be extracted and utilized for external applications.

Figure 2.4 provides a detailed depiction of these processes, illustrating the comprehensive operational mechanism of PSCs and highlighting the critical stages involved in the efficient

conversion of solar energy into electrical power. For optimal performance, a PSC necessitates precise alignment of the energy levels among its constituent layers. This alignment is crucial to ensure efficient charge transfer and to minimize energy losses. Specifically, at the interface between the ETL and the perovskite layer, it is imperative to minimize the conduction band offset while maximizing the valence band offset. Such an alignment promotes efficient electron transfer from the perovskite to the ETL while effectively inhibiting the movement of holes, thus reducing recombination losses. Similarly, at the interface between the perovskite layer and the HTL, it is essential to minimize the valence band offset and maximize the conduction band offset. This configuration facilitates smooth hole transfer from the perovskite to the HTL and prevents undesired electron backflow, thereby enhancing the separation and collection of charge carriers.

Achieving these precise energy level alignments is critical for optimizing the internal electric fields and charge dynamics within PSCs. Proper alignment enhances charge transport and extraction, thereby improving the overall efficiency and operational stability of the device. The careful tuning of energy levels between the ETL, perovskite layer, and HTL thus represents a fundamental strategy in the design and development of high-performance PSCs.[78]

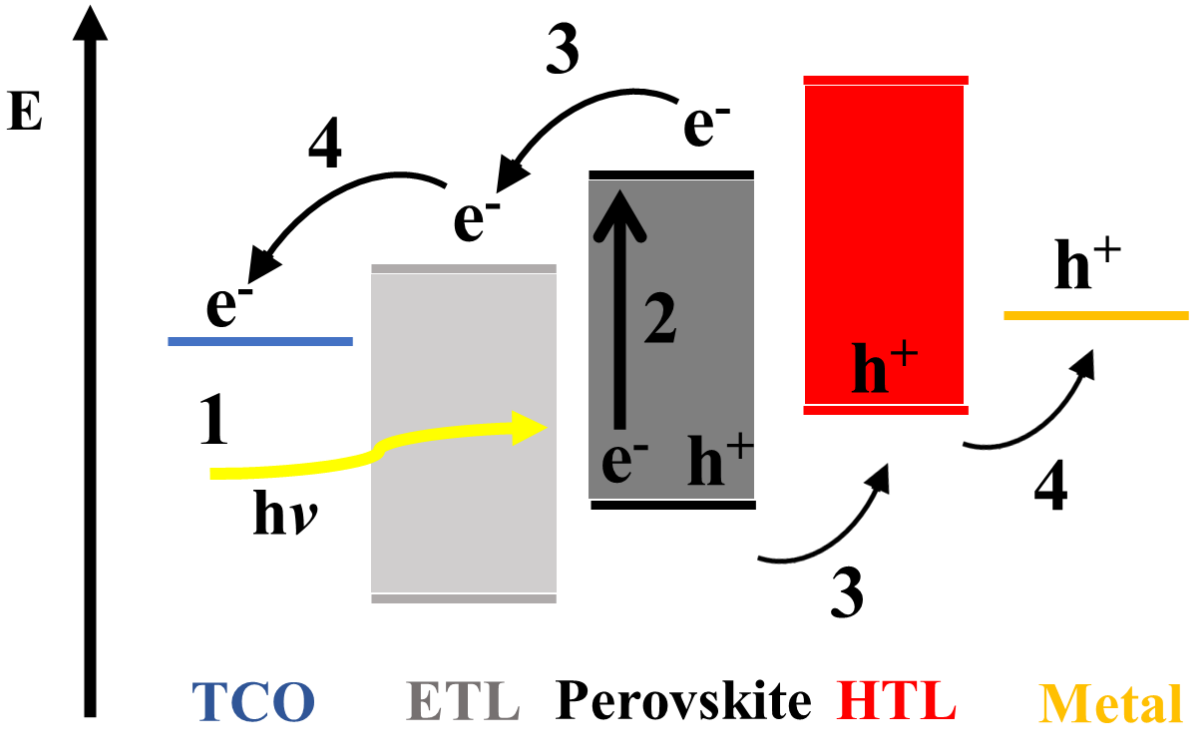

Figure 2.4: Band diagram demonstrating the fundamental concepts behind the operation of PSCs

2.5. Scalability of Perovskite Solar Cells

Despite being low-cost, having facile fabrication processes, and the potential to achieve high efficiency, the scalability of HPSCs remains a key challenge worldwide.[79,80] The following are the key scalability considerations for HPSCs:

2.5.1. Materials Stability

Given the sensitivity of the functional layers in HPSCs to moisture and air, developing a stable and sustainable functional layer is imperative.[81,82] Research is actively underway to address this challenge, with various groups working on developing stable materials, each with advantages and disadvantages. One widely adopted approach involves encapsulating the PSC cells, although this method remains costly and impractical for industrial-scale applications.[83–85]

2.5.2. Environmental Impact

Highly efficient PSCs include toxic elements, such as lead (Pb). Developing PSCs with less toxic lead-free perovskite materials is essential.[86,87] Green solvents also need to be explored to make the production environment friendly and scalable at an industrial scale.

2.5.3. Mechanical Robustness

Manufacturing FPSC involves several obstacles, notably in the ETL and active layer. Mechanical strength is one of the most important considerations. FPSCs must withstand repetitive bending, stretching, and other mechanical stresses while maintaining efficiency and performance. This necessitates materials and layers that are not only effective but also durable.

2.5.4. Substrate compatibility

Another crucial consideration for FPSCs is the flexible substrates, which are often comprised of plastics or polymers, must be compatible with the numerous layers placed on them. This compatibility encompasses temperature qualities, chemical interactions, and physical adhesion.

2.5.5. Coating homogeneity

Coating homogeneity across wide regions is a prerequisite for FPSCs. Depositing a homogeneous layer of ETL and active material promotes constant performance across the cell. However, maintaining this consistency on flexible, possibly uneven surfaces can be difficult.

2.5.6. Fabrication Techniques

Until now, state-of-the-art HPSCs have primarily been fabricated using the traditional spin-coating technique within an inert nitrogen environment, often employing a glovebox for handling.[63,88] Various fabrication methods, including spin-coating, ink-jet printing, blade coating,

and slot-die coating, are currently under development to address these challenges.[32,89–91] Table 2.2 consists of the list of widely used techniques for fabricating HPSCs.[92,93]

Table 2.2: Scalable techniques with their Pros and Cons

Technique	Cost-effectiveness	Advantages	Disadvantages
Spin coating	Serious ink wastage	Rapid drying with excellent film formation	Non-commercial due to non-scalability
Slot-die coating	Precise and economical ink usage	Precise and effective control over the film formation, high throughput, compatible with roll-to-roll (R2R) fabrication and commercial applications	Sensitive and complex process parameters
Blade coating	High ink wastage	The process is simple and compatible with other scalable processes	Not feasible with patterning and sensitive parameters like temperature
Spray coating	Fast production with high material usage	Suitability for a range of substrates and a continuous process with a high coating rate	It is challenging to deposit homogeneous films since the process is intricate and sensitive to the viscosity and surface tension of the solution
Gravure printing	Effective and productive	Rapid printing speed and high throughput	It is not good for the fabrication of uniform perovskite file

Screen printing	Low consumption	Widely used for HTL, ETL and contact layer deposition	Poor repeatability and reproducibility
Inkjet printing	Low consumption	Facile and time-saving	Lack of control over the crystallinity and depends on more controlling parameters such as voltage

Among all these widely employed scalable techniques, the slot-die coating technique provides the benefit of high throughput and precise control over the film deposition, thickness, and crystallinity. In recent times, it has also been regarded as the most promising R2R-compatible method for producing thin-film PVs on an industrial scale.[94] Hwang et al. provided the first attempt at fabricating HPSCs employing slot-die coating. In this case, the perovskite film was deposited sequentially to form a pinhole-free lead iodide (PbI_2) film with gas-quenching administered slot-die coating, which was then followed by a slot-die coating of MAI to stimulate the PbI_2 to perovskite conversion reaction.[95] It is also possible to print ETL and HTL using slot-die coating; a champion PCE of about 12% was attained on a fully printed device. Eventually, with a PCE of more than 10%, the aperture area of slot-die-coated minimodules may be up-scaled to 168.75 cm^2.[96] The champion PCE of PSCs manufactured using slot-die coating may easily approach 22% by managing the nucleation and crystallization for perovskite films.[97]

Chapter # 3

Experimental Techniques

The third chapter of the thesis is based on a brief explanation of the experimental technique and apparatus used. To make the study easy and interesting, this chapter is further divided into the following sections:

- ❖ Hydrothermal Route
- ❖ Fabrication of SDC HPSCs
- ❖ Characterization techniques

All these steps made possible our attempt to keenly investigate the properties of the material (SnO_2) and SDC FPSCs under observation.

Let’s discuss all these steps one by one.

3.1. Hydrothermal Route

A hydrothermal reaction is a chemical reaction that occurs in an aqueous environment at elevated temperature and pressure. The term "hydrothermal" combines "hydro" (water) and "thermal" (heat), reflecting the conditions under which these reactions take place.

Hydrothermal reactions are of interest in various fields, including chemistry, geology, materials science, and environmental science. They are significant in the formation of minerals, the synthesis of novel materials, the study of organic reactions, and even in the origins of life.

Some key characteristics of hydrothermal reactions include:

- ➢ Temperature and Pressure

Hydrothermal reactions typically occur at temperatures above the boiling point of water (100 °C at standard pressure) and at pressures higher than atmospheric pressure. These conditions vary widely depending on the specific reaction and its intended outcome.

- Solvent Properties of Water

Water is a versatile solvent in hydrothermal reactions, facilitating the dissolution of reactants and intermediates. The unique solvent properties of water under high temperature and pressure conditions can influence reaction pathways and product formation.

- Enhanced Reactivity

Hydrothermal systems' elevated temperature and pressure conditions can enhance the reactivity of substances, leading to accelerated reaction rates and the formation of products that may not be accessible under ambient conditions.

- Mineral Formation

Hydrothermal reactions play a crucial role in forming many minerals found in nature. For example, hydrothermal vents on the ocean floor are sites where mineral-rich fluids rise from beneath the Earth's crust, precipitating various minerals as they interact with seawater.

- Synthesis of Nanomaterials

Hydrothermal methods are widely used to synthesis nanomaterials due to their ability to control particle size, morphology, and composition. By adjusting reaction parameters such as temperature, pressure, and reactant concentrations, it is possible to tailor the properties of the resulting nanomaterials for specific applications.

Overall, hydrothermal reactions represent a fascinating area of research with applications ranging from fundamental studies of chemical reactivity to synthesizing advanced materials with unique properties. A solvothermal technique is similar to hydrothermal with an organic solvent like ethanol used instead of water. The synthesis of the utilized SnO_2 QDs is done via a

solvothermal route with ethanol as a solvent (Chapter 4). The hydrothermal reactor and Teflon liner are purchased from Toption (China).

3.2. Fabrication of Slot-Die Coated Hybrid Perovskite Solar Cells

3.2.1. Slot-Die Coating

For high-throughput fabrication, slot-die coating is a compatible method that enables the deposition of thin, uniform coatings over large areas. Depending upon the substrate and the deposition area, it allows deposition via R2R or sheet-to-sheet (S2S) fabrication of SDC PSCs. [32,98] Figure 3.1 shows the photographic images of the slot-die coaters in the Advanced Optoelectronics Laboratory at Nazarbayev University, Kazakhstan.

Figure 3.1: Photographic images of slot-die coaters for (a) flexible (NanoRoll, FOM Technologies) and (b) flexible/rigid (Vector, FOM Technologies) substrates

3.2.2. Working Principle

A slot-die coater works on a principle that involves using a specialized nozzle (slot-die) to supply and spread ink onto a substrate placed on a moving roll or chuck. The key to enhanced performance is selecting and synthesizing suitable ink and optimizing ink supply and distribution parameters. Different components of slot-die coater control the supply and distribution parameters. The SDC of PSCs involves the following steps:

- Substrate Mounting:

A vacuum chuck holds a substrate, which can be glass or PET, with a patterned TCO layer. The vacuum chuck holds the substrate securely and sets up a uniform surface for subsequent layer deposition.

- Assembling of the Slot-die Head:

Assembling a slot-die head involves using the meniscus guide and shim. These components play a crucial role in controlling the thickness and uniformity of the film. Firstly, they are inserted into the slot-die head with the help of the alignment pin. Then, the slot-die head is closed and secured with the help of specialized bolts.

- Ink Supply:

Once the slot-die head is ready, it's time to arrange a controlled supply of ink. The supply of the relevant functional layer ink is carried out with a pump. The pump is connected to the slot-die using tubing and connectors.

- Coating Parameters Selection:

1) Pump Rate:

   Controls the ink flow rate from the syringe pump to the slot-die head.

2) Coating Window:

The gap between the substrate and the slot-die head is called the coating window. The coating window affects the thickness and uniformity of the deposited layer.

- Execution of the Coating Process:

Once all the components are properly set up, slot-die coating is initiated. The ink is dispensed onto the moving substrate, forming a thin, uniform film of the functional layer required for PSCs.

Selection and precise control of the pump rate, coating speed, and coating window are crucial to achieve uniform film. Meanwhile, proper handling and alignment of the substrate on the vacuum chuck ensure consistent surface coating of the functional layers. Regular calibration of the slot-die coating system is essential to maintain the accuracy and repeatability of the coating process. Overall thin film thickness and quality depends upon the following factors:

- Distance between chuck and the slot-die head (Height)
- Chuck speed
- Ink flow rate
- Wet film thickness

The thickness of the wet film can be estimated using the thickness equation:[99]

$$d = \frac{fc}{Swp} \tag{2.5}$$

where d is the thickness, f is the flow rate, S is the chuck speed, w is the coating window, and c is the solid content in the solution. Figure 3.2 depicts the schematic diagram of the coating and relevant coating parameters.

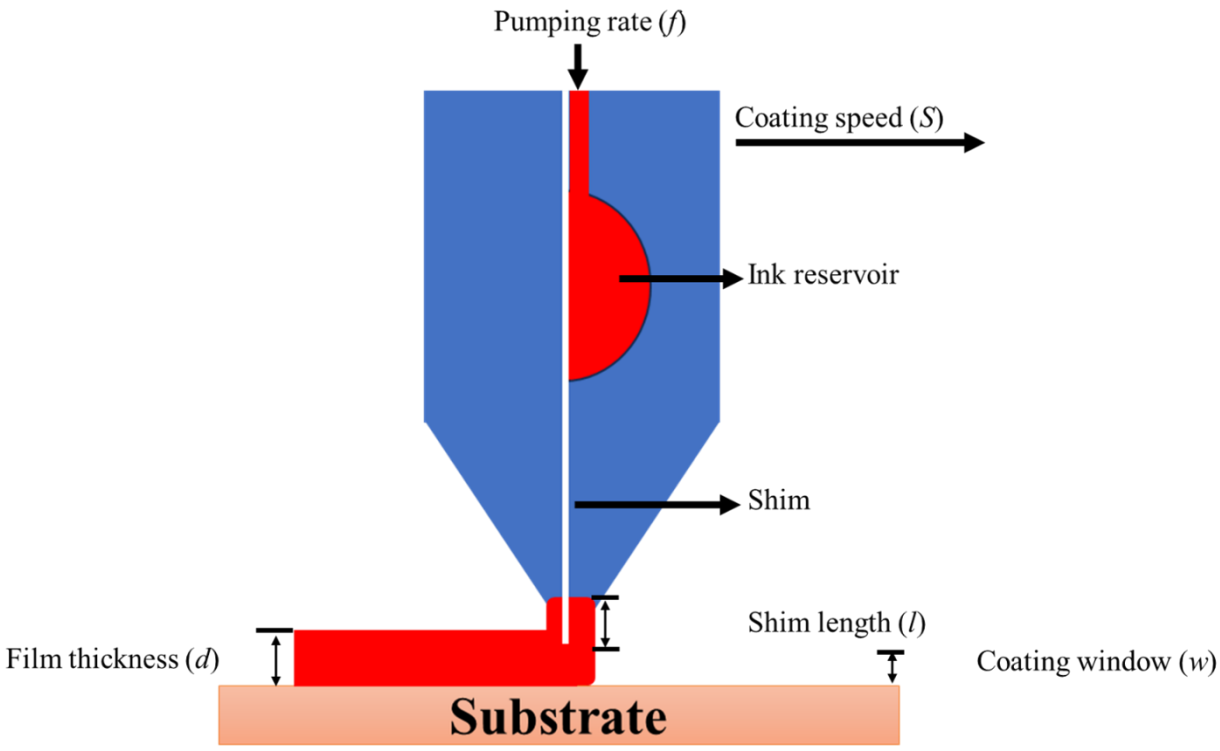

Figure 3.2: Schematic diagram illustrating slot-die coating process and an indication of main features and parameters

3.3. Characterization Techniques

Different characterization techniques were used to investigate the properties of SnO_2 QDs and SDC-FPSCs keenly. These techniques ensure the nature and performance of these materials. We utilize the following techniques.

3.3.1. X-Ray Diffraction Technique

X-ray diffraction (XRD) is a widely used analytical technique for analyzing the structural properties of both inorganic and organic materials, such as powders, films, and solids. The fundamental principle behind XRD measurements involves detecting elastically scattered X-rays, which occur when incoming X-ray radiation interacts with the ordered atomic arrays in the crystal lattice of a material (Figure 3.3).

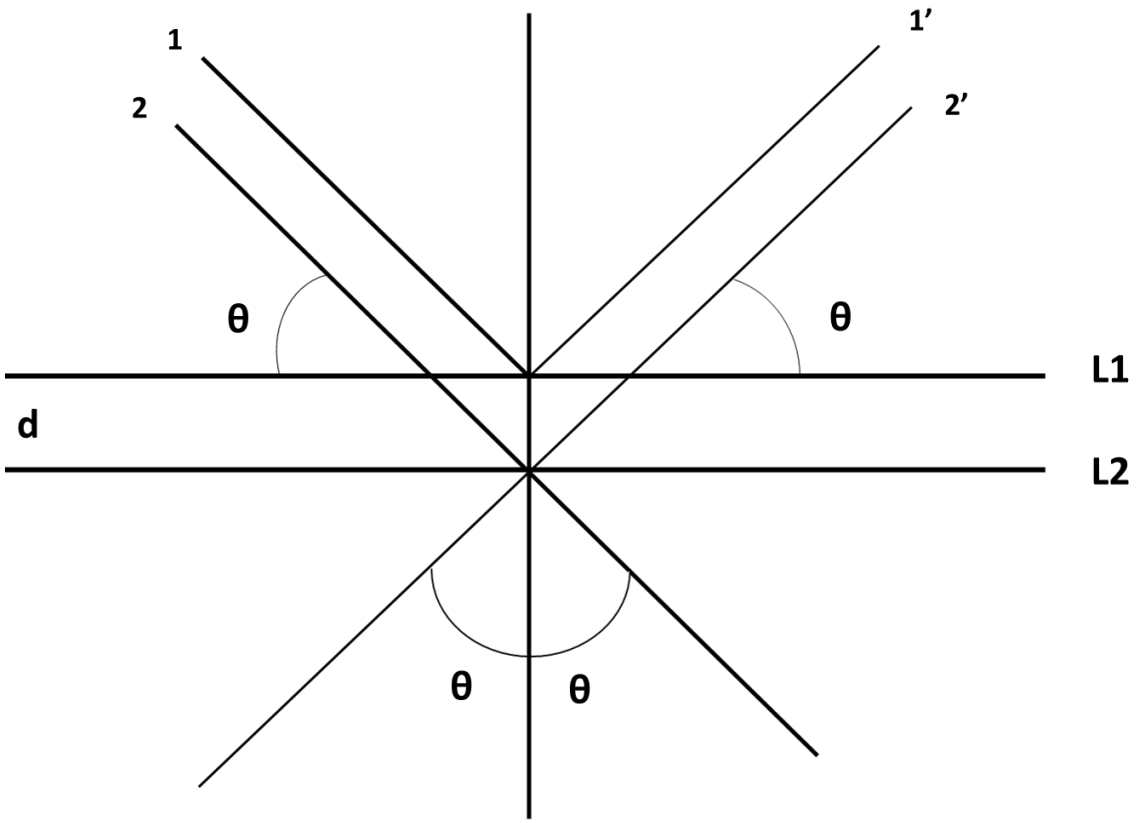

Figure 3.3: Schematic illustration depicting scattering of incident X-ray beam from different crystal planes of material

When an X-ray beam interacts with the atomic planes in a crystalline material, it is scattered by the electrons, producing a distinct diffraction pattern. This occurs because the wavelength of the X-ray radiation, typically Cu-K_α radiation with a wavelength of about 0.15 nm, is on the same scale as the interatomic spacings within the crystal lattice. The diffraction pattern is generated by plotting the intensity of the scattered X-rays against the scattering angle. Peaks in the diffraction spectrum correspond to the constructive interference of the scattered radiation. Bragg's law describes the relationship between the angle of constructive interference and the dimensions of the lattice planes:[100]

$$2d \sin\theta = n\lambda \qquad (3.1)$$

So, the possible 2θ values which can give reflections are different angles for different cell dimensions. The distribution of electrons in crystals determines the intensities of these beams. An XRD data can be utilized to estimate the crystallite size (*d*) from the peaks using the Scherrer equation:[101]

$$d = \frac{n\lambda}{\beta cos\theta}, \qquad (3.2)$$

where *n* is the Scherrer's constant (mostly its value is 0.9), λ is the wavelength of the incident beam (in the present case, its value is 1.54 Å), and β is the full width at half maximum (FWHM).

XRD has many applications in material science and characterization, mineralogy and geology, pharmaceuticals, catalysis and chemistry, thin films and coatings, archaeology and cultural heritage, polymorphism and phase analysis, and protein crystallography. These applications demonstrate the versatility and importance of XRD across various scientific disciplines and industries.

3.3.2. Electron Microscopy

Electron microscopy is a highly effective characterization technique that employs high-energy electrons to illuminate a specimen, providing structural, compositional, and morphological details. By accelerating electrons at high voltages, electron microscopy utilizes electrons with wavelengths significantly shorter than visible light, allowing for resolutions far surpassing the limits of optical microscopes around 200 to 300 nm. The de Broglie equation describes the wavelength of accelerated electrons (λ), with the applied voltage (*V*), which accounts for the difference between the rest (m_0) and the relativistic mass (*m*) of the electrons.[102]

(3.3)

$$\lambda = \frac{h}{\sqrt{2m_o eV(1 + \frac{eV}{2m_o c^2})}}$$

where *e*, *c*, and *h* are the charge of an electron, velocity of light, and Planck's constant, respectively.

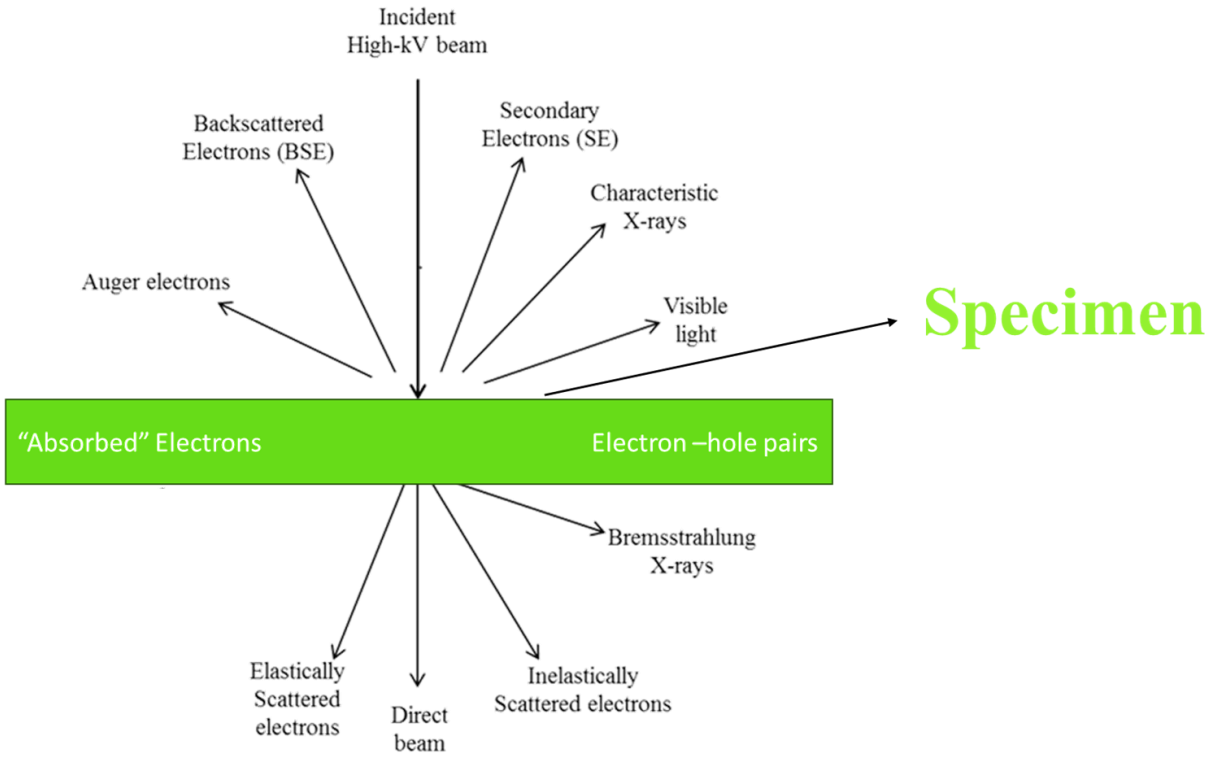

Figure 3.4: Schematic illustration showing a primary electron beam hitting a sample and the resulting secondary signals in electron microscopy

Figure 3.4 shows the schematic view of the incident electron beam on the specimen and possible generated signals. Utilization of these signals using scanning electron microscopy (SEM) and transmission electron microscopy (TEM) provides the required information.

- Transmission Electron Microscopy

In TEM investigations, high-energy electrons are used to penetrate thin samples, typically less than 100 nm thick, generating secondary signals that can be detected beneath the sample (see

Figure 3.4). TEM operates with electron acceleration voltages ranging from 80 to 400 kV, producing electrons with very short wavelengths. For example, at 100 kV, the electron wavelength is approximately 4 pm, significantly smaller than interatomic spacings, which can be up to 0.1 nm. This allows for the imaging of lattice planes within the crystal structure.

There are two primary methods for generating the electron beam in a TEM. The first method involves heating a LaB_6 crystal or tungsten filament to induce thermionic emission of electrons. The second method, known as the "cold" approach, involves extracting electrons from tungsten tips using a strong electric field. The resultant beam of intense electrons is focussed using an electromagnetic condenser lens system that can be precisely adjusted by varying the current. When the focused beam encounters the specimen, electrons passing through it are first focussed by the objective lens, resulting in a primary magnified picture of the specimen. The image is then enlarged by intermediate and projection lenses. Finally, the image is shown on a fluorescent screen or recorded with a charge-coupled device (CCD) camera (see Figure 3.5).

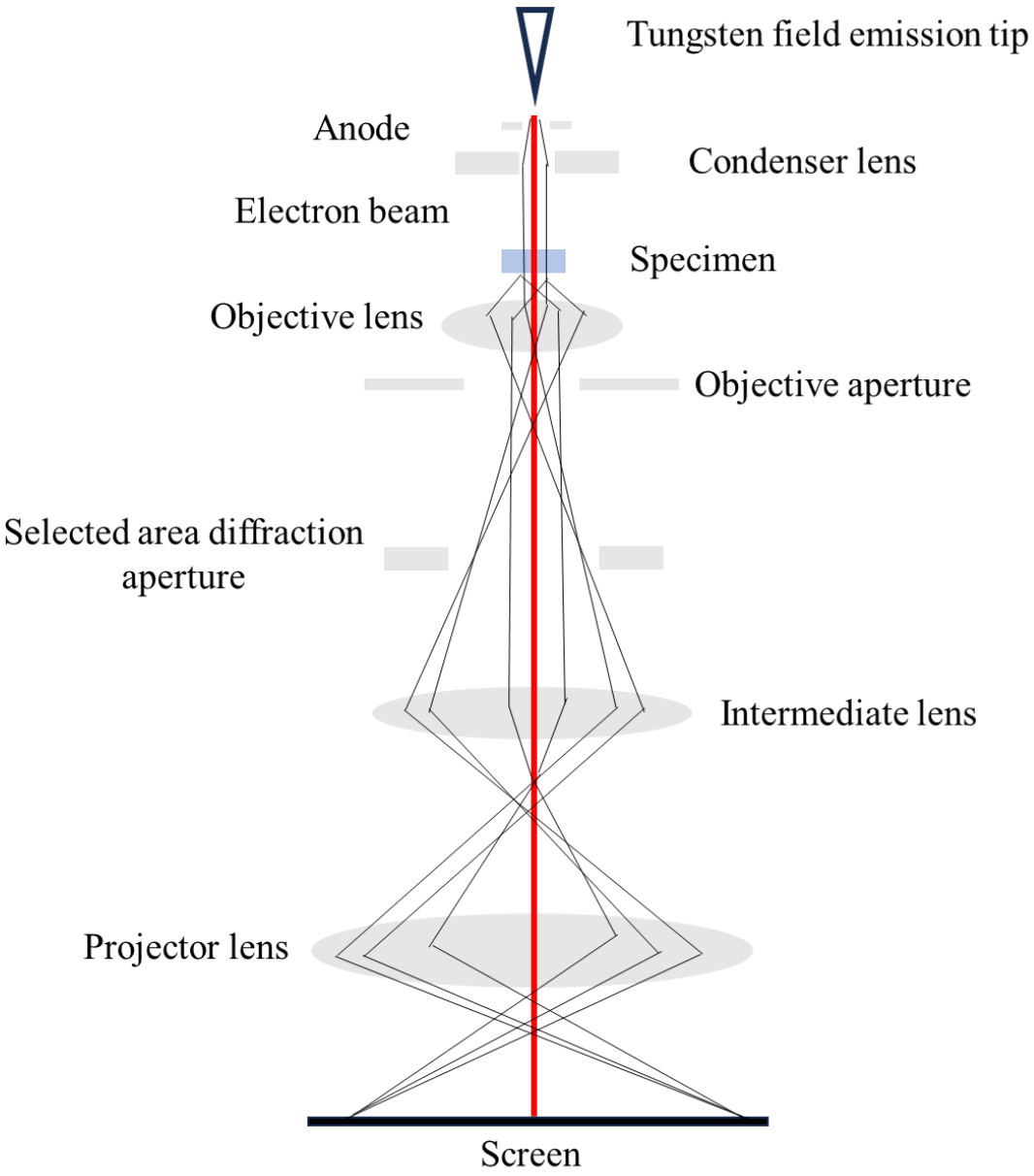

Figure 3.5: Optical path in TEM a schematic representation

TEM offers various operational modes to analyze specimens. One common mode is bright-field (BF) imaging, which is achieved by selectively blocking scattered electrons with the objective aperture, allowing directly transmitted electrons to form the image. Conversely, dark-field (DF) imaging is obtained by blocking the directly transmitted electrons and using scattered electrons to create the image. Scanning Transmission Electron Microscopy (STEM) is another essential mode in which an electron beam is focussed onto a small region on the specimen at a greater convergence angle and rastered across it. To obtain a high-resolution STEM image, the transmitted electrons

are gathered based on the precise position of the beam. Furthermore, electron diffraction patterns may be generated by focusing the imaging system on the objective's rear focal plane.

This provides detailed structural information about the specimen. For compositional analysis, techniques such as Electron Energy Loss Spectroscopy (EELS) are employed. EELS analyzes inelastically scattered electrons to provide insights into the elemental composition and electronic structure of the specimen.[102]

- Scanning Electron Microscopy – Instrumentation

In SEM measurements, energetic electrons are used for imaging motives. Unlike TEM, SEM illuminates the object with an electron beam of relatively low energy, ranging from 10^{-1} to 30 kV. This lower-intensity beam predominantly generates secondary signals from the sample's surface, which are subsequently analyzed and imaged, as shown in Figure 3.4.

During SEM measurements, the intense electron beam, also known as the probe beam, is precisely focused on the specimen and swept across its surface in a television raster pattern. When the electron beam interacts with the specimen, the electrons scatter inelastically, resulting in a variety of secondary signals. These include secondary electrons (SE), backscattered electrons (BSE), Auger electrons, distinctive X-rays, and cathodoluminescence. The signals generated are detected, amplified, and then used to image and characterize the sample, as shown in Figure 3.6. Since the signals are taken from the specimen's surface, the sample thickness is not restricted much. However, it is important to consider the effective secondary signal collection depth, which

is approximately 2 µm. This factor must be taken into account during specimen preparation to ensure accurate and effective imaging and hence analysis.

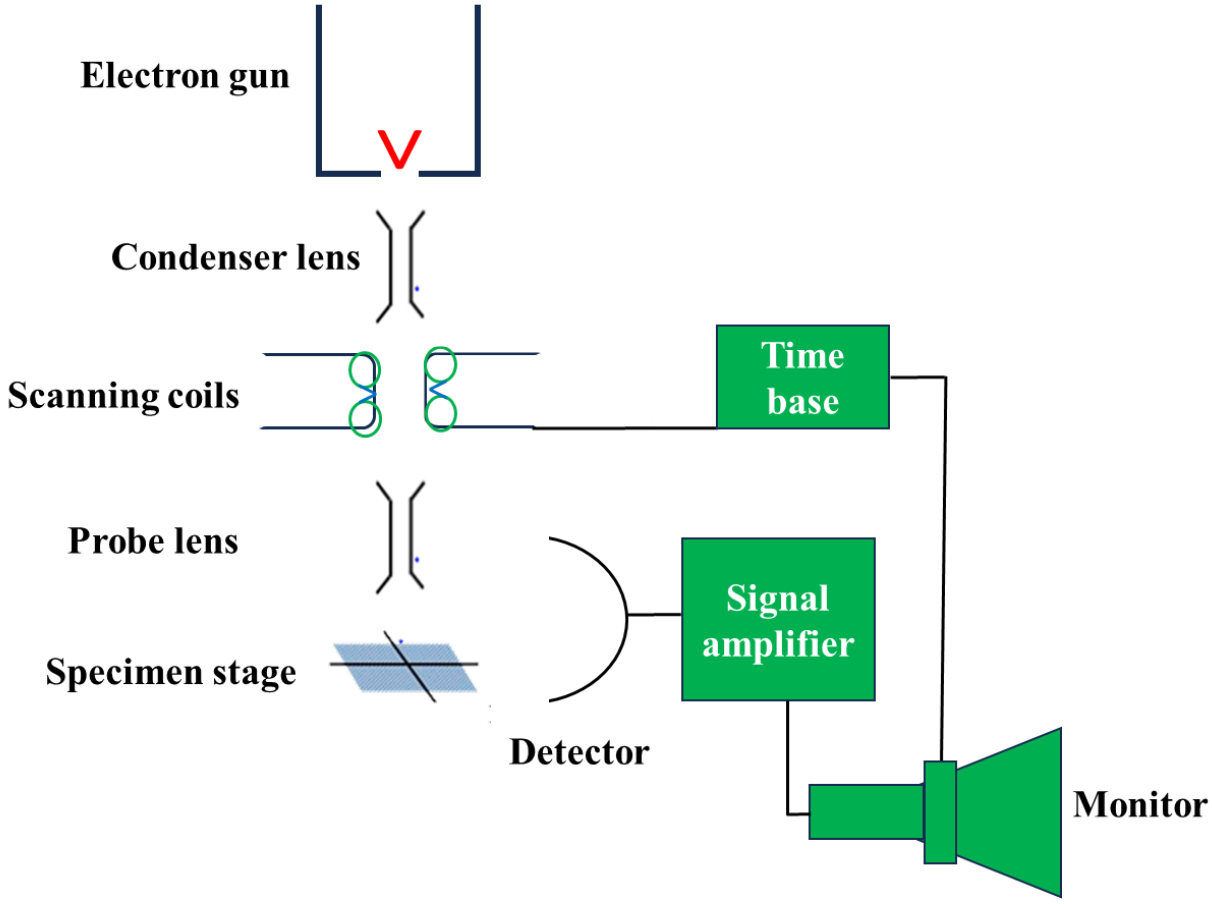

Figure 3.6: Schematic representation of a SEM

The BSE secondary signal is sensitive to the average atomic number (Z) of the specimen, allowing for images that reveal information about different phases within the sample, such as in composite or alloy materials. In contrast, the SE signal is sensitive to surface topography, providing detailed images of the sample's surface features. Characteristic X-rays emitted from the specimen can be detected and analyzed using an energy-dispersive X-ray spectrometer (EDX). This allows for the characterization of the chemical composition at specific points on the specimen. Furthermore, by recording X-rays as a function of the incident electron beam's coordinates during a raster scan, a chemical concentration map of the sample can be generated. This map provides a detailed spatial distribution of the chemical elements within the selected area of the specimen.[102]

3.3.3. Ultraviolet-Visible Spectroscopy

Ultraviolet-Visible (UV-Vis) spectroscopy is an efficient analytical method for examining how materials absorb UV and visible light. This spectroscopic technique is helpful in various disciplines, including chemistry, biology, materials science, and environmental research, as it offers important insights into molecules' electronic structure and chemical environment.

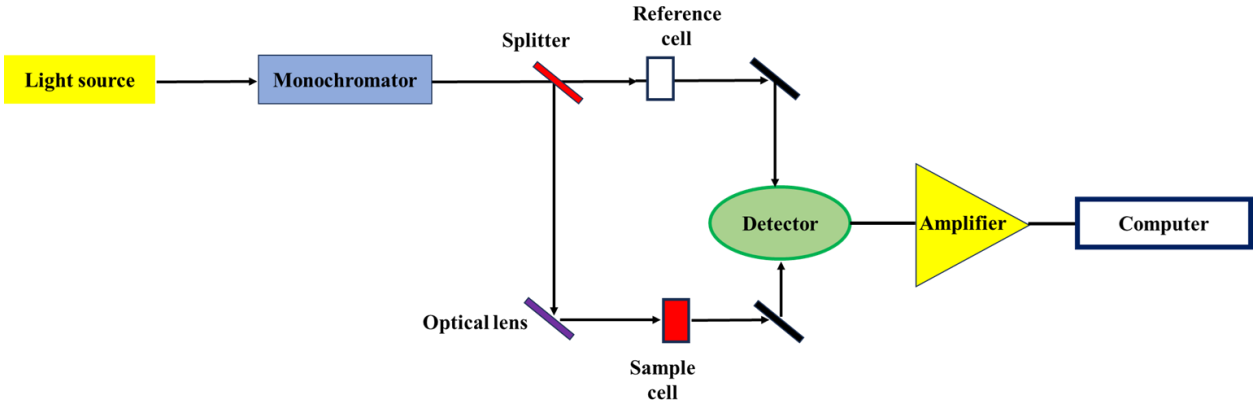

Figure 3.7: Schematic representation of a UV-Vis spectroscopy setup

A typical UV-Vis spectrophotometer used for analyzing thin films consists of several key components: a light source, a monochromator, a sample compartment, a detector, and a data acquisition system. The light source emits a broad spectrum of light, including both visible and UV wavelengths, with tungsten-halogen lamps commonly used for visible light and deuterium lamps for UV light. The monochromator selects a specific wavelength from this spectrum, utilizing a slit to allow only the desired wavelength through and a prism or diffraction grating to split the light into its constituent wavelengths. The sample compartment is designed to hold the thin film sample, which is typically mounted on a transparent substrate. The detector, often a photodiode or photomultiplier tube, measures the intensity of light that either passes through or reflects off the thin film as a function of wavelength. The data acquisition system collects this information,

generating a spectrum by measuring the intensity of transmitted or reflected light at various wavelengths.

To perform a UV-Vis spectroscopy experiment on a thin film, the sample is placed in the sample compartment. The spectrophotometer is calibrated using a reference measurement, often a blank substrate without the thin film. The instrument then scans the visible and UV regions of the spectrum, measuring the amount of light that transmits through or reflects off the thin film at each wavelength. The resulting spectrum displays the absorption (*A*) or reflectance (*R*) of light by the thin film as a function of wavelength, calculated using the Beer-Lambert Law: [103]

$$A = \log\left(\frac{I_0}{I}\right) = \epsilon c l \qquad (3.4)$$

Where I_0 and I represent the intensities of the incident and transmitted light, respectively, ϵ denotes the molar absorptivity, c is the concentration of the absorbing species, and l is the path length of the light through the sample in centimeters. This absorption or reflectance spectrum provides valuable information about the optical properties and thickness of the thin film, as well as its electronic and structural characteristics.

While UV-Vis spectroscopy is a versatile technique, it has a few limitations. Its sensitivity is limited, making it less suitable for trace analysis compared to other spectroscopic methods like mass spectrometry or fluorescence spectroscopy. Additionally, it has limited chemical selectivity; it can provide information about the general electronic structure but cannot distinguish between chemical species that absorb light at the same wavelength.

3.3.5. Photoluminescence Spectroscopy

Photoluminescence (PL) spectroscopy is a powerful analytical technique widely employed in the study and optimization of PSCs. This method involves the excitation of a material using a light source, typically a laser, which promotes electrons from the valence to the conduction band.

Photons are emitted by these electrons once they relax and return back to the valance band. A handful of insights regarding electronic and structural properties can be collected by analysis of this emitted light. PL spectroscopy is particularly useful for investigating charge carrier dynamics in PSCs. By analyzing the intensity and decay of the emitted light, it is possible to infer the recombination processes occurring within the perovskite material, including both radiative recombination, where emitted photons are observed, and non-radiative recombination, which affects the PL intensity and efficiency. The technique is instrumental in identifying and characterizing defects and trap states within the perovskite layer. Defects can act as non-radiative recombination centers, quenching the PL signal. By studying the PL spectrum and lifetime, one can gauge the density and impact of these defects, aiding in the development of defect passivation strategies to enhance solar cell performance. Additionally, the quality of the perovskite layer can be assessed through PL measurements. High-quality perovskite films exhibit strong PL emission with minimal non-radiative recombination. The FWHM of the PL peak can indicate crystal quality and uniformity, with narrower peaks generally signifying higher crystallinity and fewer defects.

PL spectroscopy also provides a direct measure of the optical band gap of the perovskite material. The peak position of the PL emission corresponds to the band gap energy, which is crucial for determining the suitability of the material for solar cell applications. Moreover, by introducing various quenching agents or by varying the environmental conditions (e.g., temperature, atmosphere), the quenching mechanisms in perovskites can be studied. This helps in understanding how different factors influence the photophysical properties and stability of PSCs. In multi-layered PSC structures, PL spectroscopy can be used to probe specific layers. By adjusting the excitation wavelength and depth, it allows to focus on the perovskite layer or interfaces, providing insights into the interaction between different layers and the overall device architecture.

To perform PL spectroscopy on PSCs, the sample is typically illuminated with a laser beam, and the emitted light is collected and analyzed using a spectrometer. Key parameters measured include the PL intensity, peak wavelength, and decay time. Time-resolved PL (TRPL)

can also be employed to study the dynamics of carrier recombination over time. A schematic representation of the experimental setup of PL spectroscopy is presented in Figure 3.8.

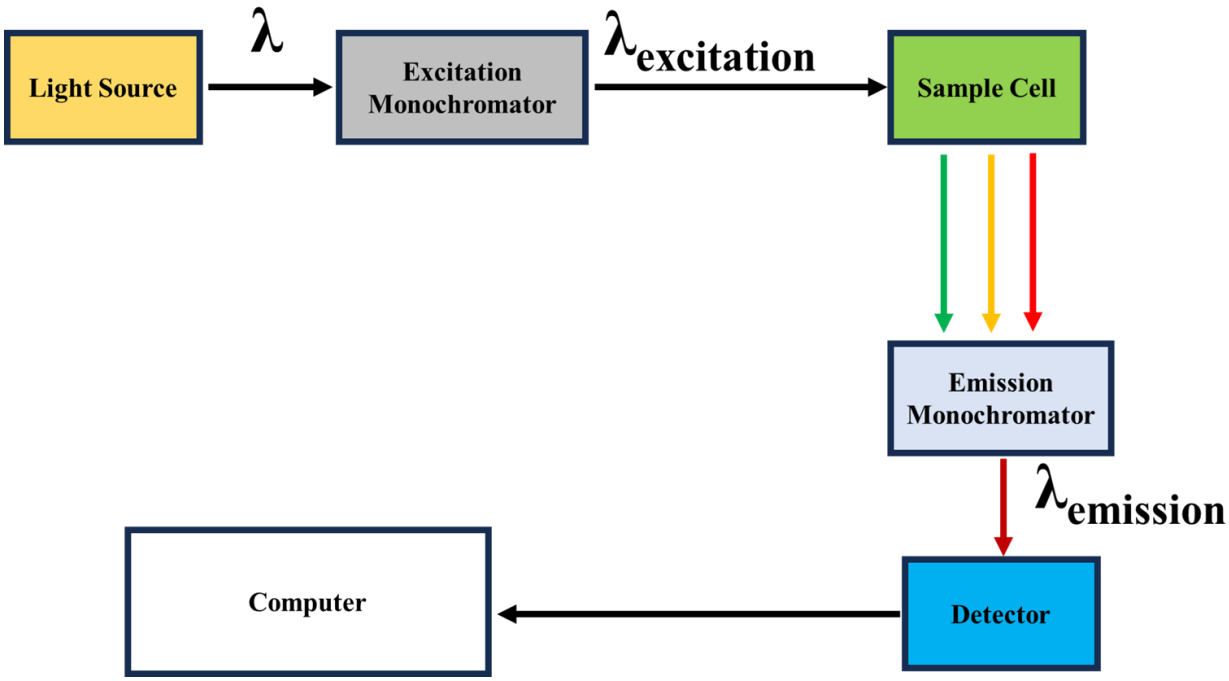

Figure 3.8: Schematic diagram of PL spectroscopy experimental setup

PL spectroscopy is a valuable tool for studying a wide range of materials, including biological samples, semiconductors, QDs, nanomaterials, and organic molecules. As a non-destructive method, it can be applied in various experimental conditions, such as different pressures, temperatures, and external stimuli, providing insights into the behavior of materials under diverse circumstances. PL spectroscopy has numerous applications: it characterizes semiconductor materials for optoelectronic devices like solar cells, LEDs, and lasers; investigates the electronic and structural properties of nanomaterials and QDs; studies photophysical processes in organic compounds and fluorescent dyes; analyzes defects and impurities in materials; and examines biological samples and biomolecules for biomedical research and diagnostics.

3.3.6. X-Ray Photoelectron Spectroscopy

The elemental composition, as well as the chemical and electronic states of materials, can all be ascertained using surface-sensitive analysis techniques such as X-ray photoelectron spectroscopy (XPS). It is extensively utilized in surface chemistry, materials science, and other scientific and industrial domains where surface analysis is essential.

The photoelectric effect, which uses X-rays to eject electrons off a material's surface, is the basis of XPS. Depending on the density and composition of the material, X-rays with adequate energy, usually in the range of a few hundred to a few thousand electron volts, can penetrate a sample's surface to a few nanometers. When an X-ray photon interacts with an electron in a sample, the electron may be ejected from the material. Upon ejection, the electron's kinetic energy indicates its binding energy to the atom from which it was expelled. The chemical environment and the atom's electronic structure determine the binding energy.

An electron energy analyzer detects the ejected electrons. XPS may detail a material's surface's elemental and chemical composition by measuring the electrons' kinetic energy and intensity. Peaks belonging to various elements found in the sample and peaks representing various chemical states of those elements comprise the energy spectrum produced by XPS analysis. The elemental composition, chemical bonding, oxidation states, and surface purity of materials may all be ascertained by analyzing XPS data. XPS analysis determines the composition and chemical environment of the sample's surface by comparing the observed binding energies with reference values for various elements and chemical states.

XPS offers several advantages, making it a highly valuable analytical technique. It is notably surface-sensitive, capable of analyzing only the top few nanometers of a material's surface, which is crucial for understanding surface chemistry. XPS provides quantitative elemental composition, allowing precise measurement of the elements present in a sample. Additionally, it can reveal the chemical bonding and oxidation states of the elements on the surface, providing detailed chemical

state information. XPS is also non-destructive, enabling the analysis of various materials, including solids, liquids, and thin films, without altering their composition or structure.

3.3.7. Solar Simulator with Keithley 2400 Source

A solar simulator is a device used to replicate the solar spectrum in a controlled environment, primarily for testing PV devices and other solar-related equipment on a laboratory scale. It plays a crucial role in evaluating the PV performance of a device by providing precise control over its electrical parameters. The solar simulator comprises several key components. The light source, which emits light across the solar spectrum, typically includes xenon arc lamps, metal halide lamps, or LEDs, all designed to mimic sunlight. The optical system ensures even light distribution over the solar cell's surface, using lenses, mirrors, and filters to collimate and diffuse the light for uniform illumination. The Keithley 2400 source meter applies controlled voltage and measures current to the solar cell, allowing characterization of the device's performance across various voltage and current levels.

In the measurement setup, the device under test is connected to the Keithley 2400 source meter. Voltage bias is applied, and the resulting current is measured. Control software automates the process of sweeping voltage and measuring current, interfacing with Keithley 2400 to set voltage levels, measure current, and collect data for analysis. The data analysis involves examining the solar cell's current-voltage (*I-V*) characteristics under different illumination conditions. This analysis enables the evaluation of crucial solar cell parameters such as short-circuit current or current density (I_{sc} or J_{sc}), open-circuit voltage (V_{oc}), maximum power point (MPP), fill factor (FF), and PCE. The solar simulator with the light source used for the *I-V* characteristics studies in this thesis is presented in Figure 3.9. The device's *J-V* curves were measured at a scan rate of 400 mV/s, with a range of -0.2 V to +1.2V. The fabricated devices had a total area of 0.1 cm^2 and are measured employing a mask of an active area of 0.03 cm^2.

Figure 3.9: Solar simulator and the light source used for the characterization of PSCs fabricated in the presented thesis

In laboratory setup, a xenon lamp equipped with appropriate filters is used to simulate air mass 1.5 spectra (AM1.5G) for *I-V* measurements. To generate *I-V* curves, the current passing through the device is measured as a function of the applied voltage, which is adjusted either in the dark or under illumination. In the dark, the *I-V* curves exhibit asymmetric, diode-like behaviour. Under the lighting, these curves shift vertically due to the generation of light-induced current. A typical *I-V* curve is presented in Figure 3.10.

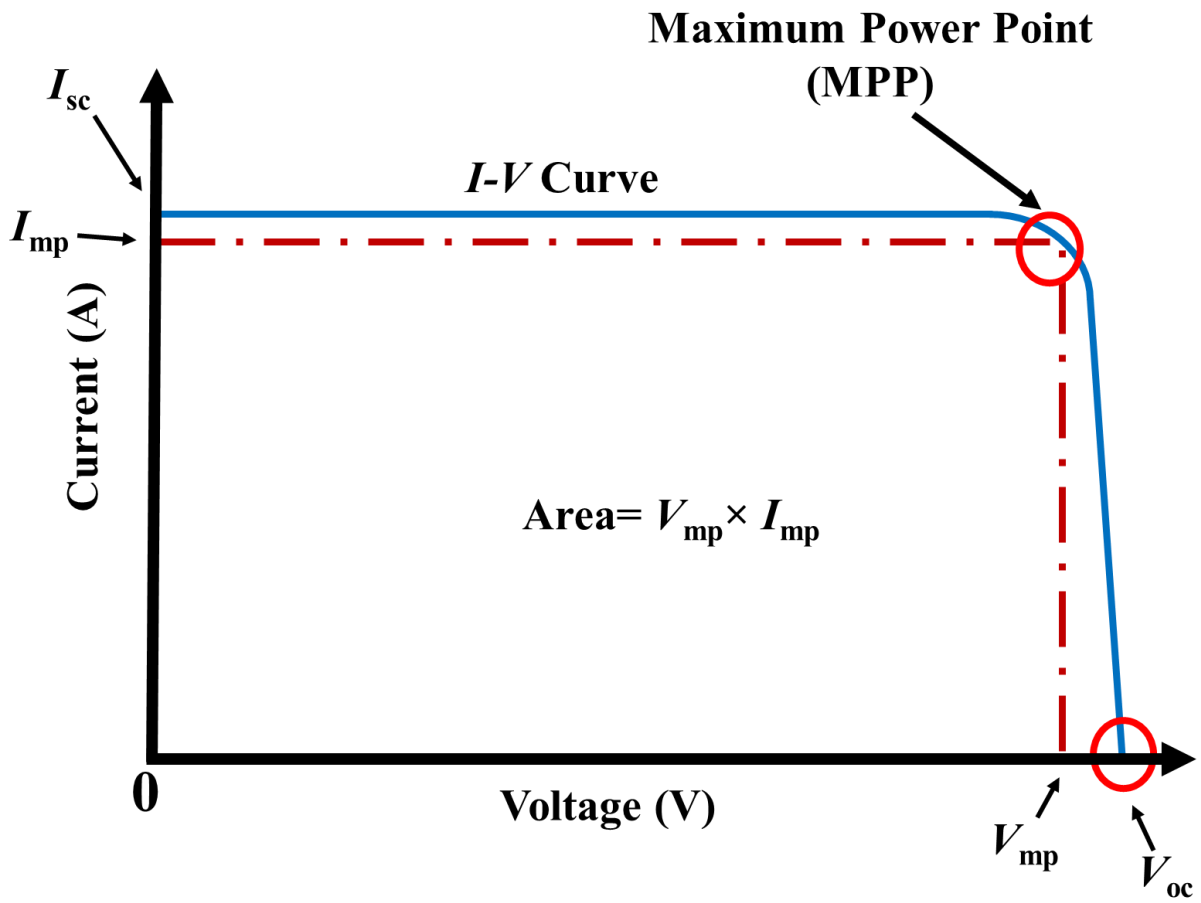

Figure 3.10: A schematic view of the typical *I-V* curve of a solar cell

A solar cell's *I-V* curve reveals plenty of data on its performance based on many crucial parameters:

- Short-Circuit Current:

When the voltage across a solar cell is zero, or when the cell is short-circuited, the current flowing through the cell is known as the short-circuit current (I_{sc}). It is the highest current the solar cell can generate in standard test circumstances, which include AM1.5G spectra, 1000 Wm^{-2} irradiance, and 25°C temperature. It is the y-intercept of the *I-V* curve.

The value of the I_{sc} depends on the light intensity (varies directly), the cell's surface area, and the quality of the semiconductor. It is usually changed to J_{sc}, obtained by dividing I_{sc} by the device's active area to make it consistent with the area.

- Open-Circuit Voltage:

The maximum voltage a solar cell can produce while its current is zero or when it is not connected to any load and no current is flowing is known as the V_{oc}. This is the highest voltage the solar cell can generate in conventional test circumstances, normally 1000 W m^{-2} irradiance, 25°C temperature, and AM1.5G spectra. It is the x-intercept of the *I-V* curve.

- Maximum Power Point:

The maximum value of the current and voltage ($I \times V$) product can be found at this point on the *I-V* curve, referred to as the maximum power point (MPP). It stands for the point at which the solar cell functions most efficiently. V_{mp} (voltage at MPP) and I_{mp} (current at MPP) are the coordinates of this location.

- Fill Factor

The FF is a measure of the "squareness" of the *I-V* curve and is defined as the ratio of the P_{max} to the product of V_{oc} and I_{sc}:

$$FF = \frac{P_{max}}{V_{oc}.I_{sc}} = \frac{I_{mp}.V_{mp}}{V_{oc}.I_{sc}} \quad (3.4)$$

- Efficiency:

A solar cell's efficiency or PCE is the ratio of output electrical power to the incident light power (P_{in}). It is given as:

$$PCE = \frac{P_{mpp}}{P_{in}} = \frac{V_{oc}.J_{sc}.FF}{P_{in}} \quad (3.5)$$

- Series Resistance

In solar cells, series resistance (R_s) refers to the cumulative resistance experienced by electrons as they go through the cell's layers, from the perovskite absorber layer to the external circuit. The main sources of R_s include contact resistance at layer interfaces, bulk resistance within the perovskite material, and resistance from charge transport layers, notably the ETL and HTL. Additionally, the resistance of metallic contacts and external connections adds to R_s. A greater R_s has a detrimental influence on the solar cell's performance by lowering the FF and perhaps decreasing the I_{SC}, limiting the maximum current flow and overall efficiency of the device. In a solar R_s can be estimated by from the slope of the *I-V* curve near the V_{oc}.

- Shunt Resistance

Shunt resistance (R_{Sh}) in solar cells refers to the unintended leakage paths that allow current to bypass the active junction, resulting in power loss. This leakage can arise due to several factors specific to the nature of perovskite materials and the structure of PSCs. Defects such as pinholes, cracks, and grain boundaries in the perovskite layer can create direct electrical pathways between the electrodes, lowering R_{Sh}. The quality of interfaces between the perovskite layer and adjacent transport layers is crucial, as poorly formed interfaces can introduce traps and defects that further contribute to lower R_{Sh}. Contaminants and impurities during the fabrication process can also lead to localized low-resistance areas, increasing the likelihood of current shunting. Additionally, PSCs are sensitive to environmental factors like moisture, oxygen, and UV light, which can degrade the perovskite material and form shunt paths over time, reducing the cell's performance. The method of deposition and quality control during fabrication significantly impact R_{Sh}, as uniformity and defect density are directly related to these factors. Low R_{Sh} negatively affects PSCs by reducing V_{oc}, lowering the FF, and decreasing overall efficiency.

3.3.8. External Quantum Efficiency Measurement System

An External Quantum Efficiency (EQE) measurement system is a setup used to characterize the spectral response of PV devices, by quantifying the ability of these devices to convert incident photons into electrical charge carriers. An EQE is also called incident-photon-to-collected-electron efficiency (IPCE) and can be expressed as follows:

$$EQE = \eta_{LHE}.\eta_{inj}.\eta_c \tag{3.6}$$

Where η_{LHE}, η_{inj}, and η_c are the light-harvesting, electron injection, and electron collection efficiencies, respectively.

The EQE of a solar cell is determined by measuring the J_{sc} as a function of the incident photon wavelength, while the J_{sc} under polychromatic light is calculated by integrating the product of EQE(λ) and incident flux density (F(λ)):

$$EQE = 1240 * \frac{J_{sc}(\lambda)}{\lambda.P_{in}} \tag{3.7}$$

$$J_{sc} = \int e.F(\lambda).EQE(\lambda)d\lambda \tag{3.8}$$

EQE measurements provide valuable insights into the performance of these devices across different wavelengths of light. A schematic setup of an EQE system is presented in Figure 3.10.

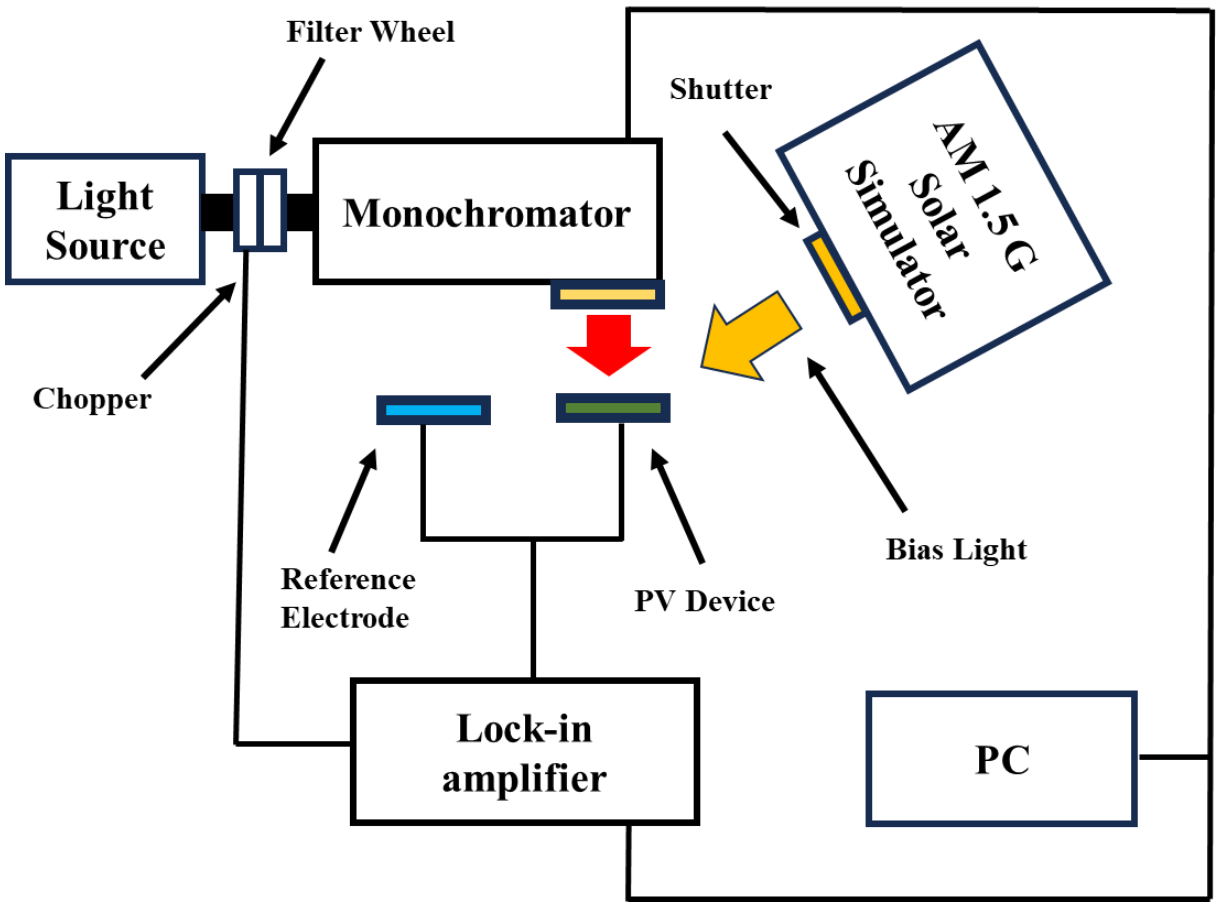

Figure 3.11: Schematic illustration of EQE measurement system adopted from ref [104]

Here's a brief overview of an EQE measurement system:

- Light Source:

The EQE measurement system utilizes a light source that covers a broad range of wavelengths, typically from UV to near-infrared (NIR) regions. This light source should be stable, uniform, and calibrated to provide accurate illumination levels across the spectrum of interest. Common light sources include xenon arc lamps, tungsten-halogen lamps, and LEDs.

- Monochromator:

A monochromator is used to select specific wavelengths of light from the broad spectrum emitted by the light source. It allows to measure the EQE of the device at different wavelengths. The monochromator typically consists of a grating or prism that disperses light and selects specific wavelengths for analysis.

- Optical Setup:

The monochromated light is directed onto the surface of the device under test. The optical setup may include lenses, mirrors, and filters to collimate, focus, and control the intensity of the light incident on the device. Ensuring that the light is evenly distributed across the device's active area is essential to obtain accurate EQE measurements.

- Device Under Test:

The PV device, such as a solar cell or photodetector, is mounted in the EQE measurement system. The device should be properly encapsulated to prevent external factors from affecting the measurements. The device's active area is exposed to the incident light, and the generated photocurrent is measured.

- Current Measurement:

The EQE measurement system includes a current measurement setup to quantify the photocurrent generated by the device in response to incident light. It typically involves a calibrated current meter or electrometer capable of measuring extremely low currents with high precision.

- Reference Detector:

A reference detector, such as a silicon photodiode with a known spectral response, may be used to calibrate the intensity of the incident light at different wavelengths. It allows to normalization of the EQE measurements and accounts for variations in the light intensity.

- Data Acquisition and Analysis:

The measured photocurrent values at different wavelengths are recorded and analyzed to calculate the device's EQE. Analysis software is used to process the data and generate EQE spectra for the device across the entire spectral range of interest. A photographic image of the EQE setup used for the PSCs in the presented work is shown in Figure 3.12.

Figure 3.12: A photographic image of the EQE setup used for the PSCs in the presented work

3.3.9. Open-Circuit Voltage Decay Measurement System

A Metrohm Autolab system has been used to measure V_{oc} decay (OCVD). The OCVD method examines the kinetics of charge carrier recombination and trap densities in semiconductor materials such as perovskites. The OCVD transient measurement is one of the straightforward methods to characterize the recombination losses in solar cells.[105] Figure 3.13 depicts an OCVD curve for two different PSCs. The charge carrier recombination lifetime (τ) of non-equilibrium photogenerated charge carriers can be estimated using the relation (3.9):

(3.9)

$$\tau = \frac{-kT}{q(\frac{dV_{oc}}{dt})}$$

Where *k*, *T*, and *e* are the Boltzmann's constant, temperature, and the positive elementary charge, respectively.

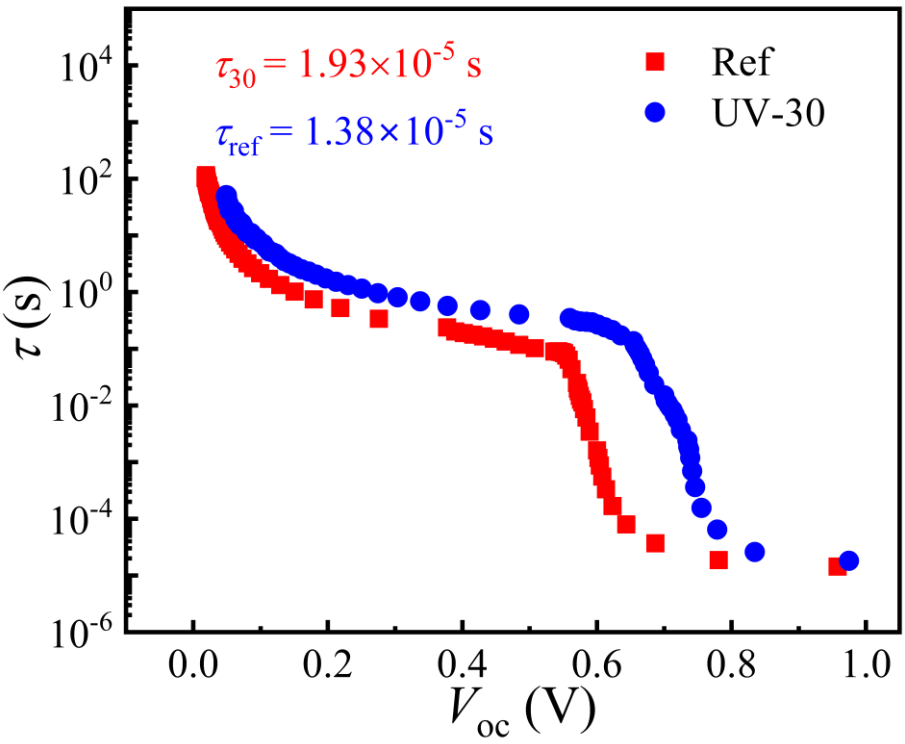

Figure 3.13: OCVD of two different PSC devices[32]

Using the Autolab PGSTAT302N for OCVD measurements in the context of PSCs is done as follows (Figure 3.14):

- Electrochemical Cell:

Usually, this entails assembling a two-electrode system with an appropriate reference electrode and the PSC acting as the working electrode. When taking measurements, the cell should be well-sealed and impervious to light to reduce external disruption.

- Experimental Setup:

The PSC is initially exposed to light during OCVD analysis to produce charge carriers (photoexcitation). After that, the light is abruptly cut off, and the open-circuit V_{oc} drop is tracked over time. It is possible to configure the Autolab PGSTAT302N for timely turning on and off the illumination, switch to open-circuit situations, and record the V_{oc} decay.

- Data Acquisition:

To record voltage decay data and control the potentiostat/galvanostat, use any relevant program, such as the Nova 2.0 program. Using the program, you may adjust the initial bias voltage, the duration of the bias application, and the voltage measurement interval during decay.

Figure 3.14: An auto measurement system for OCVD measurements

Chapter#4

Synthesis and Optimization of SnO_2 Quantum Dots-based Electron Transport Layer Ink

4.1. Materials

GreatCell Solar supplied the purchased methylammonium iodide (MAI, 99.995%). Merck supplied the following products: acetonitrile (ACN, 99.80%), PbI_2 (99%), bis(trifluoromethane)sulfonimide lithium salt (Li-TFSI, 99%), chlorobenzene (CB, 99.80%), 4-tert-Butylpyridine (4tBp, 98%), methylamine solution (MA, 33 wt% in absolute ethanol), and acetone (99.80%). Potassium hydroxide pellets (KOH, 85%) and Spiro-MeOTAD (99.50%) were acquired from Lumtec and ACS reagent, respectively. A local source supplied the ethanol (96.3%) and propanol (IPA, 99.80%). We purchased Au (99.99%) from Kurt J. Lesker. None of the chemicals were treated; they were all utilized just as received.

4.1.1. Synthesis of SnO_2 Quantum Dots

QDs are nanoscale semiconductor particles that exhibit quantum mechanical properties.[106] The behavior of excitons in bulk materials and QDs differs significantly due to the effects of quantum confinement. In bulk semiconductors, excitons, which are bound states of electrons and holes, can move freely through the crystal lattice. The size of the exciton in bulk materials is typically characterized by the Bohr exciton radius, which depends on the material's properties, such as the dielectric constant and the effective masses of the electron and hole. Energy levels in bulk materials form continuous bands, allowing electrons and holes to occupy any state within the conduction and valence bands, respectively, with the energy difference between these bands being the bandgap energy. The exciton binding energy in bulk materials is relatively low, meaning the exciton is weakly bound and can be easily dissociated into free charge carriers at room

temperature. Optically, excitons in bulk materials contribute to absorption and emission properties, with the absorption edge closely corresponding to the material's bandgap and the absorption spectrum generally being continuous, starting at the bandgap.

In contrast, in QDs, the size of the material is comparable to or smaller than the Bohr exciton radius, leading to significant spatial confinement of the exciton. This confinement restricts the movement of the electron and hole within the QD, causing the energy levels to become discrete rather than continuous. The quantum confinement effect increases the effective bandgap, as more energy is required to confine the electron and hole within the small volume of the QD. Consequently, the exciton binding energy in QDs is higher than in bulk materials due to the enhanced Coulomb interaction in the confined space, making excitons more stable even at higher temperatures. The optical properties of QDs are also distinct; they exhibit sharp absorption and emission peaks corresponding to transitions between quantized energy levels. Additionally, the bandgap in QDs can be tuned by altering their size, with smaller QDs having larger bandgaps (blue-shifted emission) and larger QDs having smaller bandgaps (red-shifted emission). These differences, including discrete energy levels, increased bandgap, higher exciton binding energy, and size-dependent optical properties, underlie the unique properties of QDs, making them suitable for various applications in optoelectronics, such as QD solar cells, LEDs, and bioimaging.

In the context of ETL, QDs can result in fewer defects, reduced material consumption, and enhanced layer compactness. Various factors can influence their formation, including precursor concentration, temperature, and processing conditions. The concentration of SnO_2 QDs in ETL inks plays a pivotal role in determining the electrical conductivity of resulting ETL films. Elevated concentrations often yield heightened electrical conductivity and can result in enhanced charge transportation from the perovskite layer to TCO. Attaining optimal concentrations of QDs can effectively minimize charge recombination losses and improve charge extraction efficiency, thereby bolstering the device's overall performance. Moreover, variations in the concentration of QDs can significantly influence the morphology and thickness of ETL films.[61] Higher

concentrations up to a limit tend to produce thicker films with a denser packing of QDs, altering surface roughness, porosity, and interfacial properties with the perovskite layer. Additionally, the concentration of QDs in ETL inks can impact the optical properties of ETL films, influencing light absorption, transmission characteristics, as well as light scattering and reflection within ETL films, thereby potentially shaping the overall optical performance of solar cells.[107]

Synthesis of SnO_2 QDs is carried out using a solvothermal technique. The solvothermal technique involves preparing a $SnCl_2 \cdot 2H_2O$ (1 mol) solution as a precursor in ethanol (10 mL) as a solvent. The preparation of the solution is carried out with sufficient oxygen supply. The precursor solution was stirred using a magnetic stirrer for 4 h. The stirred solution containing QDs was transferred into a 50 mL Teflon liner, and then the Teflon liner was inserted into a stainless-steel autoclave. The solvothermal treatment was carried out at 150 °C for 24 h in a muffle furnace. Upon completion, the furnace was allowed to cool down to room temperature, and once it reached room temperature, the solution with synthesized SnO_2 QDs was transferred to a centrifuge tube. The obtained solution was precipitated using centrifugation to obtain SnO_2 QDs. The obtained residue (SnO_2 QDs) was consecutively washed with deionized (DI) water, acetone, and ethanol. After washing, the SnO_2 QDs were transferred into the oven to dry at 80 °C for 12 hours. The whole process is shown in the flow chart presented in Figure 4.1.

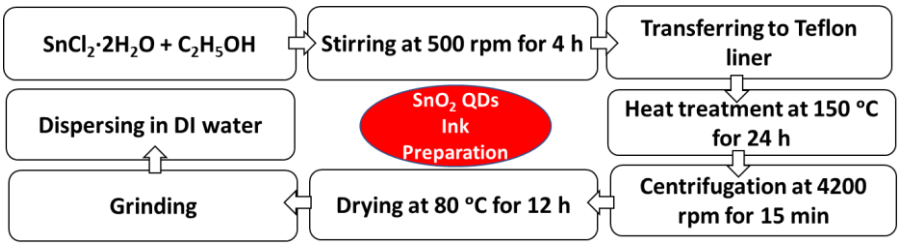

Figure 4.1: Schematic diagram outlining preparation of SnO_2 QD ETL ink

4.1.2. Ink Preparations

Concentration optimization of the SnO_2 QDs in aqueous media is done by dispersing them with the help of KOH. The dried QDs powder is ground and dispersed in different wt.% in DI

water with KOH as a pH mediator. The filtration of the colloidal solution is then carried out using a PTFE syringe filter of 0.45 µm pore size and then diluted with DI water to acquire the ink solutions with 1, 1.5, 2, 2.5, and 3 wt.% of SnO_2 QDs. The perovskite ($MAPbI_3$) ink is prepared using MAI and PbI_2 precursors and is dissolved in MA and ACN, serving as solvents. Initially, 1 mol of each PbI_2 and MAI are dissolved in 0.7 mL of MA under 460 rpm constant stirring at 70 °C for an hour using a hot plate with a magnetic stirrer. After this, the solution is diluted with the addition of 0.7 mL of ACN and kept stirring for three more hours. Then, the final perovskite ink solution is filtered using a 0.45 µm pore size PTFE filter. Using a vortex shaker, the HTL ink is prepared using 45 mg of Spiro-MeOTAD dissolved in 1 ml of CB. After 1 h of shaking, the additives such as lithium salt solution (Li-TFSI in ACN at 520 mg mL^{-1}) and 4tBp are added to the Spiro-MeOTAD/CB solution in 17.5 µL and 28.8 µL quantities, respectively. The prepared HTL ink solution is then filtered using a PTFE syringe filter for further use. The whole process of the ink synthesis is presented in the form of a flowchart in Figure 4.2.

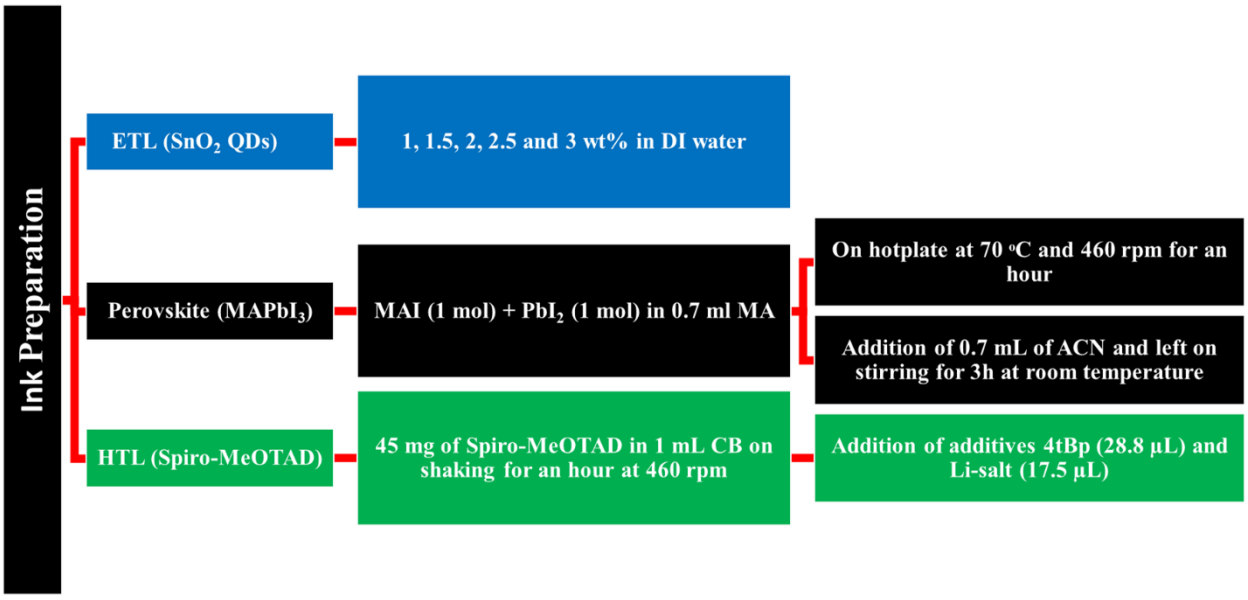

Figure 4.2: Schematic diagram showing ETL, perovskite, and HTL inks preparation steps

4.1.3. Device Fabrication

To fabricate SDC-FPSCs, the PET/ITO substrate is initially cleaned through a series of ultrasonic baths. This process includes ten minutes each in DI water with detergent, clean DI water, acetone, and IPA. After cleaning, the substrates undergo a 15-minute UV-ozone treatment and are dried using compressed air. The next step involves printing the functional layers, where the as-synthesized SnO_2 QD inks are SDC on the PET/ITO substrates using a slot-die head connected to a syringe pump. Following the deposition of the ETLs, the substrates are annealed in an oven at 140 °C for 30 minutes, after which they are allowed to cool to room temperature. Once cooled, the substrates are secured onto the chuck of the slot-die coater, and the perovskite ink is deposited onto the SDC-ETL layer via slot-die coating. Post perovskite deposition, the substrates are then subjected to a 10-minute annealing treatment at 100 °C. The HTL ink is then coated onto the perovskite layer using a clean slot-die head. Immediately following the HTL layer deposition, the substrates are left in an oxygen environment for 12 hours. All functional layers are deposited in an ambient atmosphere, with the chuck maintained at 25 °C and a relative humidity (RH) of approximately 20-25%.

After 12 hours, the top electrodes are deposited using a Mini SPECTROS vacuum thermal evaporator (Kurt J. Lesker, USA) with a shadow mask. The Au contacts, 80 nm thick, serve as the back electrodes. Figure 4.3 illustrates an energy level diagram for the SDC-FPSCs and a schematic of the device fabrication process. The final device structure is PET/ITO/SnO_2/$MAPbI_3$/Spiro-MeOTAD/Au. The same protocols are followed to fabricate reference devices, except the ETL deposition step is omitted, resulting in a device structure of PET/ITO/$MAPbI_3$/Spiro-MeOTAD/Au.

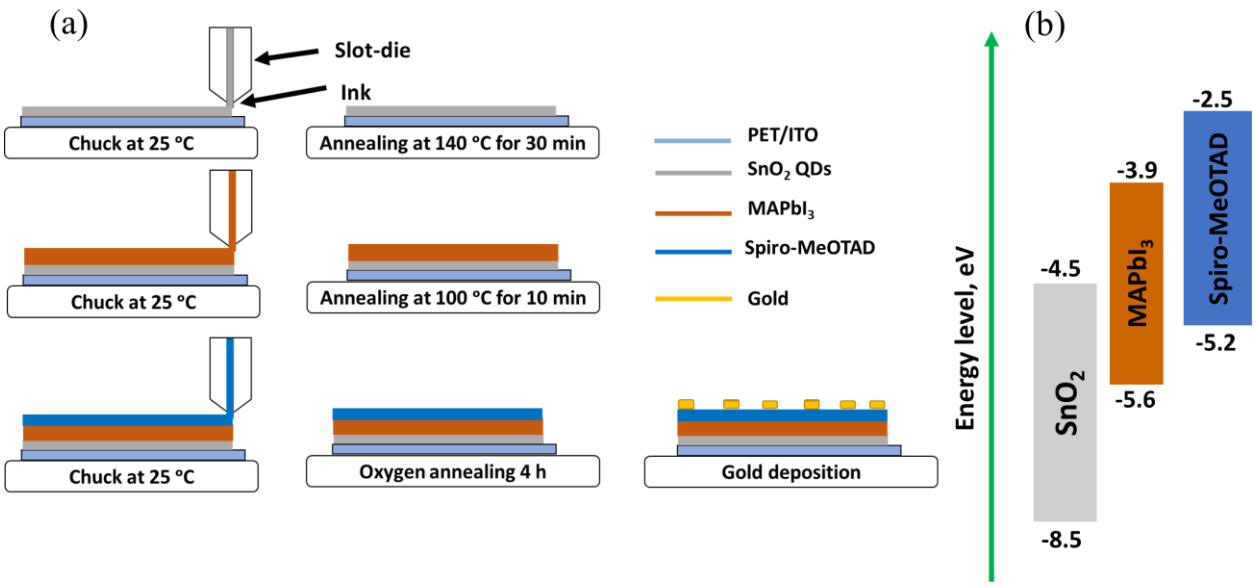

Figure 4.3: Schematic diagram illustrating (a) fabrication of FPSCs and (b) energy band alignment in devices

4.2. Results

4.2.1. Crystallographic Analysis of SnO_2 Quantum Dots

To scrutinize their structural properties, we conducted XRD measurements on freshly synthesized SnO_2 QDs. The XRD pattern of the SnO_2 QDs is presented in Figure 4.4, revealing major diffraction peaks at $2\theta = 26.7°$, 34.05°, and 52.1° referring to the reflections of the incident rays from the (110), (101), and (211) lattice planes of SnO_2, respectively. Notably, all peaks exhibit close agreement with JCPDS Data Card# 77-0452, indicating the presence of SnO_2 in its tetragonal rutile crystalline phase.[108–110] The reported XRD pattern aligns well with the findings of Zhu et al., reporting the hydrazine hydrate mineralized SnO_2 QDs synthesis via a hydrothermal route.[111]

The crystal lattice parameters *a* and *c* were determined to be 0.474 nm and 0.322 nm respectively. Additionally, the average crystallite size employing Scherrer's formula of the SnO_2 QDs was estimated to be around 2.4 nm, computed from the two major peaks at (110) and (211).[112,113]

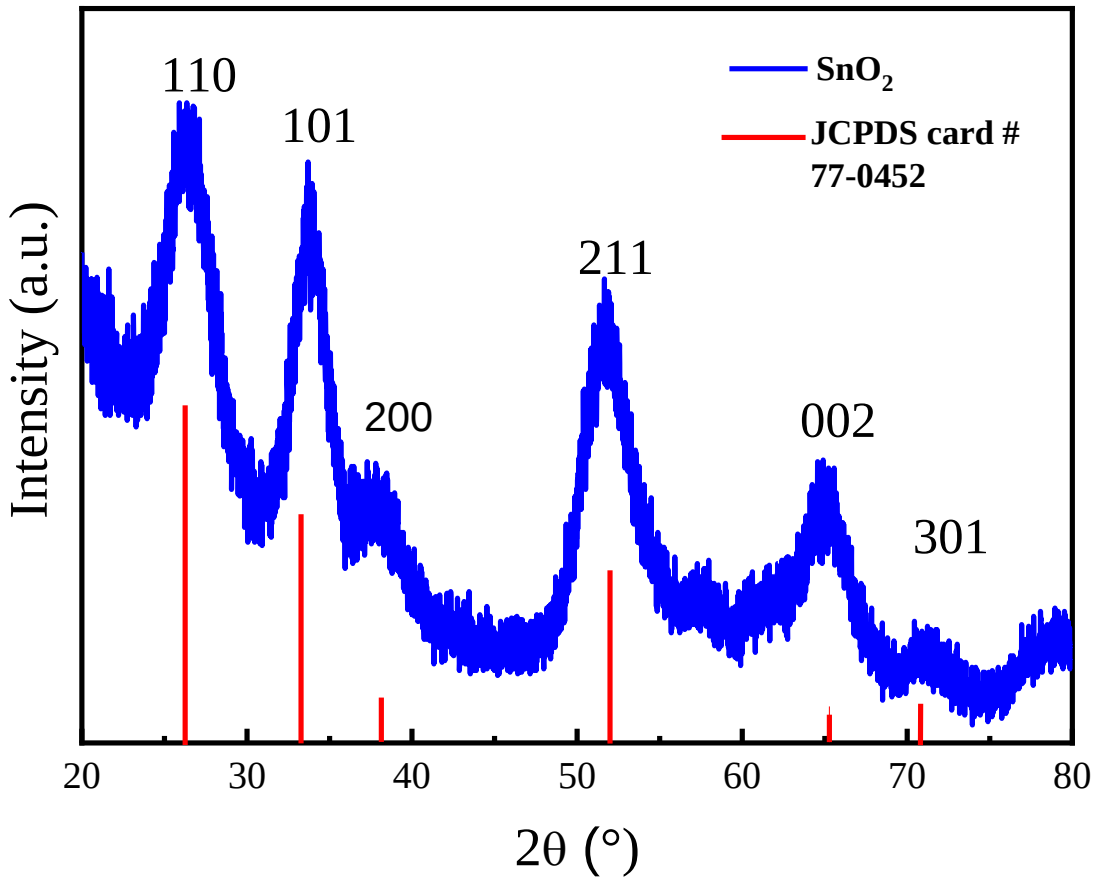

Figure 4.4: XRD pattern of as-synthesized SnO_2 QDs

4.2.2. Transmission Electron Microscopy

We measured the particle size of the as-prepared SnO_2 QDs by acquiring transmission electron micrographs. As deduced from the TEM images in Figure 4.5, the average particle size is around 2.4 nm, and is in well agreement with the estimated crystallite size from the XRD data (Figure 4.4).[111] In addition, the TEM image reveals a crystalline structure, as demonstrated by the observable fringes in Figure 4.5b, and a uniform size distribution of the synthesized particles, as seen in Figure A4.1 of the Appendix. As shown in the inset picture of Figure 4.5b, the estimated *d*-spacing value from the TEM image of the SnO_2 QDs is around 0.33 nm, corresponding to the {110} planes of SnO_2. Given that the resulting SnO_2 NPs are lesser in size than the Bohr excitonic radius (about 2.7 nm) for SnO_2, it is plausible to assume that the synthesized particles are SnO_2 QDs.[114] Similar to the XRD result, the TEM results are more or less identical to those reported by Zhu et al.[111]

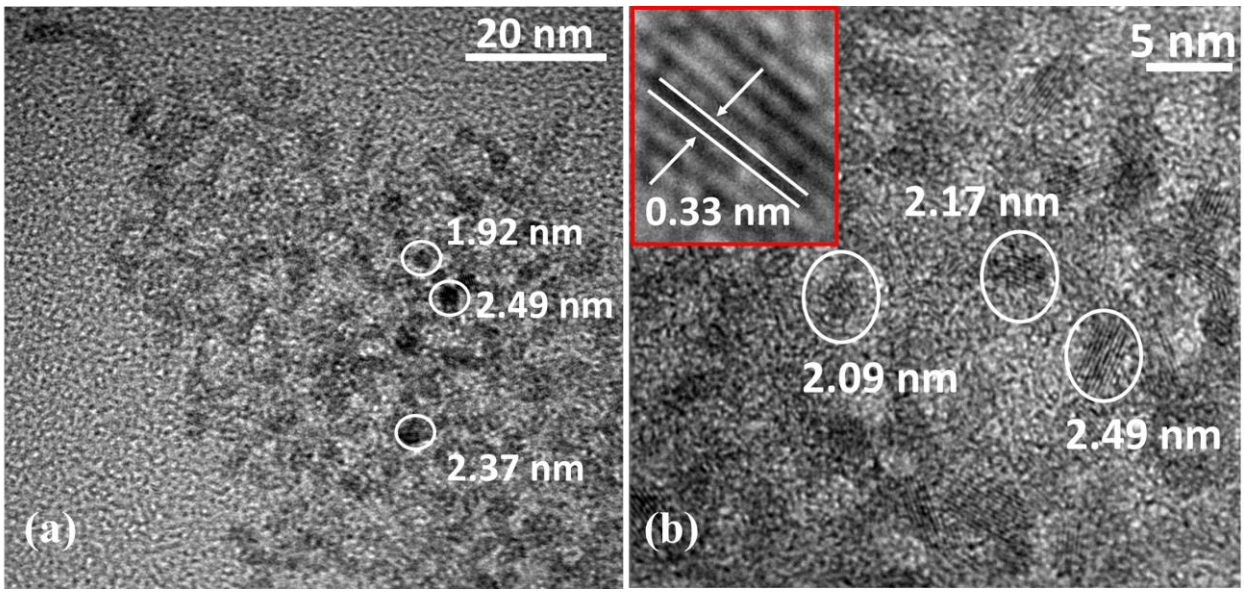

Figure 4.5: TEM micrographs of as-synthesized SnO_2 QDs at (a) 40 kX and (b) 1500 kX magnifications. The inset in (b) highlights the fringes and *d*-spacing of SnO_2 QDs

4.2.3. Optical Analysis

Using a UV-Vis spectrometer, we investigated the optical properties of ETLs fabricated using SnO_2 inks that contained varying concentrations of SnO_2 QDs. The transmittance spectra of SDC ETLs on top of bare glass across the wavelength range of 280–900 nm is presented in Figure 4.6. When the UV-Vis spectra of several ETLs are compared, it is apparent that the ETL made with 1 wt.% SnO_2 QD ink has the maximum transmittance, continuously surpassing 90% throughout the measurement range. Next in line is the ETL deposited using 2 wt.% SnO_2 QD ink. It had the 2nd-highest transmittance, somewhat higher than the ETL deposited using 1.5 wt.% SnO_2 QD ink. The ETL made with 3 wt.% SnO_2 QD ink had a comparable UV-Vis transmittance spectrum to the 1.5 wt.% SnO_2 QD ink-based ETL. Interestingly, the ETL with 2.5 wt.% SnO_2 QD ink had the lowest transmittance of the detected variants. As anticipated, thicker ETL films are formulated by increasing the concentration of SnO_2 QDs in the inks, according to the results of the UV-Vis transmittance measurements of ETLs formed with 1, 2, and 3 wt.% SnO_2 QD inks. The slight discrepancies between the ETLs made using 1.5 and 2.5 wt.% SnO_2 QD inks may be due to slight variations in the ink preparation and deposition methods, which might affect the final film

thicknesses. Notably, each ETL has a transmittance level of over 90%, which is beneficial for SDC-FPSC devices i.e., high light transmittance of these ETLs allows more photons to reach the perovskite layer in resulting SDC-FPSCs, boosting the generation of charge carriers.[115–118]

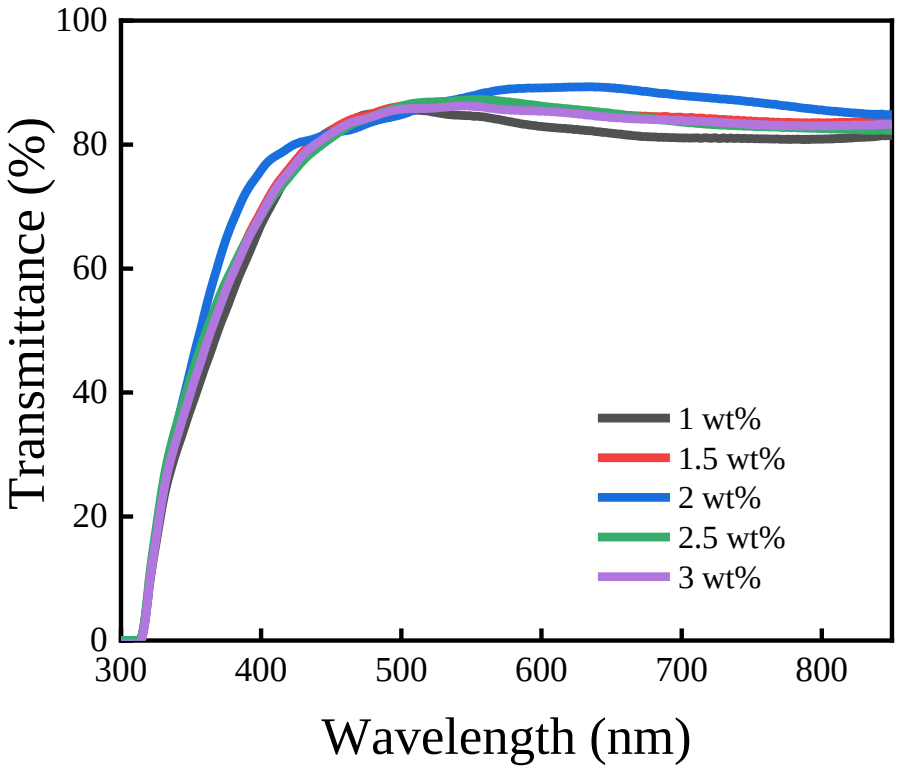

Figure 4.6: UV-Vis transmittance spectra of glass/ETLs with varying SnO_2 QDs concentrations in ETL ink

4.2.4. Scanning Electron Microscopy

The thickness of the functional layers in the device is ascertained using SEM imaging. Figure 4.7a displays the cross-section of the ETL on glass/FTO, made with a 2 wt.% SnO_2 QD ink, showing a thickness of ~ 25 nm. Additional SEM images of the ETL cross-sections fabricated with varying concentrations of SnO_2 QD ink (1, 1.5, 2.5, and 3 wt.%) are provided in Figure A4.2 in the Appendix. These images reveal that the ETL thickness increases from 16 nm to 35 nm as the SnO_2 QD concentration increases. The variation in ETL thickness significantly impacts the device performance, making it crucial to determine the optimal SnO_2 QD ink concentration for

achieving the best balance between the efficiency and stability of the final device. All three SDC-FPSC functional layers on glass/FTO are displayed in Figure 4.7b. The $MAPbI_3$ and the HTL are about 600 and 200 nm thick, respectively, whereas the ETL is only around 25 nm thick (see inset picture). Figure 4.7c shows the SEM top-view of ITO on top of PET substrate, ITO crystals can be seen clearly. The SEM top view image of SDC 2 wt.% SnO_2 QD ETL on a PET/ITO substrate is displayed in Figure 4.7d.

Given that there are no discernible pinholes in the ETL that allow the surface of the ITO to be observed, the picture suggests that the SnO_2 QDs have uniformly covered the PET/ITO substrate. One may conclude that the surface of the PET/ITO substrate is evenly covered with SnO_2 QDs by comparing Figures 4.7c and d. Optimal device operation necessitates ETL to cover the TCO layer uniformly.

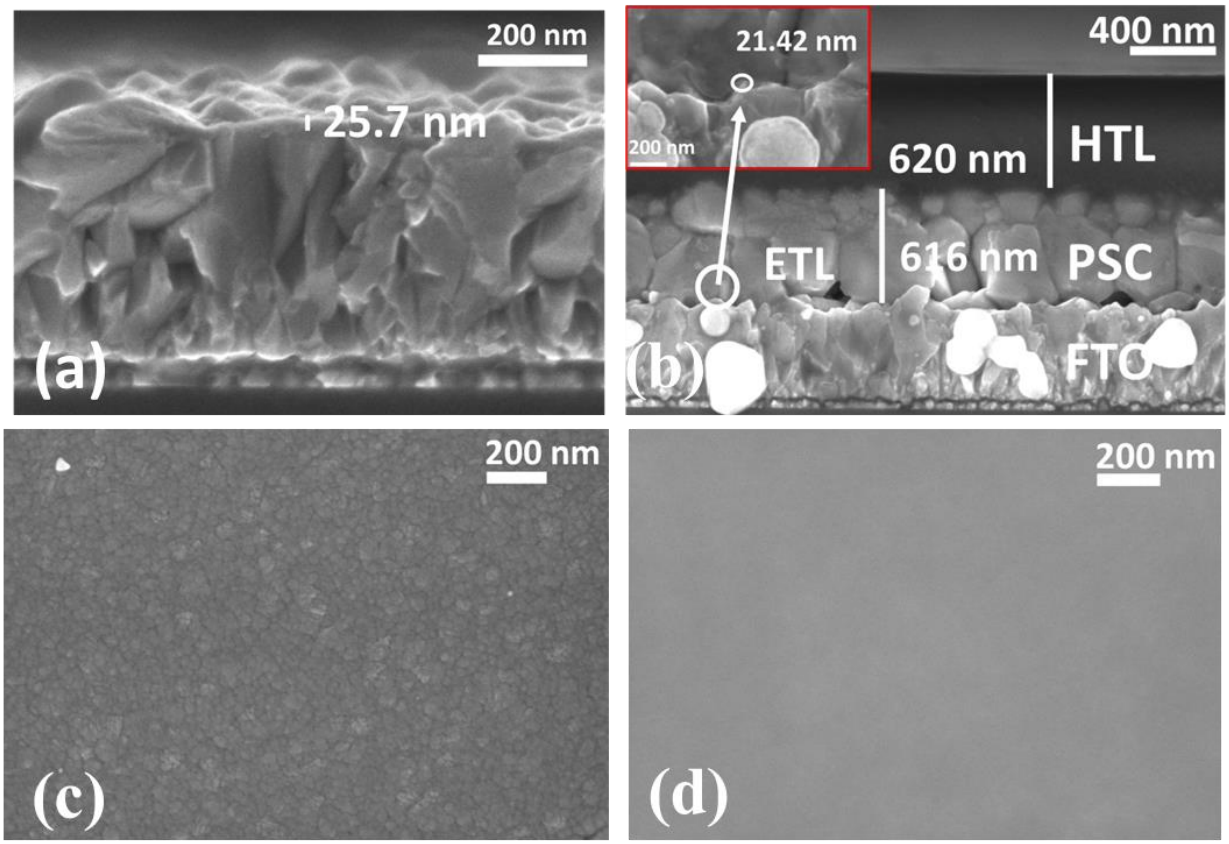

Figure 4.7: SEM cross-section images of (a) SnO_2 QD-based ETL on glass/FTO and (b) device functional layers on glass/FTO. The inset image in (b) shows the presence of ETL between the

FTO and $MAPbI_3$ layers. SEM top-view images of (c) PET/ITO and (d) SnO_2 QD-based ETL on PET/ITO at 100 kX magnification

4.2.5. Device Analysis

SDC-FPSCs fabricated on PET/ITO substrates, both with and without the ETLs, are developed using SnO_2 QD solutions of varying concentrations of 0, 1, 1.5, 2, 2.5, and 3 wt.% to determine the optimal concentration of SnO_2 QDs in the ETL ink. Multiple devices are fabricated using each of the SnO_2 QDs concentrations in the ETL ink to conduct comprehensive assessments. Henceforth, the ETLs formulated with SnO_2 QDs at concentrations of 0, 1, 1.5, 2, 2.5, and 3 wt.% are denoted as ETL0, ETL1, ETL2, ETL3, ETL4, and ETL5, respectively. The fabricated devices undergo a rigorous testing process. For each ETL variation (ETL0, ETL1, ETL2, ETL3, ETL4, and ETL5), a statistical analysis of PV device performance parameters for the top 40 best-performing devices is carried out.

Figure 4.8 illustrates PV parameters obtained from reverse scans, including V_{oc}, J_{sc}, FF, PCE, R_s, and R_{Sh} for ETL0, ETL1, ETL2, ETL3, ETL4, and ETL5. Figure 4.8a shows that for ETL0, J_{sc} is approximately 1.12 mA cm^{-2}, which rises to 7.7 mA cm^{-2} for ETL1. Subsequently, ETL2 records a J_{sc} of 12.95 mA cm^{-2}, about 40% higher than ETL1. The average J_{sc} for ETL3 (13.28 mA cm^{-2}) shows a slight increment over ETL2, while ETL4 records the highest average J_{sc} of about 14.31 mA cm^{-2}. However, ETL5 experiences a slight drop in average J_{sc} compared to ETL4.

Figure 4.8b reveals a gradual increase in average V_{oc} values from ETL0 to ETL3, with ETL3 registering around 0.93 V, approximately 13% higher than ETL1. However, subsequent devices with higher SnO_2 QDs in ETL inks (ETL4 and ETL5) gradually decrease the average V_{oc} values. Such fluctuations in V_{oc} and J_{sc} with changes in SnO_2 QD concentration in the ETL inks may stem from variations in ETL thickness and the morphology affecting the carrier recombination processes and R_s in the devices.[119] The rise in SnO_2 QD concentration in the ETL

ink correlates with higher R_s values in resulting devices, as depicted in Figure 4.8e. Conversely, increased R_{Sh} values with higher SnO_2 QD concentrations indicate denser ETLs with fewer pinholes, potentially reducing charge carrier back-reaction. This could explain the initial rise in average V_{oc} and J_{sc} values from ETL0 to ETL3. The subsequent decline in average J_{sc} in ETL5 may result from suboptimal ETL thickness hindering photon transmission. The average V_{oc} values in ETL4 and ETL5 may suffer from increased charge recombination at the ETL/$MAPbI_3$ interface due to elevated device R_s.[120]

Figure 4.8c shows a notable trend in the average values of the FF across ETL0 to ETL5. Initially, there's a sharp rise in FF from ETL0 to ETL3, followed by a gradual decline for ETL4 and ETL5. This pattern mirrors the trends observed in V_{oc} and J_{sc}. The substantial increase of approximately 37% in average FF value is particularly noteworthy when doubling the SnO_2 QD in the ETL ink of 1 wt.% (ETL1) to 2 wt.% (ETL3). FF is a multifaceted phenomenon influenced by various device parameters. The initial surge in average values of FF from ETL0 to ETL3 may be attributed to reduced charge carrier recombination and potentially enhanced ETL electrical conductivity due to increased thickness.[121–123] However, for ETL4 and ETL5, the decline in FF could be linked to rising R_s in the devices, which may impede efficient charge transport and collection within the solar cell structure.[120]

The analysis of V_{oc}, J_{sc}, and FF collectively determines the overall trend in the average PCE concerning the variations in SnO_2 QD concentration in ETL inks. As anticipated and aligned with the shifts in V_{oc}, FF, and, to some extent, J_{sc}, the average PCE values of devices exhibit an increase from ETL0 to ETL3, followed by a subsequent decrease. Remarkably, the average PCE in ETL3 surpasses that in ETL1 by nearly threefold, largely attributed to substantial enhancements in average J_{sc} (approximately 1.8-fold) and FF (approximately 1.5-fold) values upon doubling the concentration of the SnO_2 QD in the ETL ink from 1 wt.% (ETL1) to 2 wt.% (ETL3).

Devices incorporating ETLs (ETL1, ETL2, ETL3, ETL4, and ETL5) demonstrate significantly higher performances compared to those lacking an ETL (ETL0), underscoring the indispensability of an ETL layer in SDC-FPSCs to achieve optimal device performance. A comprehensive summary of PV parameters is provided in Table 4.1. Notably, commercially available metal oxide inks, such as ZnO, SnO_2, and NiO, typically possess solid metal oxide content ranging around 2-2.5 wt.%. Considering this industry standard, the observed trends in this study appear to be reasonable and aligned with commercially available inks.[124–126]

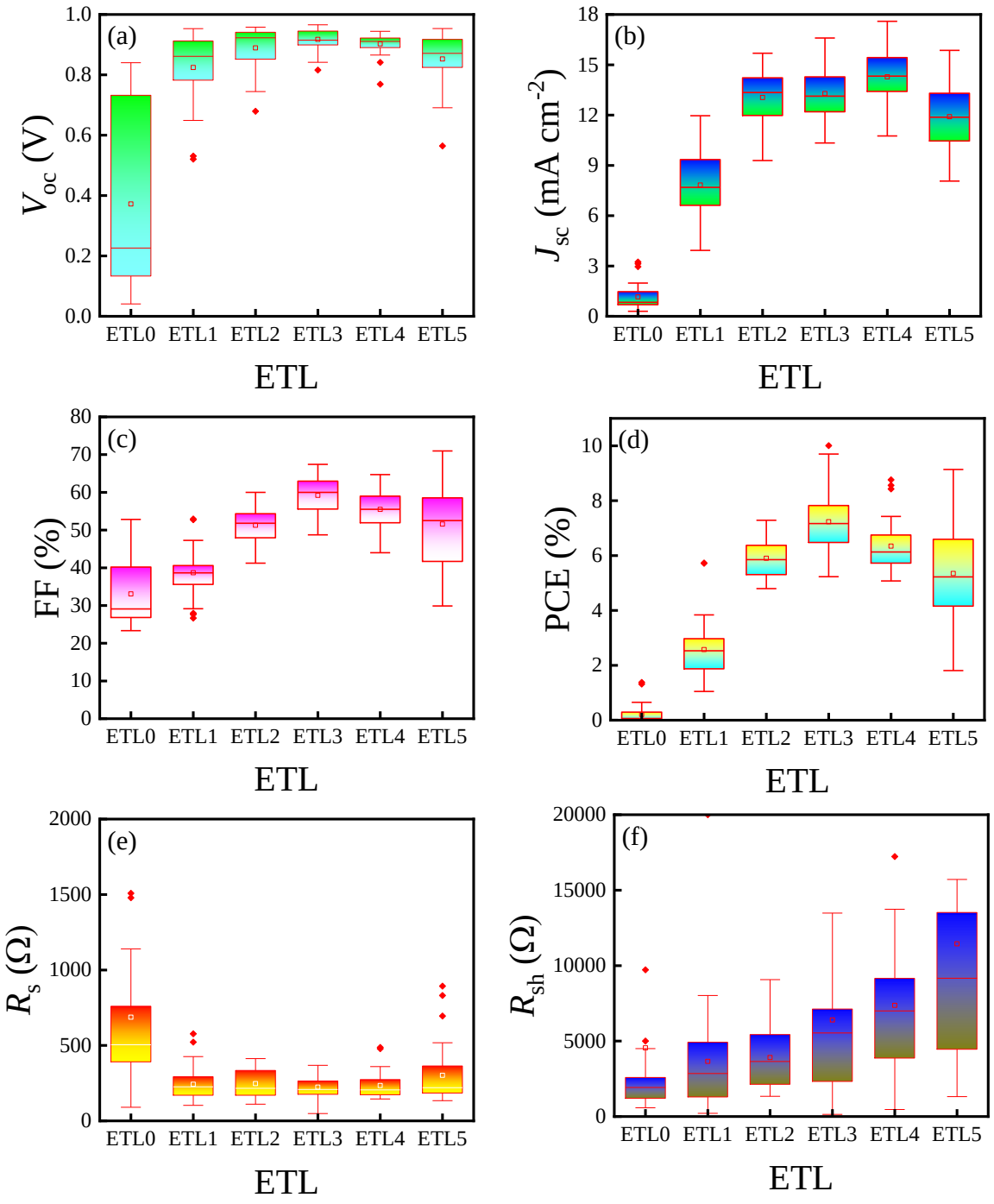

Figure 4.8: Comparison of statistical values for (a) V_{oc}, (b) J_{sc}, (c) FF, (d) PCE, (e) R_S, and (f) R_{Sh} in FPSCs based on ETL0, ETL1, ETL2, ETL3, ETL4, and ETL5

Table 4.1: Comparison of statistical solar cell performance parameters of 40 well-performing devices with various ETLs

ETLs	Scan	J_{sc} (mA cm^{-2})	V_{oc} (V)	FF (%)	PCE (%)	R_S (Ω)	R_{Sh} (kΩ)
E0 (ref.)	Reverse	1.2 ± 0.11	0.4 ± 0.05	33.1 ± 1.33	0.2 ± 0.05	689.6 ± 119	4.6 ± 2.4
	Forward	0.9 ± 0.10	0.3 ± 0.05	27.9 ± 0.48	0.1 ± 0.03	994.8 ± 252.2	16.6 ± 10.4
E1 (1 wt%)	Reverse	7.7 ± 0.29	0.8 ± 0.02	38.7 ± 0.85	2.5 ± 0.16	238.4 ± 16.6	3.7 ± 0.5
	Forward	5.6 ± 0.26	0.2 ± 0.02	28.9 ± 0.72	1.2 ± 0.09	447.8 ± 121.1	3.9 ± 0.4
E2 (1.5 wt%)	Reverse	12.9 ± 0.49	0.9 ± 0.01	51.2 ± 1.6	5.8 ± 0.3	246.6 ± 14.1	3.9 ± 0.3
	Forward	10.1 ± 0.57	0.8 ± 0.01	36.3 ± 1.4	3.0 ± 0.2	230.7 ± 11.4	3.7 ± 0.3
E3 (2 wt%)	Reverse	13.3 ± 0.22	0.9 ± 0.01	59.2 ± 0.7	7.23 ± 0.2	222.7 ± 11.2	6.3 ± 1.4
	Forward	8.5 ± 0.35	0.9 ± 0.01	28.3 ± 0.9	2.15 ± 0.1	221.3 ± 10.3	3.3 ± 0.3
E4 (2.5 wt%)	Reverse	14.3 ± 0.63	0.9 ± 0.01	53.1 ± 1.8	6.98 ± 0.5	232.6 ± 12.9	7.4 ± 1.1
	Forward	10.3 ± 0.64	0.8 ± 0.01	32.5 ± 1.4	3.08 ± 0.3	223.5 ± 15.4	4.2 ± 0.4
E5 (3 wt%)	Reverse	11.8 ± 0.30	0.8 ± 0.02	50.6 ± 1.9	5.16 ± 0.3	297.2 ± 28.6	11.7 ± 1.7
	Forward	7.5 ± 0.30	0.8 ± 0.02	25.4 ± 0.8	1.50 ± 0.1	271.0 ± 27.4	5.4 ± 0.8

From a statistical standpoint, ETL3 is the most suitable option for fabricating well-performing devices. The best-performing champion device is achieved using the ETL3. Figure 4.9a illustrates the champion device's current density-voltage (*J-V*) curves. It demonstrates V_{oc}, J_{sc}, and FF values of approximately 0.95 V, 17 mA cm^{-2}, and 63% during the reverse scan, resulting in a PCE of ~10%. PV performance parameters obtained from both the forward and reverse *J-V* scans are detailed in Table 4.2. Additionally, the champion devices' *J-V* curves employing ETL0, ETL1, ETL2, ETL4, and ETL5 ETLs, along with their corresponding PV parameters, are presented in Figure A4.3 of the Appendix.

The champion device utilizing ETL3 undergoes an EQE measurement to assess its spectral response. As depicted in Figure 4.9b, the device exhibits an EQE spectrum characteristic of $MAPbI_3$-based PSCs. The device maintains relatively consistent EQE values of approximately 50% all over the visible spectrum. The integrated value of J_{sc} derived from the champion device

EQE spectrum with ETL3 is approximately 11 mA cm^{-2}, comparable to the J_{sc} obtained from the forward scan direction *J-V* curve (refer to Table 4.2). Figure A4.4 in the Appendix showcases the champion devices EQE spectrum by employing ETL0, ETL1, ETL2, ETL4, and ETL5 ETLs. These devices attain maximum EQE values around 1, 45, 25, 35, and 30%, respectively. Notably, the trends of the EQE spectra across the visible range are not as uniform as observed in the ETL3 champion device.

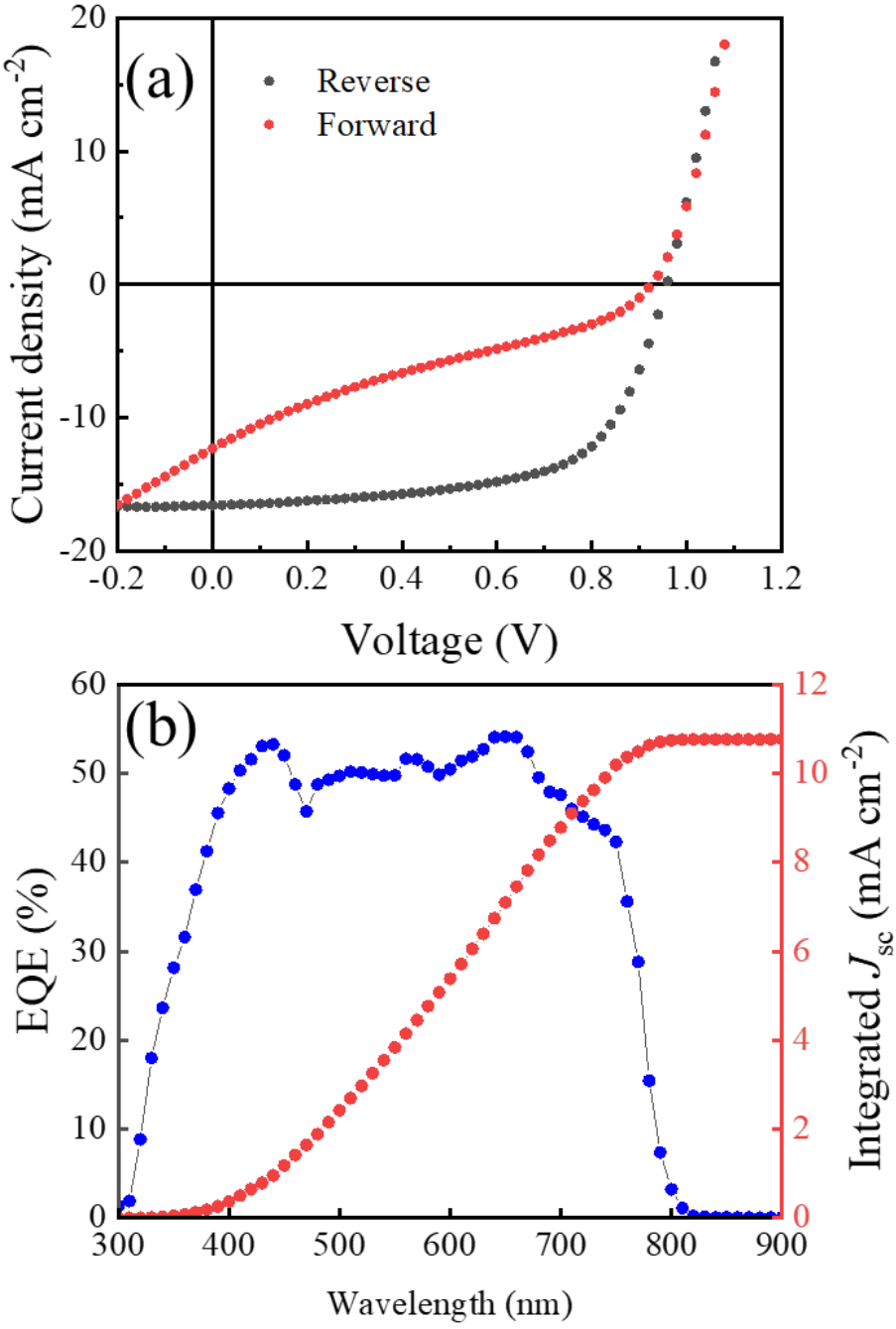

Figure 4.9: (a) *J-V* curve and (b) EQE spectrum (with integrated J_{sc}) of champion device

Table 4.2: Solar cell performance parameters of champion device

Scan Direction	J_{sc} (mA cm^{-2})	V_{oc} (V)	FF (%)	PCE (%)	Integrated J_{sc} (mA cm^{-2})
Reverse	16.6	0.96	62.9	10.0	10.8
Forward	12.3	0.92	25.4	2.9	

The mechanical stability of SDC-FPSC devices incorporating ETL3 is assessed by subjecting them to bending cycles, followed by measurements of PV performance parameters. The devices are evaluated immediately after bending cycles, maintaining a bending radius curvature of approximately 1 cm, and undergo 50 bending cycles. Figure 4.10 illustrates the trends in PV parameters for a device with ETL3 under bending conditions. Following the initial 10 bending cycles, the device experiences a 45% decrease in J_{sc} and a 37% decrease in FF. These rapid declines in J_{sc} and FF values may primarily stem from the structural deterioration of the device, particularly the cracking of the device's ITO layer.[127–131] This significantly elevates the device's R_s. Between the next 10th and 50th bending cycles, the values of the device FF drop gradually and consistently, while the decline in J_{sc} occurs at a slightly faster pace. These deteriorations could result from further and more complex structural integrity issues, such as micro delamination of device functional layers.

Regarding device V_{oc}, a nearly linear decay trend is observed with increased bending cycles. This suggests the formation of numerous defects, such as microcracks, in the perovskite layer, leading to increased charge carrier recombination.[132–135] These trends in J_{sc}, FF, and V_{oc} behavior with increasing bending cycles contribute to a rapid decay in device PCE after the initial 10 bending cycles (decreasing from 7% to 2.5%) and a somewhat steady decay between the 10th-50th bending cycles. Following the 50th bending cycle, the device's PCE drops to approximately 0.84%, marking an eightfold decrease from the initial PCE value (7%). Overall, the device

demonstrates relatively acceptable mechanical stability, which could be enhanced by transitioning to more durable TCO layers.[135]

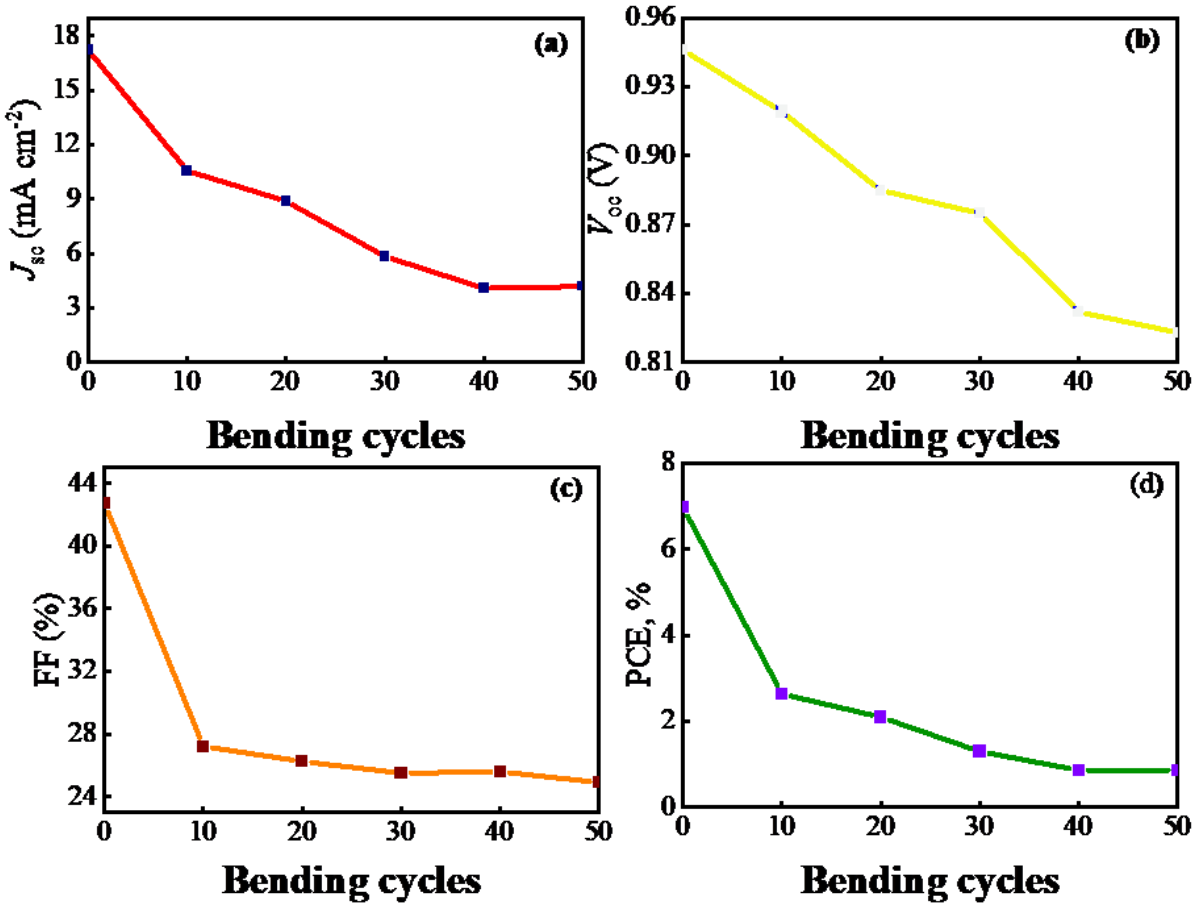

Figure 4.10: Changes in device (a) J_{sc}, (b) V_{oc}, (c) FF, and (d) PCE upon bending cycles

4.3. Conclusion of the Chapter

In conclusion, the chapter demonstrates a facile synthesis of SnO_2 QDs-based ETL ink. The formulated ink has been passed through different material and device characterization protocols for optimization. Firstly, the average particle size is around 2.4 nm according to TEM micrographs. This is in good agreement with the XRD analysis, confirming the crystallinity and size of the SnO_2 QDs. Later, these SnO_2 QDs were dispersed in an aqueous media to obtain inks with varying concentrations, i.e. 0, 1.0, 1.5, 2.0, 2.5, and 3.0 wt.% in DI water. Fabrication of the dives is conducted on the flexible PET/ITO substrates using a scalable SDC technique. The devices fabricated using 2.0 wt.% of SnO_2 QDs-based ETL outperform the others. These devices showed

an average PCE of around 7.23 % for the reverse scan. The champion device showed a PCE of around 10 % with the 2 wt.% concentration SnO_2 QDs-based ink. It showed better solar cell device performance parameters and enhanced EQE than the other concentrations. In the end, the mechanical stability of the device is tested with a bending test analysis. The fast degradation in the PV device performance parameters is observed due to the cracking of the ITO layer upon bending. Later, the device continuously performed several bending cycles, showing its compatibility with the flexible substrates. The findings reported in this chapter might be helpful in the synthesis and development of a low-temperature processable and flexible substrate-friendly SnO_2 QDs-based ETL ink.

Chapter#5

Switching from SnO_2 Nanoparticles to SnO_2 Quantum Dots

5.1. Materials

All the materials used in this analysis are similar to that reported in Chapter #4, with the addition of SnO_2 NP colloid dispersion (15 wt % colloidal dispersion in H_2O) and (6,6)-phenyl C71 butyric acid methyl ester ($PC_{71}BM$) purchased from Alfa Aesar and Lumtec, respectively. While Kurt. J. supplied molybdenum oxide (MoO_x), Al, and Ag pellets for fabrication of back electrodes of devices.

5.1.1. Ink Preparations

The entire ink synthesis process is depicted in the flowchart in Figure 5.1. All the inks, except the SnO_2 NP-based ETL ink, are made using the same methods described in Chapter 4. The SnO_2 NP ink is prepared by dissolving a colloidal dispersion of SnO_2 NPs in DI water at a ratio of 1:6.5 to achieve a final ink concentration of 2 wt.%. The resulting solution is then ultrasonicated for 20 minutes to ensure thorough mixing. After sonication, the ink is filtered using a 0.45 μm PTFE syringe filter to remove any agglomerated particles.

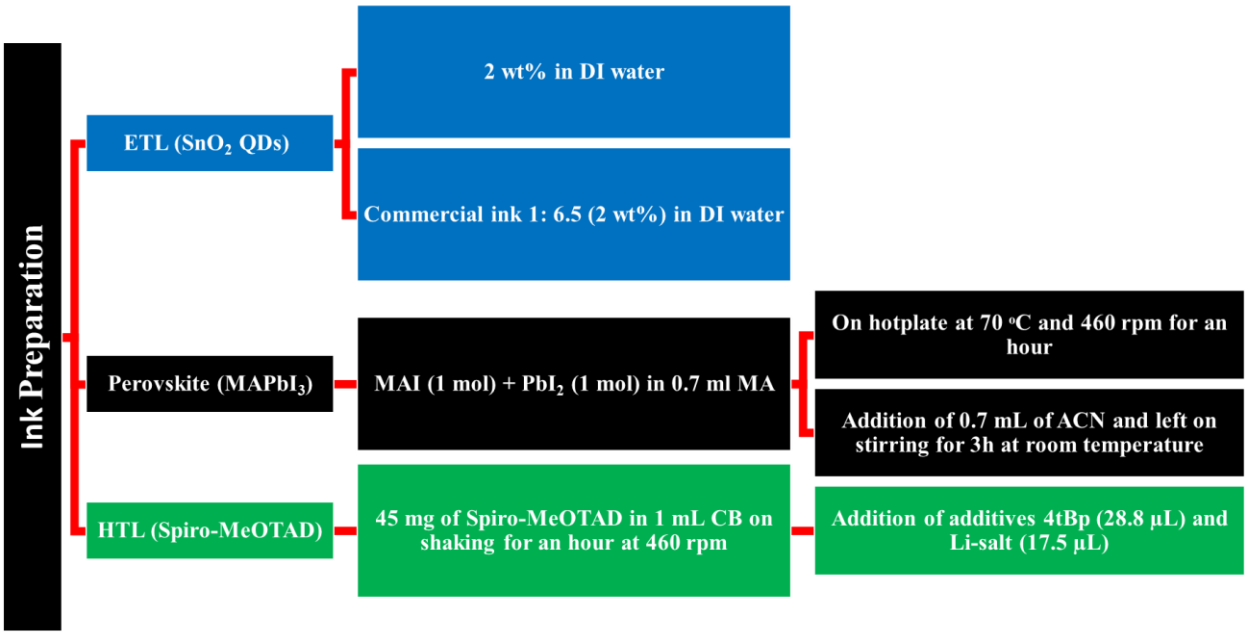

Figure 5.1: Schematic diagram showing preparation steps for ETL, perovskite, and HTL inks

5.1.2. Substrate Preparation

PET/ITO substrates are utilized in the manufacturing of SDC-FPSCs. The cleaning process involves immersing the substrates in an ultrasonic bath for ten minutes each in DI water with detergent, followed by clean DI water, acetone, and IPA. After this cleaning step, the substrates are treated with UV-ozone for 15 minutes and then dried using a compressed air stream.

5.1.3. Device Fabrication

Next, the functional layers are printed; the as-synthesized SnO_2 QDs-based and the commercial SnO_2 NPs-based inks are SDC on the PET/ITO substrates using a slot-die head attached to a syringe pump. After the deposition of the ETLs, these substrates are annealed at 140 °C for 30 min inside an oven. Afterwards, the substrates are allowed to cool down. Once cooled and reached room temperature, substrates are fixed on the chuck of the slot-die coater for the slot-die coating of the perovskite ink onto the SDC-ETL. After the perovskite deposition, the substrates are subjected to annealing at 100 °C for 10 min in an oven. Next, the HTL ink is coated on the $MAPbI_3$ layer with a clean slot-die head. Right after the final (HTL) layer deposition, the substrates are left

in an oxygen environment for 12 h. All functional layers are SDC in an ambient atmosphere at a chuck temperature of 25 °C and an RH of ~40-60%.

After 12 h, the back electrode is deposited using a Nexdep PVD thermal evaporator (Angstrom) and a shadow mask. The back electrodes were the MoO_x/Al contacts with a 10nm/100nm thickness. A schematic diagram of the device structure and energy level diagram for the SDC-FPSCs are shown in Figure 5.2.

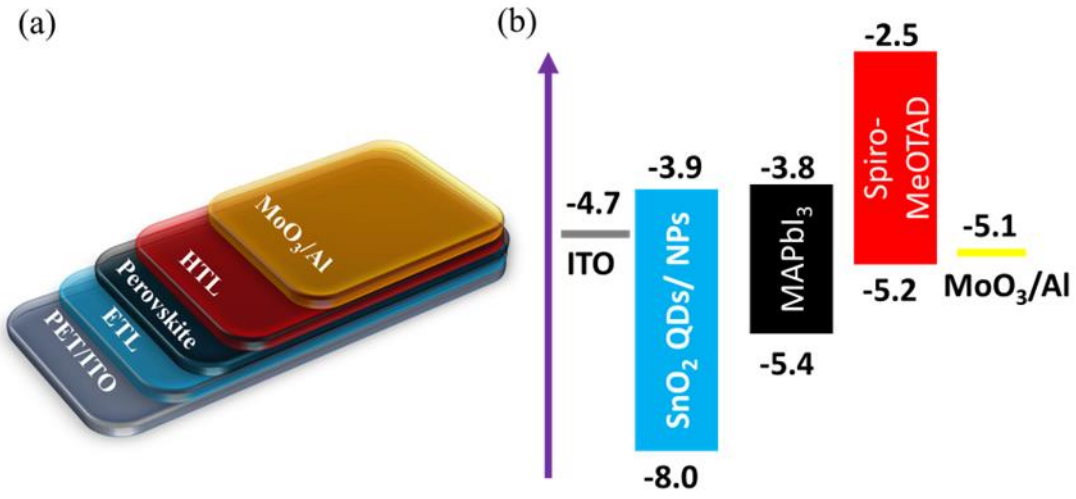

Figure 5.2: Schematic diagrams showing (a) structure and (b) energy band alignment in FPSCs

5.2. Results

TEM micrographs are obtained for the samples containing SnO_2 QDs (Fig. 5.3a and 5.3b) and SnO_2 NPs (Fig. 5.3d and 5.3e). The SnO_2 QDs and SnO_2 NPs are crystalline and have fairly homogeneous particle distributions, as shown in Fig. 5.3c and 5.3f. According to Figure 5.3c, the mean particle size of SnO_2 QDs is approximately 2.5 nm, which is smaller than the Bohr exciton radius of SnO_2 (2.70 nm).[136] In comparison, SnO_2 NPs exhibit an average particle size of around 4.5 nm, as shown in Figure 5.3f. The measurement of the particle sizes is done by analyzing 11 particles of each ink using ImageJ software. The XRD graphs of the samples containing SnO_2 QDs and SnO_2 NPs, which can be found in Appendix Fig. A5.2, also demonstrate the crystalline nature of the particles.

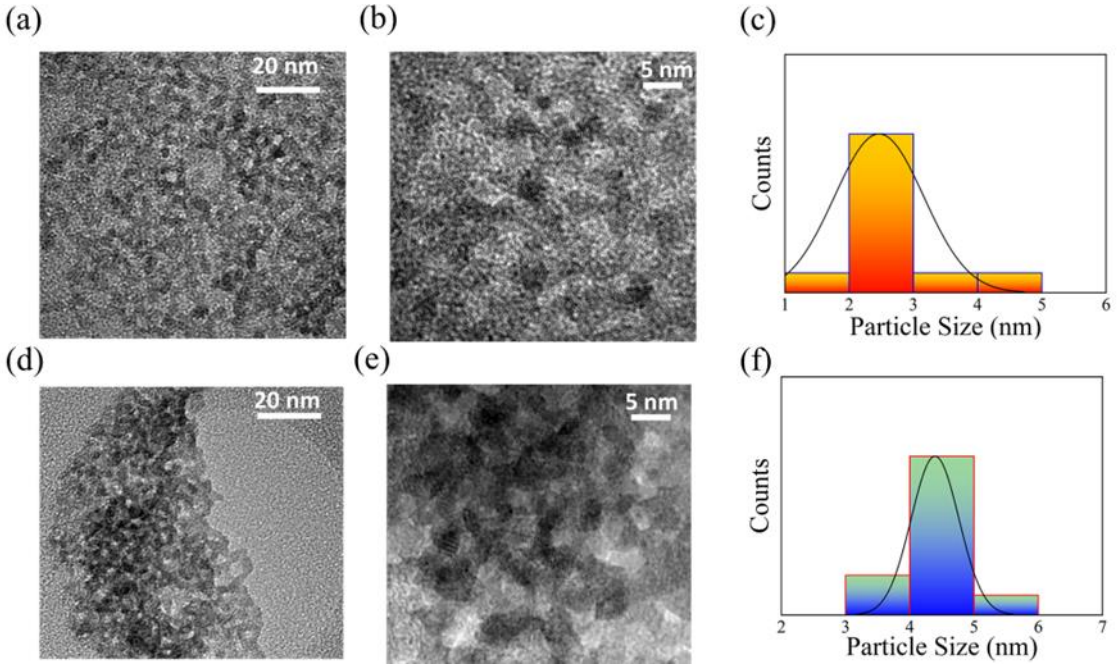

Figure 5.3: TEM micrographs of (a-b) SnO_2 QDs and (d-e) SnO_2 NPs at lower and higher magnifications, respectively. Particle size distribution curves of SnO_2 (c) QDs and (f) NPs

To develop SDC-FPSCs using SnO_2 QD and SnO_2 NP-based ETLs, clean PET/ITO substrates are SDC with the ETL inks. A top-view SEM examination is performed on the PET/ITO substrates coated with ETL to examine the surface coverage and homogeneity of the resulting SnO_2 NP- and SnO_2 QD-based ETLs. The SEM micrographs (see Fig. A5.3 in the Appendix) reveal that the PET/ITO substrates are rather uniformly covered by both types of ETLs since there are no visible pinholes in the ETLs. SnO_2 QD- and SnO_2 NP-based ETLs on PET/ITO substrates are thus freshly developed, and the $MAPbI_3$ layer is SDC on top of them. After the SDC-$MAPbI_3$ layer has formed, a Spiro-MeOTAD-based HTL is SDC on top. The device fabrication procedure is completed using a thermal evaporator to deposit MoOx/Al contacts. Figure A5.4 illustrates the SEM cross-section view micrographs of the acquired devices.

The resultant devices' performance is examined under ambient conditions, devoid of encapsulation. Figure 5.4 presents a comparative analysis of the resulting device's PV parameters. For both kinds of ETLs, a total of 45 devices are examined. This comparison is displayed for the

following device parameters: J_{sc}, V_{oc}, FF, PCE, R_s, and R_{Sh}. Table A5.2 shows the mean values for the PV properties (refer to Appendix).

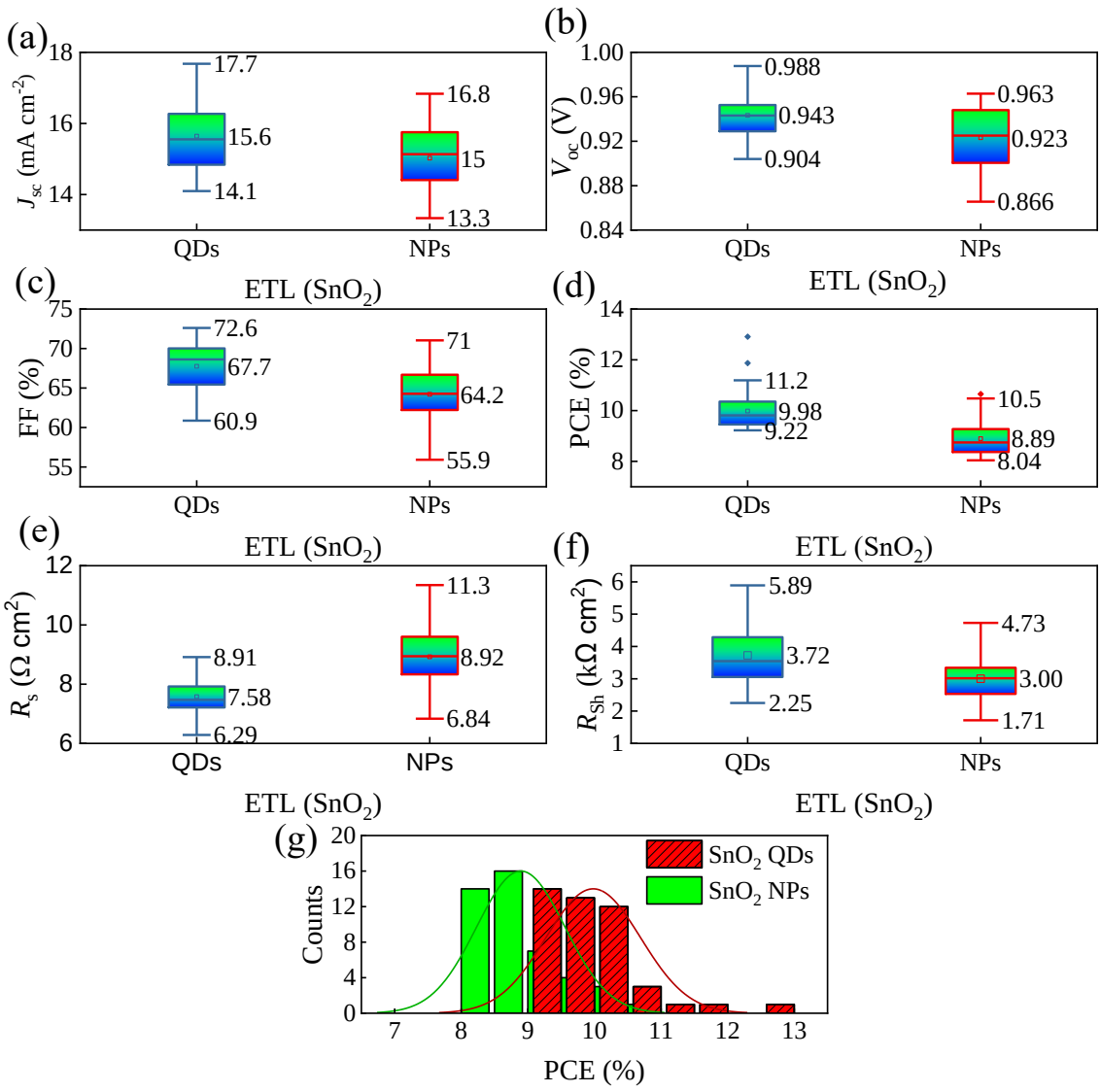

Figure 5.4: Comparison of statistical values for (a) J_{sc}, (b) V_{oc}, (c) FF, (d) PCE, (e) R_S, and (f) R_{Sh} in FPSCs with SnO_2 QD- and SnO_2 NP-based ETLs, (g) PCE distribution diagram for FPSCs with SnO_2 QD- and SnO_2 NP-based ETLs

The devices with SDC-SnO_2 QD-based ETLs had greater J_{sc} and V_{oc} values than those with SDC-SnO_2 NP-based ETLs, as shown in Fig. 5.4a and 5.4b. The average values of the devices J_{sc}, V_{oc}, and FF with SnO_2 QD-based ETLs are greater than those with SnO_2 NP-based ETLs. As a

result, compared to devices with SnO_2 NP-based ETLs, the average PCE of devices with SnO_2 QD-based ETLs is about 11% higher. SnO_2 QD-based ETLs offer greater R_{Sh} and lower R_s in devices than SnO_2 NP-based ETLs, as shown in Figures 5.4e and 5.4f. This could be because SnO_2 QD-based ETLs are more compact and pinhole-free than their SnO_2 NP-based counterpart. The PCE values for most SnO_2 QD-based ETL devices range from 9 to 10.5%, whereas PCE values for SnO_2 NP-based ETL devices range from 8 to 9% (Fig. 5.4g).

The *J-V* curves of the top-performing devices with SnO_2 NP- and QD-based ETLs are presented in Fig. 5.5a. Table 5.1 displays the devices' solar cell performance parameters. Using SnO_2 QD-based ETL, the PCE of the best-performing device reached a value of around 12.91%. This is approximately 18% higher than the maximum PCE (10.6%) recorded in devices using SnO_2 NP-based ETL. Additionally, by comparing the recorded EQE spectra of these devices, the spectral responses of these devices are also assessed (refer to Fig. 5.5b). The devices' EQE spectra are well above 50% of the visible spectrum with spectral characteristics of $MAPbI_3$-based devices.[137,138] Comparing the device with SnO_2 NP-based ETL to the one with SnO_2 QD-based ETL, the former exhibits lower EQE values over the measuring range. Here, the 600–750 nm wavelength range shows a notable boost in the SnO_2 QDs-based device's EQE values, up to about 15% higher than the former device's EQE values for the same wavelengths. For devices with SnO_2 QD- and SnO_2 NP-based ETLs (See Table 5.1), the EQE spectra yield the integrated J_{sc} values of 15 and 13.5 mA cm^{-2}, respectively. The values of J_{sc} derived from the *J-V* measurements are generally consistent with these (see Fig. 5.5a and Table 5.1).

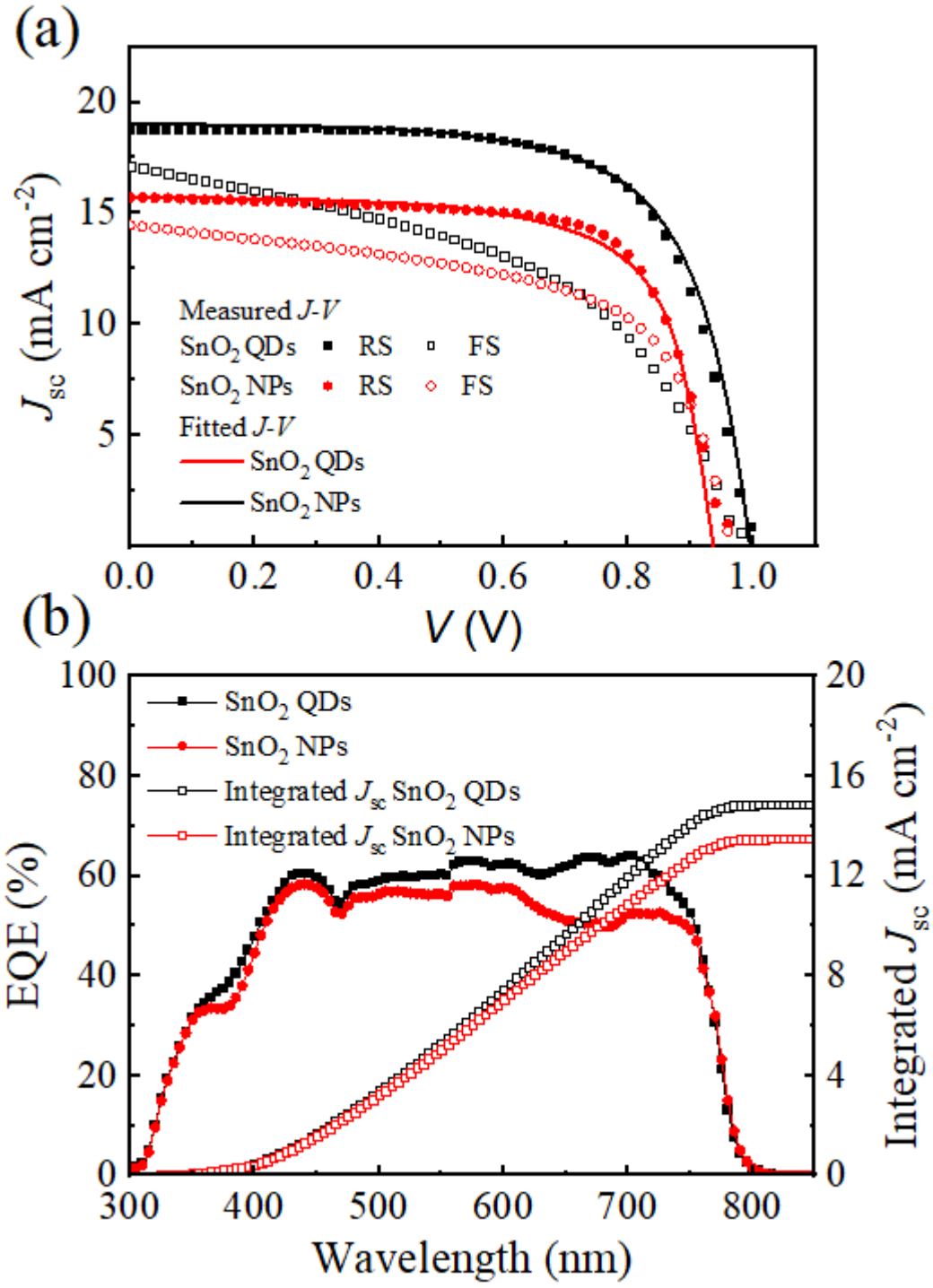

Figure 5.5: Comparison of (a) *J-V* curves and (b) EQE spectra (with integrated J_{sc}) of champion FPSCs with SnO_2 QD- and SnO_2 NP-based ETLs

Table 5.1: Photovoltaic device performance parameters of champion solar cells with SnO_2 QD-based and SnO_2 NP-based ETLs, tested under AM1.5G conditions

ETL	Scan Direction	J_{sc} (mA cm^{-2})	V_{oc} (V)	FF (%)	PCE (%)	R_s (Ω cm^2)	R_{sh} (kΩ cm^2)	Integrated J_{sc} (mA cm^{-2})
SnO_2 QDs	Rev.	18.8	1.00	69	12.9	3.9	1.0	
	Theor.	19.0	1.00	68	12.9	3.8	1.0	15.0
	For.	17.3	1.0	48	8.1	3.9	0.2	
SnO_2 NPs	Rev.	15.7	1.0	71	10.6	3.9	0.9	
	Theor.	15.7	0.9	69	10.3	4.0	0.9	13.5
	For.	14.5	0.9	59	8.2	4.7	0.3	

According to the results, devices using SnO_2 QD-based ETLs often outperform those using SnO_2 NP-based ETLs. The size variation of the SnO_2 particles is the primary distinction between these two types of ETLs. This might have an impact on the ETL/$MAPbI_3$ interface. Different SnO_2 particle sizes may change the optical characteristics of the employed ETLs, which can then impact the carrier extraction and recombination at the ETL/$MAPbI_3$ interface.[139–141] Nonetheless, the UV-Vis transmittance analyses conducted on SnO_2 QD- and SnO_2 NP-based ETLs on glass (refer to Fig. A5.5 Appendix) demonstrate that the optical transparency of these two kinds of ETLs is similar. This indicates that the same light will be transmitted to the perovskite layer when the devices are illuminated with the same light intensity. Thus, the size difference between SnO_2 QD and SnO_2 NP does not cause a performance difference between the devices. Under the same light illumination, the carrier production in the perovskite layer is expected to be consistent if the devices with these two different types of ETLs have the same perovskite layer thickness, as is the case in the fabricated devices. Therefore, variations in carrier generation are unlikely to account for the performance differences between devices using SnO_2 QD-based and SnO_2 NP-based ETLs. Instead, these disparities may be attributed to the carrier extraction and recombination processes occurring at the ETL/$MAPbI_3$ interface.

The extraction coefficient (c_{ex}), representing the efficiency of charge carrier extraction, can be estimated using the following equation:

$$c_{ex}(V) \approx \frac{J_{sc}}{J_{gen}}, \quad (5.1)$$

where J_{gen} is the current density of photo-generated charge carriers.[142] The current of photo-generated carriers in solar cells consists of two components: the current density due to holes (J_p) and the current density due to electrons (J_n). The total generated current density, J_{gen}, can be described by the following equations:[141,143]

$$J_{gen} = J_p + J_n \quad (5.2)$$

where,

$$J_p = qn\mu_p E_v + \mu_p k_B T \nabla p \quad (5.3)$$

$$J_n = qn\mu_n E_c + \mu_n k_B T \nabla n \quad (5.4)$$

Here, $E_v = -\nabla(V + \chi_0 + E_{g,0})$ and $E_c = -\nabla(V + \chi_0)$ are the conduction and valance band energies, $E_{g,0}$ is the band gap, χ_0 is the electron affinity, μ_n is the mobility of electrons and μ_p is the mobility of holes. Since the HTL is identical in the SDC devices with SnO_2 QD-based and SnO_2 NP-based ETLs, the hole current density (J_p) can be assumed to be the same. Therefore, in this case, the difference in charge carrier extraction is primarily determined by the electron current density (J_n).

Steady-state PL (SS-PL) measurements are carried out for SDC-$MAPbI_3$ with the glass as the substrate, as well as the SnO_2 QD ETL/$MAPbI_3$ and SnO_2 NP ETL/ $MAPbI_3$ films on glass, to get a better insight on charge transfer between the $MAPbI_3$ layer and SnO_2 QD- and SnO_2 NP-based ETLs. The clean $MAPbI_3$ film exhibits a PL peak at around 775 nm, which is characteristic

peak for $MAPbI_3$, as seen in Fig. 5.6. SnO_2 ETLs partly quench the PL emission of the $MAPbI_3$ layer, as evidenced by the PL peak of the SnO_2 QD-based ETL/$MAPbI_3$ film and the SnO_2 NP-based ETL/$MAPbI_3$ film being much lower than the PL peak of the neat $MAPbI_3$ film. This suggests that photo-generated charges are transferred to SnO_2 ETLs from the $MAPbI_3$ layer. Additionally, Fig. 5.6 shows that compared to the SnO_2 QD-based ETL/$MAPbI_3$ film, the PL peak of the SnO_2 NP-based ETL/$MAPbI_3$ film is significantly larger. This implies that charge extraction is more efficient in SnO_2 QD-based ETLs than in SnO_2 NP-based ETLs. These findings unambiguously indicate that SnO_2 QD- and SnO_2 NP-based ETLs have different ETL/perovskite interface characteristics. Therefore, examining the physical characteristics of this interface may provide some understanding of the performance disparity between devices that use SnO_2 NP- and SnO_2 QD-based ETLs.

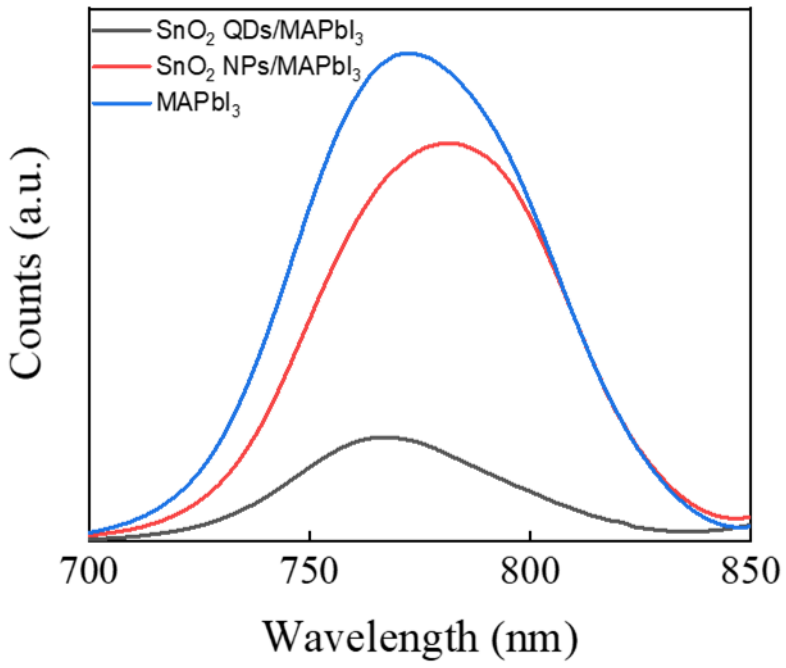

Figure 5.6: Steady-state PL spectra of pristine $MAPbI_3$, SnO_2 QD-based ETL/$MAPbI_3$, and SnO_2 NP-based ETL/$MAPbI_3$ films on glass

Measurements of space-charge-limited current (SCLC) using electron—or hole-only devices help determine the trap state density and the mobility of charge carriers in semiconductors.[144–146] Therefore, SDC electron-only devices using SnO_2 QD- and SnO_2 NP-based ETLs can assist in investigating the characteristics of the ETL/$MAPbI_3$ interface in devices and offer some perspectives into how various ETLs impact these parameters in the $MAPbI_3$ layer. In light of this, SnO_2 QD- and SnO_2 NP-based ETLs are used to print electron-only devices, and the *J-V* characteristics of the resulting devices are examined. The architecture of the constructed electron-only devices is shown as an inset graph in Fig. 5.7, which also displays the *J-V* curve characteristics of the devices. The linear relation indicates the device's ohmic response at low bias. There was a distinct kink point at which the current rises linearly with the voltage. When the voltage increases to the area above the kink-point, the current rises more quickly, indicating that injected carriers are filling the trap states.[147] Three zones may be seen in the presented electron-only devices' *J-V* curves. The first area has a slope of 1 and is at low voltages. The second has a slope of two and is at intermediate voltages. This intermediate region is referred to as the trap-filling regime.[145] Lastly, at high voltages, the third area – known as the SCLC region with a slope greater than two – appears.[144] Using the Mott-Gurney equation, we can estimate the electron mobility from the SCLC region:

$$\mu_n = \frac{8 J_D A^3}{9 \varepsilon \varepsilon_0 V^2}, \tag{5.5}$$

where J_D, V, and ε (=28.8) are the current density, the applied voltage, and the relative dielectric constant of $MAPbI_3$ perovskite, respectively.[146,148] While ε_0 and A (=550 nm) are the vacuum permittivity and the thickness of the $MAPbI_3$ film, respectively.

The estimated μ_n values from the electron-only devices in the $MAPbI_3$ layer, using SnO_2 QD-based and SnO_2 NP-based ETLs, are approximately 6.40×10^{-4} and 6.10×10^{-4} $cm^2\ V^{-1}s^{-1}$, respectively. Although the μ_n value for the device with the SnO_2 QD-based ETL is slightly higher than that for the SnO_2 NP-based ETL, this minor difference is not significant enough to account for the substantial variation observed in the J_{sc} values of the SDC-FPSCs (refer to Fig. 5.4a and

Fig. 5.5a). Therefore, the variation in the carrier extraction coefficient between devices with SnO_2 QD-based and SnO_2 NP-based ETLs is likely related to differences in charge carrier concentration, which are influenced by the recombination processes occurring within the devices.[141]

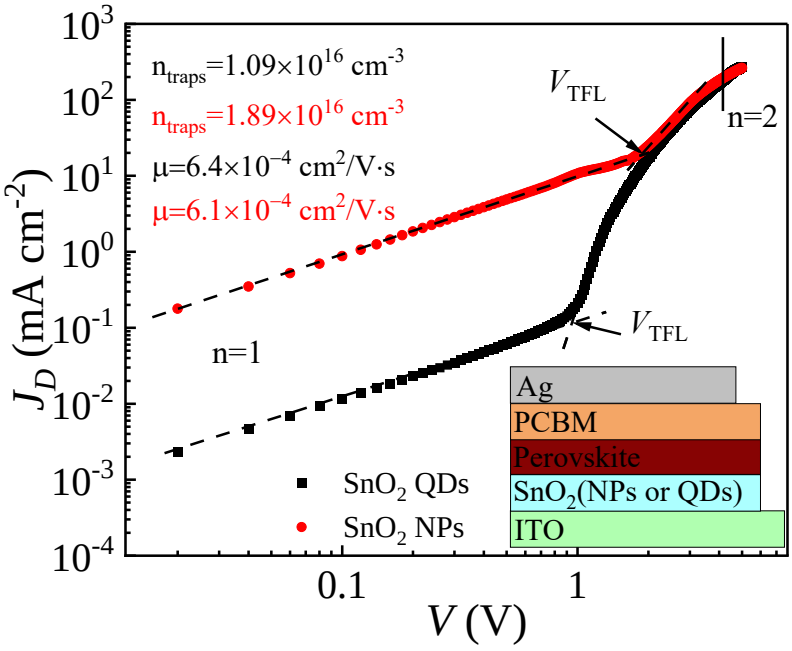

Figure 5.7: *J-V* curves of electron-only devices with SnO_2 QD- and SnO_2 NP-based ETLs

Three primary processes comprise carrier recombination in PSCs: Shockley-Read-Hall (SRH), radiative, and Auger recombination. The material's characteristic of radiative recombination in the perovskite layer shouldn't alter based on the carrier-selective layers. Therefore, the SRH and surface recombination processes are mostly responsible for the variation in carrier recombination between the devices with SnO_2 QD- and SnO_2 NP-based ETLs. The following relation is used to determine the density of trap states to figure out the recombination processes in the devices:

$$n_{trap} = \frac{2\varepsilon\varepsilon_0 V_{TFL}}{(qA^2)} \qquad (5.6)$$

where q and V_{TFL} are the elementary charge and the trap-filled-limit voltage respectively, estimated from the SCLC measurements with electron-only devices.[149,150] The estimated value of n_{trap} in the perovskite layer of the device with SnO_2 QD-based ETL is 1.10×10^{16} cm^3, whereas it is 1.89×10^{16} cm^3 in the device with SnO_2 NP-based ETL. These results show that using SnO_2 NPs to form ETLs results in more trap states in the perovskite layer.

The recombination mechanisms are better understood by examining the dependency of V_{oc} and J_{sc} on light intensity in the resultant SDC-FPSCs.[151–153] To do this, neutral density filters (see Fig. A5.6 in the Appendix) are used to measure the *J-V* curves of the top-performing FPSCs with SnO_2 QD- and SnO_2 NP-based ETLs (see Fig. 5.8a) under various light intensities. The inset graph in Figure 5.8 shows that J_{sc}'s dependency on light intensity is linear for both devices. This suggests that the devices' recombination losses under short-circuit conditions are minimal.[154]

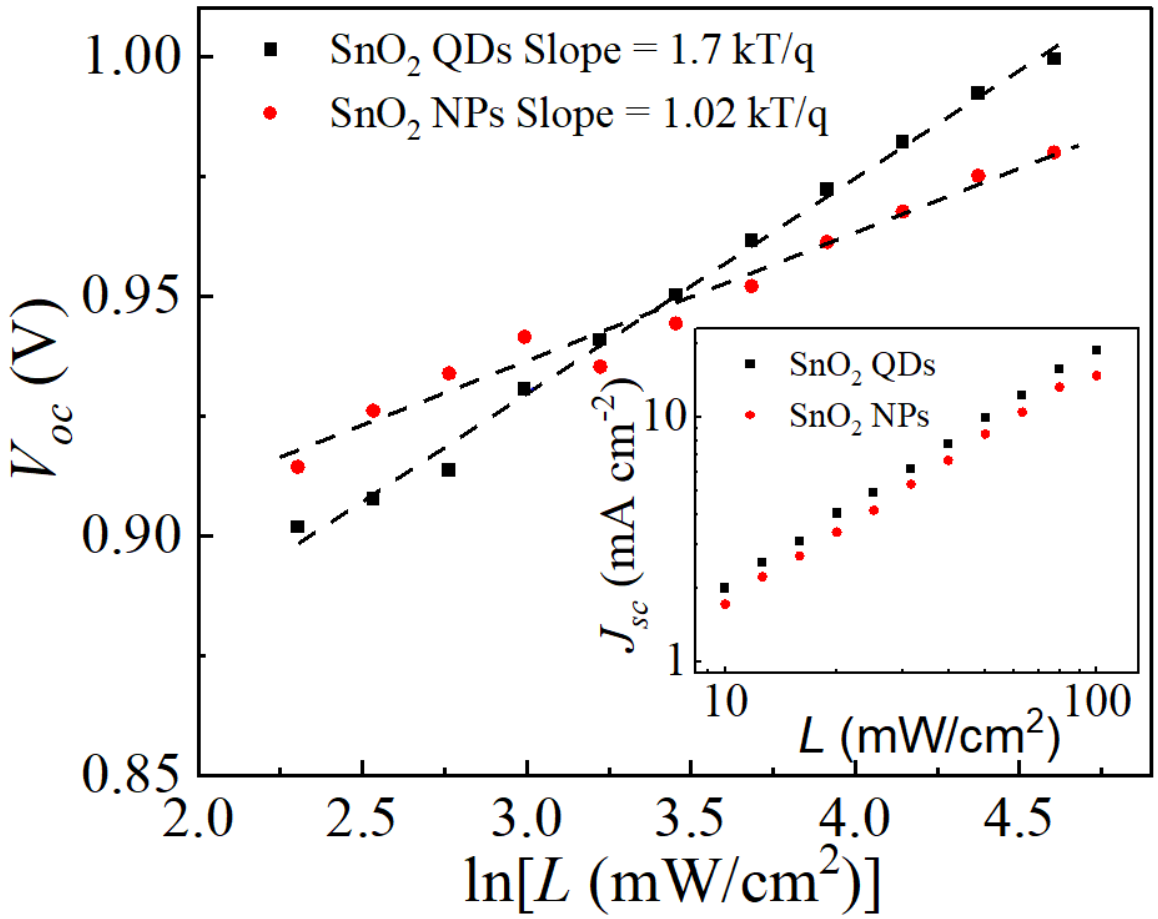

Figure 5.8: The dependences of V_{oc} and J_{sc} on varying light intensities for best-performing

The V_{oc} dependence on light intensity can be understood using the following equation:[143,155,156]

$$V_{oc} = \frac{n_{idl} k_B T ln(L)}{q}, \quad (5.7)$$

n_{idl} is the light ideality factor, k_B is Boltzmann's constant, T is the absolute temperature, and L is the light intensity. Estimating the n_{idl} from the slope of the V_{oc} dependence on $ln(L)$ is possible. The estimated n_{idl} value from Fig. 5.8 for the device with SnO_2 QD-based ETL is around 1.7. This suggests that SRH recombination is the device's primary source of recombination.[154,155,157] The defects present in the perovskite active layer are often responsible for the dominant SRH recombination in FPSCs.[158,159] The expected value of n_{idl} for the device with SnO_2 NP-based ETL is 1.02. This is significantly lower than the n_{idl} value in the device using SnO_2 QD-based ETL. Surface recombination processes are frequently attributed to the decrease in n_{idl}.[160,161] This suggests that in addition to surface recombination, SRH recombination in the devices with SnO_2 NP-based ETLs causes a significant loss of photo-generated charge carriers. Additional evidence for this comes from the devices' OCVD measurements, which indicate that the device with SnO_2 QD-based ETLs has a higher electron lifetime (τ) value (around MPP and lower voltages) than the device with SnO_2 NP-based ETLs (see Fig. A5.7 in Appendix).

Numerical simulation approaches employing standard drift-diffusion models afford to reproduce *J-V* curves of PSCs. Thus, we employed this approach to reproduce the *J-V* curves (reverse scans) of the top-performing devices using SnO_2 QD- and SnO_2 NP-based ETLs to better comprehend the experimentally obtained results. This is accomplished by using the experimentally determined $MAPbI_3$ layer electronic parameters, including the charge carrier mobility (approximated from the SCLC measurements, see Fig. 5.7) and the τ (approximated from the OCVD measurements, see Fig. A5.7 in Appendix), along with the values from the literature for remaining functional layers of the device (see Table A5.3 in Appendix). The theoretical *J-V* curves (see Fig. 5.5a and Table 5.1) that closely resemble the experimental ones are obtained via these

techniques. The results of the simulation studies indicate that the device using SnO_2 NP-based ETL has a higher surface recombination speed value than the device using SnO_2 QD-based ETL. This suggests that in the device with SnO_2 NP-based ETL, charge carrier recombination at the ETL/$MAPbI_3$ interface is also greater, possibly because of a higher concentration of surface defects. This is in line with the experimental findings described above.

Lower levels of oxygen vacancies in SnO_2 QDs relative to SnO_2 NPs may be associated with greater charge extraction at the SnO_2 QD-based ETL/$MAPbI_3$ interface in devices. Decreased oxygen vacancies also implied better device performance and a decrease in the concentration of trap states in SnO_2 ETLs.[63,162,163] Thus, SnO_2 QD- and SnO_2 NP-based ETLs on bare glass are subjected to XPS investigation to gain a better insight. Figure 5.9 displays the XPS spectra that were recorded for the samples. The spectra of the samples are provided in full in Fig. 5.9a and b, while the enlarged pictures of the spectral peaks linked to oxygen (O) and tin (Sn) are displayed in Fig. 5.9c and d. Potassium (K) impurities are also visible in the spectra of samples, as seen in Fig. 5.9a and b. The KOH addition found in ETL inks provides potassium, which aids in stabilizing the colloidal solutions of SnO_2 QDs and SnO_2 NPs [35]. Sn, O, and K elemental ratios in SnO_2 QD- and SnO_2 NP-based ETLs derived from Sn*3d*, O*1s*, and K*2p* XPS peaks are displayed in Table 5.2.

For SnO_2 QD- and SnO_2 NP-based ETLs, the ratio of O*1s* to Sn3*d* yields values of 3.72 and 3.48, respectively, suggesting reduced oxygen vacancies in the former. Furthermore, compared to SnO_2 NP-based ETLs, the elemental ratio of K in SnO_2 QD-based ETLs appears to be more than twice as high. It is important to note that K ions can be an effective passivating agent for surface imperfections in the perovskite layer [164–166]. Therefore, it is plausible to propose that the enhanced functionality of SDC-FPSCs using SnO_2 QD-based ETLs in contrast to their SnO_2 NP-based counterpart may result from a reduced oxygen vacancy concentration in the former. Furthermore, an increased concentration of K ions on the surface of SnO_2 QD-based ETLs aids in improving surface defect passivation of the $MAPbI_3$ layer at the interface between the ETL and

the perovskite. Thus, surface recombination is hampered, and the density of trap states is decreased.

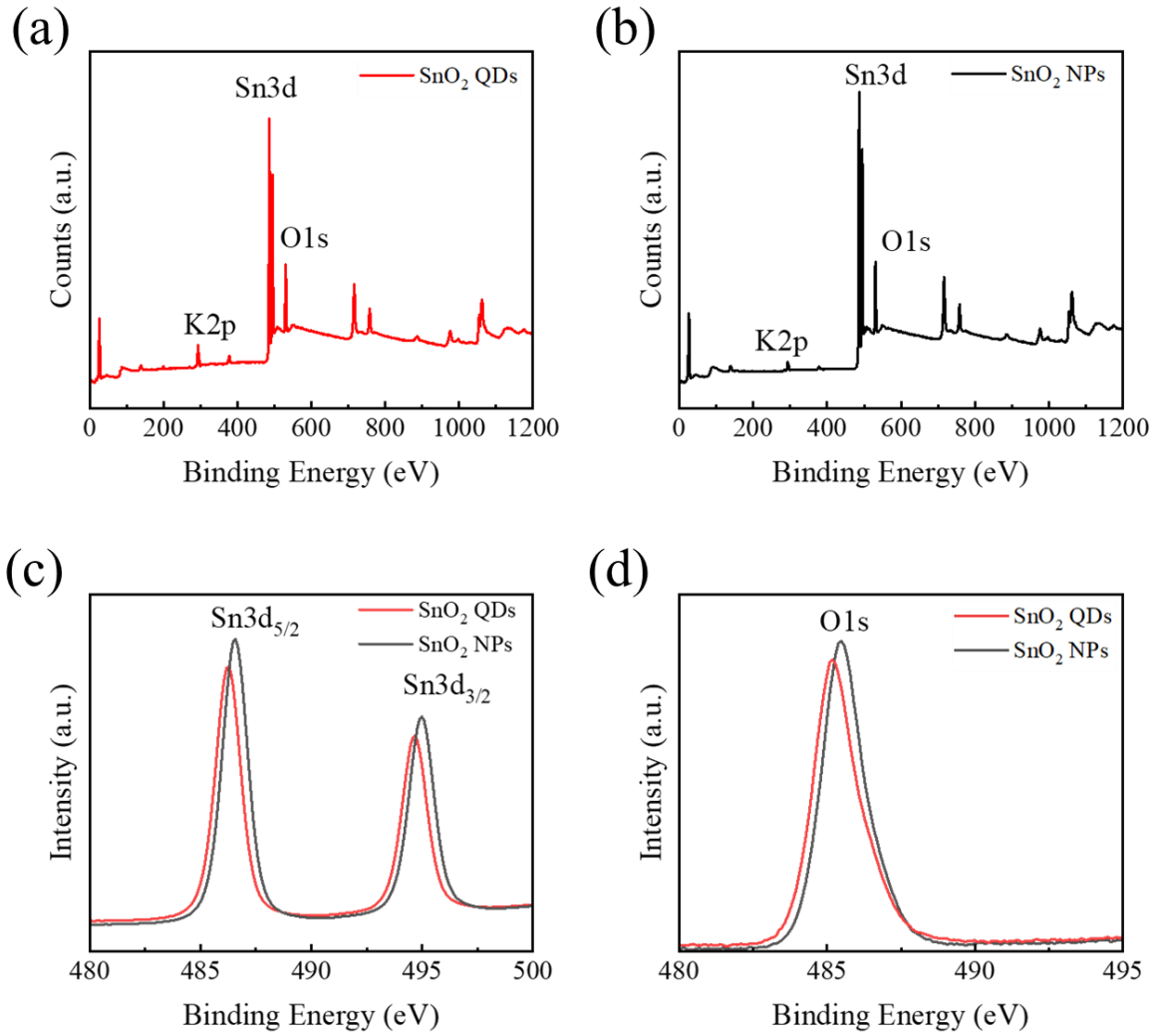

Figure 5.9: XPS spectra of (a) SnO_2 QD- and (b) SnO_2 NP-based ETLs. XPS spectra of SnO_2 QD- and SnO_2 NP-based ETLs for (c) Sn and (d) O peaks, respectively

Table 5.2: Atomic ratios of Sn, O, and K in SnO_2 QD- and SnO_2 NP-based ETLs

Element	**Atomic Percentage**	
	SnO_2 QDs	**SnO_2 NPs**
Sn3d	18.7	21.3
O1s	69.7	74.2
Sn3d/O1s	3.7	3.5

K2p	11.6	4.5

Lastly, a bending test is used to examine the mechanical stability of the devices using SnO_2 QD- and SnO_2 NP-based ETLs. After applying bending cycles, the devices' solar cell properties are evaluated. Here, devices were bent 10 times in succession to a curvature with a radius of one centimeter during a bending cycle. Figure 5.10 displays the behaviour of the devices' J_{sc}, FF, V_{oc}, and PCE values upon varying bending cycles. Similar patterns can be seen in the J_{sc} values in both devices, which decrease by around 70% following the first bending cycle and vanish completely following the second (see Fig. 5.10a). The V_{oc} of the SnO_2 QD-based ETL device exhibits a steady and linear degradation pattern as the number of applied bending cycles increases. The device's V_{oc} value decreases by around 5% following the final bending cycle.

In contrast, in devices with SnO_2 NP-based ETL, as seen in Figure 5.10b, the V_{oc} value decreases by approximately 5% following the first bending cycle and subsequently by approximately 15% following the second bending cycle. After that, the device's V_{oc} value essentially stays the same. Regarding the FF values, after the first bending cycle, they decrease in both devices by around 35–40% of their initial value before becoming constant (refer to Fig. 5.10c). The variations in the device PCE are determined by these patterns in the behaviour of J_{sc}, V_{oc}, and FF *vs.* bending cycles. Generally, the devices with ETLs based on SnO_2 QD and SnO_2 NP exhibit comparable patterns in their PCE variation when bending cycles are performed (refer to Fig. 5.10d). After the first bending cycle, the devices' PCE values decrease by around 75% of their starting values, and after the second bending cycle, they practically disappear completely. The ITO layer's deterioration (cracking), which causes a considerable rise in the R_s values of the devices and has a major impact on device current and FF, is primarily responsible for the observed degradation of the PV parameters of the devices during the bending test.[127,130,131] This can be lessened or enhanced by utilizing other interlayers that can increase the mechanical stability of the

TCO layers, or it can be improved by using TCO alternatives that are more resilient and durable.[98,134,167,168]

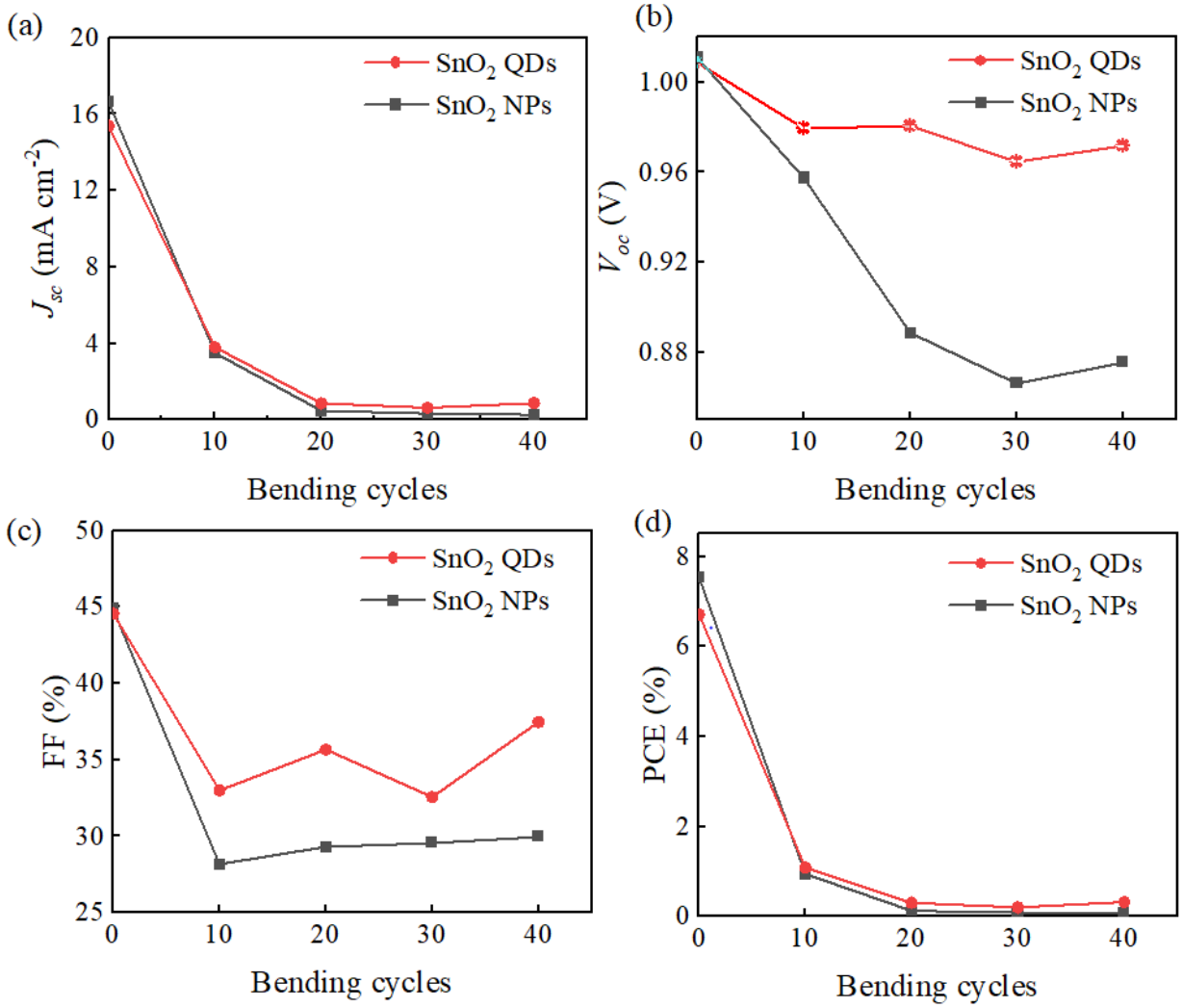

Figure 5.10: Changes in (a) J_{sc}, (b) V_{oc}, (c) FF, and (d) PCE of FPSCs with SnO_2 QD- and SnO_2 NP-based ETLs upon bending cycles

5.3. Conclusion of the Chapter

In conclusion, SnO_2 QD- and SnO_2 NP-based ETLs are used to fabricate SDC-FPSCs and the influence of these ETLs on the overall device PV performance. Devices using SnO_2 QD-based ETLs have been demonstrated to outperform those using SnO_2 NP-based ETLs on average. SnO_2

QD-based ETL yields a best-performing device with a PCE of 12.91%, whereas SnO_2 NP-based ETL produces a PCE of about 10.6%. When comparing SnO_2 QD-based ETLs to SnO_2 NP-based ETLs, the PL measurements using SnO_2 QD-based ETL/$MAPbI_3$ samples demonstrated a superior PL emission quenching of the perovskite layer. The perovskite layer of devices with SnO_2 QD-based ETLs possesses greater electron mobility and lesser trap states than that of devices with SnO_2 NP-based ETLs, according to tests conducted with electron-only devices.

Furthermore, devices with SnO_2 QD-based ETLs had smaller recombination losses than devices with SnO_2 NP-based ETLs, according to V_{oc} *vs.* light intensity and OCVD measurements done on the SDC-FPSCs. Numerical modelling experiments, which also showed reduced surface recombination in systems using SnO_2 QD-based ETLs, corroborate this. These results suggest that the enhanced performance of SnO_2 QD-based ETLs in the developed FPSCs may be caused by optimum conditions for the charge extraction process at the ETL/$MAPbI_3$ interface. This might have an underlying cause related to the superior material electronic characteristics of SnO_2 QD-based ETLs, which could result from the fact that SnO_2 QDs have higher potassium ion concentrations and fewer oxygen vacancies than SnO_2 NPs. The results of this study show that SnO_2 QDs can be a viable substitute for commercially available SnO_2 NPs in the preparation of ETLs of SDC-FPSCs. This can help fabricate effective devices at moderate temperatures and pave the way for developing more industrially friendly manufacturing techniques.

Chapter # 6

Conclusion and Outlook

This chapter outlines the novel contributions and critical outcomes of the current thesis and concludes with a summary. It also makes suggestions for prospective future research directions.

6.1. Key Findings

The aim of this thesis was threefold: (i) to develop SnO_2 QD-based ETL inks for application in flexible optoelectronics, particularly in halide perovskites, (ii) to optimize the ink formulation, and (iii) to compare the performance of these inks with that of commercially available and widely used SnO_2 NPs-based dispersion solutions. The synthesis and optimization processes of SnO_2 QDs-based ETL inks are detailed in Chapter 4. This chapter outlines the step-by-step methodology adopted to achieve the optimal ink formulation, highlighting the critical parameters and conditions that can influence ink's performance.

Chapter 5 focuses on a comparative analysis of PV device performance using newly developed SnO_2 QDs-based ETL inks and commercially available SnO_2 NPs-based dispersion solutions. This chapter presents a thorough comparison, highlighting the differences in efficiency and effectiveness between these two types of inks. Our key findings suggest that as-prepared SnO_2 QDs-based inks are suitable for fabricating highly effective ETLs in regular structured PSCs on PET substrates. These inks' formulation supports slot-die coating and processing, making them highly suitable for application in flexible optoelectronics.

The results presented in Chapter 5 indicate that SnO_2 QDs-based ETL inks significantly outperform the commercial SnO_2 NPs-based dispersion solutions, with an average PCE enhancement of approximately 11%. This improvement is attributed to the enhanced charge extraction capabilities of SnO_2 QDs and their ability to reduce trap states in the perovskite layer.

The QDs' superior electronic properties facilitate better charge transfer and minimize recombination losses, leading to higher overall device performance.

In summary, the development, optimization, and comparison of SnO_2 QDs-based ink as presented in this thesis offer significant advancements in the field of flexible optoelectronics. The findings underscore the potential of SnO_2 QDs-based ETL inks to replace traditional SnO_2 NP-based solutions, providing a pathway for more efficient and durable PSCs. This research not only demonstrates the practical benefits of using SnO_2 QDs in PSCs but also paves the way for future innovations in the development of high-performance, flexible optoelectronic devices.

References

(1) Nations, U. *Population*. United Nations. https://www.un.org/en/global-issues/population (accessed 2024-02-04).

(2) Letcher, T. M. Chapter 1 - The Root Causes of Global Warming and the New Normal. In *Living with Climate Change*; Letcher, T. M., Ed.; Elsevier, 2024; pp 3–20. https://doi.org/10.1016/B978-0-443-18515-1.00010-1.

(3) Roy, A. A Panel Data Study on the Effect of Climate Change on Life Expectancy. *PLOS Climate* **2024**, *3* (1), e0000339. https://doi.org/10.1371/journal.pclm.0000339.

(4) Pawan, M. Impact of Global Warming on Environment. **2014**, *3*.

(5) Ipcc. *Global Warming of 1.5°C: IPCC Special Report on Impacts of Global Warming of 1.5°C above Pre-Industrial Levels in Context of Strengthening Response to Climate Change, Sustainable Development, and Efforts to Eradicate Poverty*, 1st ed.; Cambridge University Press, 2022. https://doi.org/10.1017/9781009157940.

(6) *What is the Kyoto Protocol? | UNFCCC*. https://unfccc.int/kyoto_protocol (accessed 2024-02-18).

(7) Global Energy Transformation: A Roadmap to 2050.

(8) *Energy-related CO2 emissions worldwide 1975-2022*. Statista. https://www.statista.com/statistics/526002/energy-related-carbon-dioxide-emissions-worldwide/ (accessed 2024-02-07).

(9) Majeed, Y.; Khan, M. U.; Waseem, M.; Zahid, U.; Mahmood, F.; Majeed, F.; Sultan, M.; Raza, A. Renewable Energy as an Alternative Source for Energy Management in Agriculture. *Energy Reports* **2023**, *10*, 344–359. https://doi.org/10.1016/j.egyr.2023.06.032.

(10) *Energies | Free Full-Text | Renewable and Sustainable Energy Transitions for Countries with Different Climates and Renewable Energy Sources Potentials*. https://www.mdpi.com/1996-1073/11/12/3523 (accessed 2024-02-04).

(11) Lund, H. Renewable Energy Strategies for Sustainable Development. *Energy* **2007**, *32* (6), 912–919. https://doi.org/10.1016/j.energy.2006.10.017.

(12) Hong, S.; Bradshaw, C. J. A.; Brook, B. W. Global Zero-Carbon Energy Pathways Using Viable Mixes of Nuclear and Renewables. *Applied Energy* **2015**, *143*, 451–459. https://doi.org/10.1016/j.apenergy.2015.01.006.

(13) Guangul, F. M.; Chala, G. T. Solar Energy as Renewable Energy Source: SWOT Analysis. In *2019 4th MEC International Conference on Big Data and Smart City (ICBDSC)*; IEEE: Muscat, Oman, 2019; pp 1–5. https://doi.org/10.1109/ICBDSC.2019.8645580.

(14) Maradin, D. ADVANTAGES AND DISADVANTAGES OF RENEWABLE ENERGY SOURCES UTILIZATION. *IJEEP* **2021**, *11* (3), 176–183. https://doi.org/10.32479/ijeep.11027.

(15) Hayat, M. B.; Ali, D.; Monyake, K. C.; Alagha, L.; Ahmed, N. Solar Energy—A Look into Power Generation, Challenges, and a Solar-Powered Future. *International Journal of Energy Research* **2019**, *43* (3), 1049–1067. https://doi.org/10.1002/er.4252.

(16) Crabtree, G. W.; Lewis, N. S. Solar Energy Conversion. *Physics Today* **2007**, *60* (3), 37–42. https://doi.org/10.1063/1.2718755.

(17) Ohwofosirai, A. A Study of the Optical Conductivity, Extinction Coefficient and Dielectric Function of CdO by Sucessive Ionic Layer Adsorption and Reaction (SILAR) Techniques. *ACSJ* **2014**, *4* (6), 736–744. https://doi.org/10.9734/ACSJ/2014/6958.

(18) Nozik, A. J. Photoelectrochemistry: Applications to Solar Energy Conversion. *Annu. Rev. Phys. Chem.* **1978**, *29* (1), 189–222. https://doi.org/10.1146/annurev.pc.29.100178.001201.

(19) Markvart, T.; CastaÑer, L. IIa-1 - Principles of Solar Cell Operation. In *Practical Handbook of Photovoltaics*; Markvart, T., Castañer, L., Eds.; Elsevier Science: Amsterdam, 2003; pp 71–93. https://doi.org/10.1016/B978-185617390-2/50005-2.

(20) Goetzberger, A.; Luther, J.; Willeke, G. Solar Cells: Past, Present, Future. *Solar Energy Materials and Solar Cells* **2002**, *74* (1), 1–11. https://doi.org/10.1016/S0927-0248(02)00042-9.
(21) Płaczek-Popko, E. Top PV Market Solar Cells 2016. *Opto-Electronics Review* **2017**, *25* (2), 55–64. https://doi.org/10.1016/j.opelre.2017.03.002.
(22) Lee, T. D.; Ebong, A. U. A Review of Thin Film Solar Cell Technologies and Challenges. *Renewable and Sustainable Energy Reviews* **2017**, *70*, 1286–1297. https://doi.org/10.1016/j.rser.2016.12.028.
(23) Fthenakis, V. Sustainability of Photovoltaics: The Case for Thin-Film Solar Cells. *Renewable and Sustainable Energy Reviews* **2009**, *13* (9), 2746–2750. https://doi.org/10.1016/j.rser.2009.05.001.
(24) Ananthakumar, S.; Kumar, J. R.; Babu, S. M. Third-Generation Solar Cells: Concept, Materials and Performance - An Overview. In *Emerging Nanostructured Materials for Energy and Environmental Science*; Rajendran, S., Naushad, Mu., Raju, K., Boukherroub, R., Eds.; Environmental Chemistry for a Sustainable World; Springer International Publishing: Cham, 2019; Vol. 23, pp 305–339. https://doi.org/10.1007/978-3-030-04474-9_7.
(25) *Best Research-Cell Efficiency Chart*. https://www.nrel.gov/pv/cell-efficiency.html (accessed 2021-10-18).
(26) Teply, C.; Tyler, B. A.; Berger, R. F. Tuning the Band Gaps of Oxide and Halide Perovskite Compounds via Biaxial Strain in All Directions. *J. Phys. Chem. C* **2021**, *125* (47), 25951–25958. https://doi.org/10.1021/acs.jpcc.1c07169.
(27) Song, Z.; Watthage, S. C.; Phillips, A. B.; Heben, M. J. Pathways toward High-Performance Perovskite Solar Cells: Review of Recent Advances in Organo-Metal Halide Perovskites for Photovoltaic Applications. *J. Photon. Energy* **2016**, *6* (2), 022001. https://doi.org/10.1117/1.JPE.6.022001.
(28) Gong, C.; Tong, S.; Huang, K.; Li, H.; Huang, H.; Zhang, J.; Yang, J. Flexible Planar Heterojunction Perovskite Solar Cells Fabricated via Sequential Roll-to-Roll Microgravure Printing and Slot-Die Coating Deposition. *Solar RRL* **2020**, *4* (2), 1900204. https://doi.org/10.1002/solr.201900204.
(29) Elangovan, N. K.; Kannadasan, R.; Beenarani, B. B.; Alsharif, M. H.; Kim, M.-K.; Hasan Inamul, Z. Recent Developments in Perovskite Materials, Fabrication Techniques, Band Gap Engineering, and the Stability of Perovskite Solar Cells. *Energy Reports* **2024**, *11*, 1171–1190. https://doi.org/10.1016/j.egyr.2023.12.068.
(30) Kiani, M. S.; Sadirkhanov, Z. T.; Kakimov, A. G.; Parkhomenko, H. P.; Ng, A.; Jumabekov, A. N. Solution-Processed SnO2 Quantum Dots for the Electron Transport Layer of Flexible and Printed Perovskite Solar Cells. *Nanomaterials* **2022**, *12* (15), 2615. https://doi.org/10.3390/nano12152615.
(31) Wu, X.; Xu, G.; Yang, F.; Chen, W.; Yang, H.; Shen, Y.; Wu, Y.; Chen, H.; Xi, J.; Tang, X.; Cheng, Q.; Chen, Y.; Ou, X.; Li, Y.; Li, Y. Realizing 23.9% Flexible Perovskite Solar Cells via Alleviating the Residual Strain Induced by Delayed Heat Transfer. *ACS Energy Lett.* **2023**, *8* (9), 3750–3759. https://doi.org/10.1021/acsenergylett.3c01167.
(32) Kiani, M. S.; Parkhomenko, H. P.; Mangrulkar, M.; Aigarayeva, S.; Akhanuly, A.; Shalenov, E. O.; Ng, A.; Jumabekov, A. N. Stepping toward Portable Optoelectronics with SnO_2 Quantum Dot-Based Electron Transport Layers. *ACS Omega* **2023**, *8* (23), 21212–21222. https://doi.org/10.1021/acsomega.3c02341.
(33) Elumalai, N. K.; Mahmud, M. A.; Wang, D.; Uddin, A. Perovskite Solar Cells: Progress and Advancements. *Energies* **2016**, *9* (11), 861. https://doi.org/10.3390/en9110861.
(34) Si, H.; Zhao, X.; Zhang, Z.; Liao, Q.; Zhang, Y. Low-Temperature Electron-Transporting Materials for Perovskite Solar Cells: Fundamentals, Progress, and Outlook. *Coordination Chemistry Reviews* **2024**, *500*, 215502. https://doi.org/10.1016/j.ccr.2023.215502.

(35) Bu, T.; Li, J.; Zheng, F.; Chen, W.; Wen, X.; Ku, Z.; Peng, Y.; Zhong, J.; Cheng, Y.-B.; Huang, F. Universal Passivation Strategy to Slot-Die Printed SnO2 for Hysteresis-Free Efficient Flexible Perovskite Solar Module. *Nat Commun* **2018**, *9* (1), 4609. https://doi.org/10.1038/s41467-018-07099-9.
(36) Tong, G.; Ono, L. K.; Liu, Y.; Zhang, H.; Bu, T.; Qi, Y. Up-Scalable Fabrication of SnO2 with Multifunctional Interface for High Performance Perovskite Solar Modules. *Nano-Micro Lett.* **2021**, *13* (1), 155. https://doi.org/10.1007/s40820-021-00675-7.
(37) Roy, P.; Ghosh, A.; Barclay, F.; Khare, A.; Cuce, E. Perovskite Solar Cells: A Review of the Recent Advances. *Coatings* **2022**, *12* (8), 1089. https://doi.org/10.3390/coatings12081089.
(38) Lin, L.; Jones, T. W.; Yang, T. C.; Duffy, N. W.; Li, J.; Zhao, L.; Chi, B.; Wang, X.; Wilson, G. J. Inorganic Electron Transport Materials in Perovskite Solar Cells. *Adv. Funct. Mater.* **2021**, *31* (5), 2008300. https://doi.org/10.1002/adfm.202008300.
(39) Zhang, J.; Zhang, W.; Cheng, H.-M.; Silva, S. R. P. Critical Review of Recent Progress of Flexible Perovskite Solar Cells. *Materials Today* **2020**, *39*, 66–88. https://doi.org/10.1016/j.mattod.2020.05.002.
(40) Lou, Q.; Han, Y.; Liu, C.; Zheng, K.; Zhang, J.; Chen, X.; Du, Q.; Chen, C.; Ge, Z. π-Conjugated Small Molecules Modified SnO2 Layer for Perovskite Solar Cells with over 23% Efficiency. *Advanced Energy Materials* **2021**, *11* (39), 2101416. https://doi.org/10.1002/aenm.202101416.
(41) Rao, C. N. R. Perovskites. In *Encyclopedia of Physical Science and Technology (Third Edition)*; Meyers, R. A., Ed.; Academic Press: New York, 2003; pp 707–714. https://doi.org/10.1016/B0-12-227410-5/00554-8.
(42) Song, Z.; Watthage, S. C.; Phillips, A. B.; Heben, M. J. Pathways toward High-Performance Perovskite Solar Cells: Review of Recent Advances in Organo-Metal Halide Perovskites for Photovoltaic Applications. *Journal of Photonics for Energy* **2016**, *6* (2). https://doi.org/10.1117/1.JPE.6.022001.
(43) Evolution of Perovskite Solar Cells. In *Perovskite Photovoltaics*; Academic Press, 2018; pp 43–88. https://doi.org/10.1016/B978-0-12-812915-9.00003-4.
(44) Akkerman, Q. A.; Manna, L. What Defines a Halide Perovskite? *ACS Energy Lett.* **2020**, *5* (2), 604–610. https://doi.org/10.1021/acsenergylett.0c00039.
(45) Brittman, S.; Adhyaksa, G. W. P.; Garnett, E. C. The Expanding World of Hybrid Perovskites: Materials Properties and Emerging Applications. *MRS Communications* **2015**, *5* (1), 7–26. https://doi.org/10.1557/mrc.2015.6.
(46) Li, C.; Lu, X.; Ding, W.; Feng, L.; Gao, Y.; Guo, Z. Formability of ABX3 (X = F, Cl, Br, I) Halide Perovskites. *Acta Cryst B* **2008**, *64* (6), 702–707. https://doi.org/10.1107/S0108768108032734.
(47) Li, Z.; Yang, M.; Park, J.-S.; Wei, S.-H.; Berry, J. J.; Zhu, K. Stabilizing Perovskite Structures by Tuning Tolerance Factor: Formation of Formamidinium and Cesium Lead Iodide Solid-State Alloys. *Chem. Mater.* **2016**, *28* (1), 284–292. https://doi.org/10.1021/acs.chemmater.5b04107.
(48) Sahoo, S. K.; Manoharan, B.; Sivakumar, N. Introduction. In *Perovskite Photovoltaics*; Elsevier, 2018; pp 1–24. https://doi.org/10.1016/B978-0-12-812915-9.00001-0.
(49) Masood, M. T. Solution-Processable Compact and Mesoporous Titanium Dioxide Thin Films as Electron-Selective Layers for Perovskite Solar Cells, 2020.
(50) Atta, N. F.; Galal, A.; El-Ads, E. H. Perovskite Nanomaterials – Synthesis, Characterization, and Applications. In *Perovskite Materials - Synthesis, Characterisation, Properties, and Applications*; Pan, L., Zhu, G., Eds.; InTech, 2016. https://doi.org/10.5772/61280.
(51) He, C.; Liu, X. The Rise of Halide Perovskite Semiconductors. *Light Sci Appl* **2023**, *12* (1), 15. https://doi.org/10.1038/s41377-022-01010-4.
(52) Usman, M.; ur Rehman, J.; Tahir, M. B.; Hussain, A. Structural, Electronics, Magnetic, Optical, Mechanical and Hydrogen Storage Properties of Ga-Based Hydride-Perovskites

XGaH3 (X = K, Li). *International Journal of Energy Research* **2022**, *46* (11), 15617–15626. https://doi.org/10.1002/er.8257.
(53) Chouhan, L.; Ghimire, S.; Subrahmanyam, C.; Miyasaka, T.; Biju, V. Synthesis, Optoelectronic Properties and Applications of Halide Perovskites. *Chem. Soc. Rev.* **2020**, *49* (10), 2869–2885. https://doi.org/10.1039/C9CS00848A.
(54) Gao, P.; Grätzel, M.; Nazeeruddin, M. K. Organohalide Lead Perovskites for Photovoltaic Applications. *Energy Environ. Sci.* **2014**, *7* (8), 2448–2463. https://doi.org/10.1039/C4EE00942H.
(55) Jung, H. S.; Park, N. Perovskite Solar Cells: From Materials to Devices. *Small* **2015**, *11* (1), 10–25. https://doi.org/10.1002/smll.201402767.
(56) Maculan, G.; Sheikh, A. D.; Abdelhady, A. L.; Saidaminov, M. I.; Haque, M. A.; Murali, B.; Alarousu, E.; Mohammed, O. F.; Wu, T.; Bakr, O. M. $CH_3NH_3PbCl_3$ Single Crystals: Inverse Temperature Crystallization and Visible-Blind UV-Photodetector. *J. Phys. Chem. Lett.* **2015**, *6* (19), 3781–3786. https://doi.org/10.1021/acs.jpclett.5b01666.
(57) Sun, S. Synthesis, Characterization and Properties of Hybrid Organic-Inorganic Perovskites for Photovoltaic Applications.
(58) Kang, R.; Yeo, J.-S.; Lee, H. J.; Lee, S.; Kang, M.; Myoung, N.; Yim, S.-Y.; Oh, S.-H.; Kim, D.-Y. Exploration of Fabrication Methods for Planar CH3NH3PbI3 Perovskite Solar Cells. *Nano Energy* **2016**, *27*, 175–184. https://doi.org/10.1016/j.nanoen.2016.06.052.
(59) Li, J.; Bu, T.; Liu, Y.; Zhou, J.; Shi, J.; Ku, Z.; Peng, Y.; Zhong, J.; Cheng, Y.-B.; Huang, F. Enhanced Crystallinity of Low-Temperature Solution-Processed SnO2 for Highly Reproducible Planar Perovskite Solar Cells. *ChemSusChem* **2018**, *11* (17), 2898–2903. https://doi.org/10.1002/cssc.201801433.
(60) Ren, N.; Tan, L.; Li, M.; Zhou, J.; Ye, Y.; Jiao, B.; Ding, L.; Yi, C. 25% - Efficiency Flexible Perovskite Solar Cells via Controllable Growth of SnO2. *iEnergy* **2024**, *3* (1), 39–45. https://doi.org/10.23919/IEN.2024.0001.
(61) Vijayaraghavan, S. N.; Wall, J.; Li, L.; Xing, G.; Zhang, Q.; Yan, F. Low-Temperature Processed Highly Efficient Hole Transport Layer Free Carbon-Based Planar Perovskite Solar Cells with SnO2 Quantum Dot Electron Transport Layer. *Materials Today Physics* **2020**, *13*, 100204. https://doi.org/10.1016/j.mtphys.2020.100204.
(62) Xu, F.; Liu, J.; Subbiah, A. S.; Liu, W.; Kang, J.; Harrison, G. T.; Yang, X.; Isikgor, F. H.; Aydin, E.; De Bastiani, M.; De Wolf, S. Potassium Thiocyanate-Assisted Enhancement of Slot-Die-Coated Perovskite Films for High-Performance Solar Cells. *Small Science* **2021**, *1* (5), 2000044. https://doi.org/10.1002/smsc.202000044.
(63) Ren, Z.; Liu, K.; Hu, H.; Guo, X.; Gao, Y.; Fong, P. W. K.; Liang, Q.; Tang, H.; Huang, J.; Zhang, H.; Qin, M.; Cui, L.; Chandran, H. T.; Shen, D.; Lo, M.-F.; Ng, A.; Surya, C.; Shao, M.; Lee, C.-S.; Lu, X.; Laquai, F.; Zhu, Y.; Li, G. Room-Temperature Multiple Ligands-Tailored SnO2 Quantum Dots Endow in Situ Dual-Interface Binding for Upscaling Efficient Perovskite Photovoltaics with High VOC. *Light Sci Appl* **2021**, *10* (1), 239. https://doi.org/10.1038/s41377-021-00676-6.
(64) Wang, H.; Cao, S.; Yang, B.; Li, H.; Wang, M.; Hu, X.; Sun, K.; Zang, Z. NH_4Cl-Modified ZnO for High-Performance $CsPbIBr_2$ Perovskite Solar Cells via Low-Temperature Process. *Sol. RRL* **2020**, *4* (1), 1900363. https://doi.org/10.1002/solr.201900363.
(65) Song, T.-B.; Chen, Q.; Zhou, H.; Jiang, C.; Wang, H.-H.; Yang, Y. (Michael); Liu, Y.; You, J.; Yang, Y. Perovskite Solar Cells: Film Formation and Properties. *Journal of Materials Chemistry A* **2015**, *3* (17), 9032–9050. https://doi.org/10.1039/C4TA05246C.
(66) Ansari, M. I. H.; Qurashi, A.; Nazeeruddin, M. K. Frontiers, Opportunities, and Challenges in Perovskite Solar Cells: A Critical Review. *Journal of Photochemistry and Photobiology C: Photochemistry Reviews* **2018**, *35*, 1–24. https://doi.org/10.1016/j.jphotochemrev.2017.11.002.

(67) M. Rombach, F.; A. Haque, S.; J. Macdonald, T. Lessons Learned from Spiro-OMeTAD and PTAA in Perovskite Solar Cells. *Energy & Environmental Science* **2021**, *14* (10), 5161–5190. https://doi.org/10.1039/D1EE02095A.
(68) Rana, N. K.; Das, T.; Garg, P.; Bera, A.; Guchhait, A. PTAA/Ag-Based Large Area Perovskite Solar Cells Toward Low-Cost and Ambient Stability. *J. Phys. Chem. C* **2023**, *127* (45), 21954–21962. https://doi.org/10.1021/acs.jpcc.3c04037.
(69) Holzhey, P.; Prettl, M.; Collavini, S.; Mortan, C.; Saliba, M. Understanding the Impact of Surface Roughness: Changing from FTO to ITO to PEN/ITO for Flexible Perovskite Solar Cells. *Sci Rep* **2023**, *13* (1), 6375. https://doi.org/10.1038/s41598-023-33147-6.
(70) Xiong, S.; Yuan, M.; Yang, J.; Song, J.; Guo, X.; Li, X.; Li, B.; Liu, X.; Duan, C.; Liu, F.; Fahlman, M.; Bao, Q. Engineering of the Back Contact between PCBM and Metal Electrode for Planar Perovskite Solar Cells with Enhanced Efficiency and Stability. *Advanced Optical Materials* **2019**, *7* (19), 1900542. https://doi.org/10.1002/adom.201900542.
(71) Hussain, I.; Tran, H. P.; Jaksik, J.; Moore, J.; Islam, N.; Uddin, M. J. Functional Materials, Device Architecture, and Flexibility of Perovskite Solar Cell. *emergent mater.* **2018**, *1* (3), 133–154. https://doi.org/10.1007/s42247-018-0013-1.
(72) Tao, J.; Liu, X.; Shen, J.; Wang, H.; Xue, J.; Su, C.; Guo, H.; Fu, G.; Kong, W.; Yang, S. Functionalized SnO2 Films by Using EDTA-2 M for High Efficiency Perovskite Solar Cells with Efficiency over 23%. *Chemical Engineering Journal* **2022**, *430*, 132683. https://doi.org/10.1016/j.cej.2021.132683.
(73) Wu, C.-G.; Chiang, C.-H.; Tseng, Z.-L.; K. Nazeeruddin, M.; Hagfeldt, A.; Grätzel, M. High Efficiency Stable Inverted Perovskite Solar Cells without Current Hysteresis. *Energy & Environmental Science* **2015**, *8* (9), 2725–2733. https://doi.org/10.1039/C5EE00645G.
(74) *Recent Advances in the Inverted Planar Structure of Perovskite Solar Cells | Accounts of Chemical Research*. https://pubs.acs.org/doi/full/10.1021/acs.accounts.5b00404 (accessed 2024-02-04).
(75) Chen, W.; Yin, X.; Que, M.; Xie, H.; Liu, J.; Yang, C.; Guo, Y.; Wu, Y.; Que, W. A Comparative Study of Planar and Mesoporous Perovskite Solar Cells with Printable Carbon Electrodes. *Journal of Power Sources* **2019**, *412*, 118–124. https://doi.org/10.1016/j.jpowsour.2018.11.031.
(76) Singh, R.; Sandhu, S.; Lee, J.-J. Elucidating the Effect of Shunt Losses on the Performance of Mesoporous Perovskite Solar Cells. *Solar Energy* **2019**, *193*, 956–961. https://doi.org/10.1016/j.solener.2019.10.018.
(77) Yin, X.; Zhai, J.; Song, L.; Du, P.; Li, N.; Yang, Y.; Xiong, J.; Ko, F. Novel NiO Nanoforest Architecture for Efficient Inverted Mesoporous Perovskite Solar Cells. *ACS Appl. Mater. Interfaces* **2019**, *11* (47), 44308–44314. https://doi.org/10.1021/acsami.9b15820.
(78) Jan, S. T.; Noman, M. Analyzing the Effect of Planar and Inverted Structure Architecture on the Properties of MAGeI3 Perovskite Solar Cells. *Energy Technology* **2023**, *11* (11), 2300564. https://doi.org/10.1002/ente.202300564.
(79) Park, N.-G. Research Direction toward Scalable, Stable, and High Efficiency Perovskite Solar Cells. *Advanced Energy Materials* **2020**, *10* (13), 1903106. https://doi.org/10.1002/aenm.201903106.
(80) *A Review on Scaling Up Perovskite Solar Cells - Li - 2021 - Advanced Functional Materials - Wiley Online Library*. https://onlinelibrary.wiley.com/doi/full/10.1002/adfm.202008621 (accessed 2024-02-05).
(81) Ahmed Chowdhury, T.; Zafar, M. A. B.; Islam, M. S.-U.; Shahinuzzaman, M.; Aminul Islam, M.; Uddin Khandaker, M. Stability of Perovskite Solar Cells: Issues and Prospects. *RSC Advances* **2023**, *13* (3), 1787–1810. https://doi.org/10.1039/D2RA05903G.
(82) McMeekin, D. P.; Holzhey, P.; Fürer, S. O.; Harvey, S. P.; Schelhas, L. T.; Ball, J. M.; Mahesh, S.; Seo, S.; Hawkins, N.; Lu, J.; Johnston, M. B.; Berry, J. J.; Bach, U.; Snaith, H. J. Intermediate-Phase Engineering via Dimethylammonium Cation Additive for Stable

Perovskite Solar Cells. *Nat. Mater.* **2023**, *22* (1), 73–83. https://doi.org/10.1038/s41563-022-01399-8.

(83) Hsu, H.-C.; Hong, S.-T.; Wu, S.-H.; Shih, C.-F. A Poly(Methyl Methacrylate)-Encapsulated Perovskite Solar Antenna with a Long Lifespan. *Organic Electronics* **2023**, *114*, 106748. https://doi.org/10.1016/j.orgel.2023.106748.

(84) Ma, S.; Yuan, G.; Zhang, Y.; Yang, N.; Li, Y.; Chen, Q. Development of Encapsulation Strategies towards the Commercialization of Perovskite Solar Cells. *Energy & Environmental Science* **2022**, *15* (1), 13–55. https://doi.org/10.1039/D1EE02882K.

(85) Li, J.; Xia, R.; Qi, W.; Zhou, X.; Cheng, J.; Chen, Y.; Hou, G.; Ding, Y.; Li, Y.; Zhao, Y.; Zhang, X. Encapsulation of Perovskite Solar Cells for Enhanced Stability: Structures, Materials and Characterization. *Journal of Power Sources* **2021**, *485*, 229313. https://doi.org/10.1016/j.jpowsour.2020.229313.

(86) Babayigit, A.; Ethirajan, A.; Muller, M.; Conings, B. Toxicity of Organometal Halide Perovskite Solar Cells. *Nature Mater* **2016**, *15* (3), 247–251. https://doi.org/10.1038/nmat4572.

(87) Liu, W.-W.; Wu, T.-H.; Liu, M.-C.; Niu, W.-J.; Chueh, Y.-L. Recent Challenges in Perovskite Solar Cells Toward Enhanced Stability, Less Toxicity, and Large-Area Mass Production. *Advanced Materials Interfaces* **2019**, *6* (9), 1801758. https://doi.org/10.1002/admi.201801758.

(88) Cai, B.; Zhang, W.-H.; Qiu, J. Solvent Engineering of Spin-Coating Solutions for Planar-Structured High-Efficiency Perovskite Solar Cells. *Chinese Journal of Catalysis* **2015**, *36* (8), 1183–1190. https://doi.org/10.1016/S1872-2067(15)60929-9.

(89) *Inkjet-Printed Triple Cation Perovskite Solar Cells | ACS Applied Energy Materials*. https://pubs.acs.org/doi/full/10.1021/acsaem.8b00222 (accessed 2024-02-05).

(90) Huckaba, A. J.; Lee, Y.; Xia, R.; Paek, S.; Bassetto, V. C.; Oveisi, E.; Lesch, A.; Kinge, S.; Dyson, P. J.; Girault, H.; Nazeeruddin, M. K. Inkjet-Printed Mesoporous TiO2 and Perovskite Layers for High Efficiency Perovskite Solar Cells. *Energy Technology* **2019**, *7* (2), 317–324. https://doi.org/10.1002/ente.201800905.

(91) *Blade-Coated Hybrid Perovskite Solar Cells with Efficiency > 17%: An In Situ Investigation | ACS Energy Letters*. https://pubs.acs.org/doi/full/10.1021/acsenergylett.8b00428 (accessed 2024-02-05).

(92) Tu, Y.; Ye, J.; Yang, G.; Zang, Y.; Zhang, L.; Wang, Y.; Li, G.; Chu, L.; Yan, W. Slot-Die Coating Fabrication of Perovskite Solar Cells toward Commercialization. *Journal of Alloys and Compounds* **2023**, *942*, 169104. https://doi.org/10.1016/j.jallcom.2023.169104.

(93) Valsalakumar, S.; Roy, A.; Mallick, T. K.; Hinshelwood, J.; Sundaram, S. An Overview of Current Printing Technologies for Large-Scale Perovskite Solar Cell Development. *Energies* **2022**, *16* (1), 190. https://doi.org/10.3390/en16010190.

(94) Li, F.; Lin, F. R.; Jen, A. K.-Y. Current State and Future Perspectives of Printable Organic and Perovskite Solar Cells. *Advanced Materials n/a* (n/a), 2307161. https://doi.org/10.1002/adma.202307161.

(95) Hwang, K.; Jung, Y.-S.; Heo, Y.-J.; Scholes, F. H.; Watkins, S. E.; Subbiah, J.; Jones, D. J.; Kim, D.-Y.; Vak, D. Toward Large Scale Roll-to-Roll Production of Fully Printed Perovskite Solar Cells. *Advanced Materials* **2015**, *27* (7), 1241–1247. https://doi.org/10.1002/adma.201404598.

(96) Di Giacomo, F.; Shanmugam, S.; Fledderus, H.; Bruijnaers, B. J.; Verhees, W. J. H.; Dorenkamper, M. S.; Veenstra, S. C.; Qiu, W.; Gehlhaar, R.; Merckx, T.; Aernouts, T.; Andriessen, R.; Galagan, Y. Up-Scalable Sheet-to-Sheet Production of High Efficiency Perovskite Module and Solar Cells on 6-in. Substrate Using Slot Die Coating. *Solar Energy Materials and Solar Cells* **2018**, *181*, 53–59. https://doi.org/10.1016/j.solmat.2017.11.010.

(97) Li, J.; Dagar, J.; Shargaieva, O.; Maus, O.; Remec, M.; Emery, Q.; Khenkin, M.; Ulbrich, C.; Akhundova, F.; Márquez, J. A.; Unold, T.; Fenske, M.; Schultz, C.; Stegemann, B.; Al-Ashouri, A.; Albrecht, S.; Esteves, A. T.; Korte, L.; Köbler, H.; Abate, A.; Többens, D. M.;

Zizak, I.; List-Kratochvil, E. J. W.; Schlatmann, R.; Unger, E. Ink Design Enabling Slot-Die Coated Perovskite Solar Cells with >22% Power Conversion Efficiency, Micro-Modules, and 1 Year of Outdoor Performance Evaluation. *Advanced Energy Materials* **2023**, *13* (33), 2203898. https://doi.org/10.1002/aenm.202203898.

(98) Sears, K. K.; Fievez, M.; Gao, M.; Weerasinghe, H. C.; Easton, C. D.; Vak, D. ITO-Free Flexible Perovskite Solar Cells Based on Roll-to-Roll, Slot-Die Coated Silver Nanowire Electrodes. **2017**, 9.

(99) Hong, S.; Lee, J.; Kang, H.; Lee, K. Slot-Die Coating Parameters of the Low-Viscosity Bulk-Heterojunction Materials Used for Polymer Solarcells. *Solar Energy Materials and Solar Cells* **2013**, *112*, 27–35. https://doi.org/10.1016/j.solmat.2013.01.006.

(100) Humphreys, C. J. The Significance of Bragg's Law in Electron Diffraction and Microscopy, and Bragg's Second Law. *Acta Cryst A* **2013**, *69* (1), 45–50. https://doi.org/10.1107/S0108767312047587.

(101) Muniz, F. T. L.; Miranda, M. A. R.; Morilla Dos Santos, C.; Sasaki, J. M. The Scherrer Equation and the Dynamical Theory of X-Ray Diffraction. *Acta Crystallogr A Found Adv* **2016**, *72* (3), 385–390. https://doi.org/10.1107/S205327331600365X.

(102) Jumabekov, A. N. Lead sulfide quantum dot-based nanostructured solar cells. Text.PhDThesis, Ludwig-Maximilians-Universität München, 2014. https://edoc.ub.uni-muenchen.de/17596/ (accessed 2024-05-14).

(103) Swinehart, D. F. The Beer-Lambert Law. *J. Chem. Educ.* **1962**, *39* (7), 333. https://doi.org/10.1021/ed039p333.

(104) Lin, C.-F.; Zhang, M.; Liu, S.-W.; Chiu, T.-L.; Lee, J.-H. High Photoelectric Conversion Efficiency of Metal Phthalocyanine/Fullerene Heterojunction Photovoltaic Device. *International Journal of Molecular Sciences* **2011**, *12* (1), 476–505. https://doi.org/10.3390/ijms12010476.

(105) Parkhomenko, H. P.; Yerlanuly, Y.; Brus, V. V.; Jumabekov, A. N. Effect of Mild Mechanical Stresses on Device Physics of Slot-Die Coated Flexible Perovskite Solar Cells. *Organic Electronics* **2024**, *129*, 107049. https://doi.org/10.1016/j.orgel.2024.107049.

(106) García de Arquer, F. P.; Talapin, D. V.; Klimov, V. I.; Arakawa, Y.; Bayer, M.; Sargent, E. H. Semiconductor Quantum Dots: Technological Progress and Future Challenges. *Science* **2021**, *373* (6555), eaaz8541. https://doi.org/10.1126/science.aaz8541.

(107) Kim, M.; Jeong, J.; Lu, H.; Lee, T. K.; Eickemeyer, F. T.; Liu, Y.; Choi, I. W.; Choi, S. J.; Jo, Y.; Kim, H.-B.; Mo, S.-I.; Kim, Y.-K.; Lee, H.; An, N. G.; Cho, S.; Tress, W. R.; Zakeeruddin, S. M.; Hagfeldt, A.; Kim, J. Y.; Grätzel, M.; Kim, D. S. Conformal Quantum Dot–SnO2 Layers as Electron Transporters for Efficient Perovskite Solar Cells. *Science* **2022**, *375* (6578), 302–306. https://doi.org/10.1126/science.abh1885.

(108) Chen, W.; Zhou, Q.; Wan, F.; Gao, T. Gas Sensing Properties and Mechanism of Nano-SnO_2-Based Sensor for Hydrogen and Carbon Monoxide. *Journal of Nanomaterials* **2012**, *2012*, 1–9. https://doi.org/10.1155/2012/612420.

(109) T. Lamdhade, G.; C. Raghuwanshi, F.; M. Agrawal, R.; M. Balkhande, V.; Shripath, T. SnO2 Nanoparticles Synthesis Via Liquid-Phase Co-Precipitation Technique. *Adv. Mater. Lett.* **2015**, *6* (8), 738–742. https://doi.org/10.5185/amlett.2015.5877.

(110) Rani, R.; Sharma, S. Preparation and Characterization of SnO2 Nanofibers via Electrospinning. *Advances in Nanoparticles* **2016**, *5* (1), 53–59. https://doi.org/10.4236/anp.2016.51006.

(111) Zhu, H.; Yang, D.; Yu, G.; Zhang, H.; Yao, K. A Simple Hydrothermal Route for Synthesizing SnO2quantum Dots. *Nanotechnology* **2006**, *17* (9), 2386–2389. https://doi.org/10.1088/0957-4484/17/9/052.

(112) Halvani Anaraki, E.; Kermanpur, A.; Steier, L.; Domanski, K.; Matsui, T.; Tress, W.; Saliba, M.; Abate, A.; Grätzel, M.; Hagfeldt, A.; Correa-Baena, J.-P. Highly Efficient and Stable Planar Perovskite Solar Cells by Solution-Processed Tin Oxide. *Energy & Environmental Science* **2016**, *9* (10), 3128–3134. https://doi.org/10.1039/C6EE02390H.

(113) Ke, W.; Fang, G.; Liu, Q.; Xiong, L.; Qin, P.; Tao, H.; Wang, J.; Lei, H.; Li, B.; Wan, J.; Yang, G.; Yan, Y. Low-Temperature Solution-Processed Tin Oxide as an Alternative Electron Transporting Layer for Efficient Perovskite Solar Cells. *J. Am. Chem. Soc.* **2015**, *137* (21), 6730–6733. https://doi.org/10.1021/jacs.5b01994.
(114) Bhattacharjee, A.; Ahmaruzzaman, M. A Novel and Green Process for the Production of Tin Oxide Quantum Dots and Its Application as a Photocatalyst for the Degradation of Dyes from Aqueous Phase. *Journal of Colloid and Interface Science* **2015**, *448*, 130–139. https://doi.org/10.1016/j.jcis.2015.01.083.
(115) Xie, J.; Huang, K.; Yu, X.; Yang, Z.; Xiao, K.; Qiang, Y.; Zhu, X.; Xu, L.; Wang, P.; Cui, C.; Yang, D. Enhanced Electronic Properties of SnO_2 *via* Electron Transfer from Graphene Quantum Dots for Efficient Perovskite Solar Cells. *ACS Nano* **2017**, *11* (9), 9176–9182. https://doi.org/10.1021/acsnano.7b04070.
(116) Ou, X.-L.; Feng, J.; Xu, M.; Sun, H.-B. Semitransparent and Flexible Perovskite Solar Cell with High Visible Transmittance Based on Ultrathin Metallic Electrodes. *Opt. Lett., OL* **2017**, *42* (10), 1958–1961. https://doi.org/10.1364/OL.42.001958.
(117) *Remarkably high performance of organic photovoltaic devices with 3,9-bis(2-methylene-(3-(1,1-dicyanomethylene)-indanone))-5,5,11,11-tetrakis(4-hexyl meta-phenyl)-dithieno[2,3-d:2',3'-d']-s-indaceno[1,2-b:5,6-b']dithiophene)- ethylhexyloxy] photoactive acceptor under halogen light illumination - ScienceDirect*. https://www.sciencedirect.com/science/article/pii/S0378775321012738 (accessed 2022-06-30).
(118) *Elastomeric Indoor Organic Photovoltaics with Superb Photothermal Endurance - Kim - - Advanced Functional Materials - Wiley Online Library*. https://onlinelibrary.wiley.com/doi/abs/10.1002/adfm.202201921 (accessed 2022-06-30).
(119) Jeyakumar, R.; Bag, A.; Nekovei, R.; Radhakrishnan, R. Influence of Electron Transport Layer (TiO2) Thickness and Its Doping Density on the Performance of CH3NH3PbI3-Based Planar Perovskite Solar Cells. *Journal of Elec Materi* **2020**, *49* (6), 3533–3539. https://doi.org/10.1007/s11664-020-08041-w.
(120) *Impact of Interfacial Layers in Perovskite Solar Cells - Cho - 2017 - ChemSusChem - Wiley Online Library*. https://chemistry-europe.onlinelibrary.wiley.com/doi/full/10.1002/cssc.201701095 (accessed 2022-05-31).
(121) Habisreutinger, S. N.; Noel, N. K.; Snaith, H. J. Hysteresis Index: A Figure without Merit for Quantifying Hysteresis in Perovskite Solar Cells. *ACS Energy Lett.* **2018**, *3* (10), 2472–2476. https://doi.org/10.1021/acsenergylett.8b01627.
(122) Cao, Q.; Li, Y.; Zhang, H.; Yang, J.; Han, J.; Xu, T.; Wang, S.; Wang, Z.; Gao, B.; Zhao, J.; Li, X.; Ma, X.; Zakeeruddin, S. M.; Sha, W. E. I.; Li, X.; Grätzel, M. Efficient and Stable Inverted Perovskite Solar Cells with Very High Fill Factors via Incorporation of Star-Shaped Polymer. *Science Advances 7* (28), eabg0633. https://doi.org/10.1126/sciadv.abg0633.
(123) Rai, M.; Wong, L. H.; Etgar, L. Effect of Perovskite Thickness on Electroluminescence and Solar Cell Conversion Efficiency. *J. Phys. Chem. Lett.* **2020**, *11* (19), 8189–8194. https://doi.org/10.1021/acs.jpclett.0c02363.
(124) Tan, H.; Jain, A.; Voznyy, O.; Lan, X.; García de Arquer, F. P.; Fan, J. Z.; Quintero-Bermudez, R.; Yuan, M.; Zhang, B.; Zhao, Y.; Fan, F.; Li, P.; Quan, L. N.; Zhao, Y.; Lu, Z.-H.; Yang, Z.; Hoogland, S.; Sargent, E. H. Efficient and Stable Solution-Processed Planar Perovskite Solar Cells via Contact Passivation. *Science* **2017**, *355* (6326), 722–726. https://doi.org/10.1126/science.aai9081.
(125) Weber, S.; Rath, T.; Mangalam, J.; Kunert, B.; Coclite, A. M.; Bauch, M.; Dimopoulos, T.; Trimmel, G. Investigation of NiOx-Hole Transport Layers in Triple Cation Perovskite Solar Cells. *J Mater Sci: Mater Electron* **2018**, *29* (3), 1847–1855. https://doi.org/10.1007/s10854-017-8094-9.

(126) Hoang, V. Q.; Lee, S. K.; Bark, C. W. Dispersed SnO2 Colloids Using Sodium Dodecyl Benzene Sulfonate for High-Performance Planar Perovskite Solar Cells. *Solar Energy* **2021**, *230*, 747–753. https://doi.org/10.1016/j.solener.2021.10.081.
(127) Jo Kim, B.; Hoe Kim, D.; Lee, Y.-Y.; Shin, H.-W.; Sang Han, G.; Sug Hong, J.; Mahmood, K.; Kyu Ahn, T.; Joo, Y.-C.; Sun Hong, K.; Park, N.-G.; Lee, S.; Suk Jung, H. Highly Efficient and Bending Durable Perovskite Solar Cells: Toward a Wearable Power Source. *Energy & Environmental Science* **2015**, *8* (3), 916–921. https://doi.org/10.1039/C4EE02441A.
(128) Wang, C.; Guan, L.; Zhao, D.; Yu, Y.; Grice, C. R.; Song, Z.; Awni, R. A.; Chen, J.; Wang, J.; Zhao, X.; Yan, Y. Water Vapor Treatment of Low-Temperature Deposited SnO_2 Electron Selective Layers for Efficient Flexible Perovskite Solar Cells. *ACS Energy Lett.* **2017**, *2* (9), 2118–2124. https://doi.org/10.1021/acsenergylett.7b00644.
(129) *High Bending Durability of Efficient Flexible Perovskite Solar Cells Using Metal Oxide Electron Transport Layer | The Journal of Physical Chemistry C*. https://pubs.acs.org/doi/10.1021/acs.jpcc.8b05008 (accessed 2022-07-12).
(130) Heo, J. H.; Shin, D. H.; Jang, M. H.; Lee, M. L.; Kang, M. G.; Im, S. H. Highly Flexible, High-Performance Perovskite Solar Cells with Adhesion Promoted AuCl3-Doped Graphene Electrodes. *J. Mater. Chem. A* **2017**, *5* (40), 21146–21152. https://doi.org/10.1039/C7TA06465A.
(131) Popoola, I. K.; Gondal, M. A.; Qahtan, T. F. Recent Progress in Flexible Perovskite Solar Cells: Materials, Mechanical Tolerance and Stability. *Renewable and Sustainable Energy Reviews* **2018**, *82*, 3127–3151. https://doi.org/10.1016/j.rser.2017.10.028.
(132) Lee, G.; Kim, M.; Choi, Y. W.; Ahn, N.; Jang, J.; Yoon, J.; Kim, S. M.; Lee, J.-G.; Kang, D.; Jung, H. S.; Choi, M. Ultra-Flexible Perovskite Solar Cells with Crumpling Durability: Toward a Wearable Power Source. *Energy Environ. Sci.* **2019**, *12* (10), 3182–3191. https://doi.org/10.1039/C9EE01944H.
(133) Cheacharoen, R.; Rolston, N.; Harwood, D.; Bush, K. A.; Dauskardt, R. H.; McGehee, M. D. Design and Understanding of Encapsulated Perovskite Solar Cells to Withstand Temperature Cycling. *Energy Environ. Sci.* **2018**, *11* (1), 144–150. https://doi.org/10.1039/C7EE02564E.
(134) Jiang, N.-R.; Wang, Y.-F.; Dong, Q.-F.; Ge, C.-D.; Yang, Z.-Q.; Yin, D.; Liu, Y.-F.; Bi, Y.-G.; Feng, J.; Sun, H.-B. Enhanced Efficiency and Mechanical Robustness of Flexible Perovskite Solar Cells by Using HPbI3 Additive. *Solar RRL* **2021**, *5* (4), 2000821. https://doi.org/10.1002/solr.202000821.
(135) *Impact of interlayer application on band bending for improved electron extraction for efficient flexible perovskite mini-modules - ScienceDirect*. https://www.sciencedirect.com/science/article/pii/S2211285518302866?via%3Dihub (accessed 2022-07-12).
(136) Altinkaya, C.; Aydin, E.; Ugur, E.; Isikgor, F. H.; Subbiah, A. S.; De Bastiani, M.; Liu, J.; Babayigit, A.; Allen, T. G.; Laquai, F.; Yildiz, A.; De Wolf, S. Tin Oxide Electron-Selective Layers for Efficient, Stable, and Scalable Perovskite Solar Cells. *Advanced Materials* **2021**, *33* (15), 2005504. https://doi.org/10.1002/adma.202005504.
(137) Chander, S.; Purohit, A.; Nehra, A.; Nehra, S. P.; Dhaka, M. S. A Study on Spectral Response and External Quantum Efficiency of Mono-Crystalline Silicon Solar Cell. **2015**, 4.
(138) Slami, A.; Benramdane, N. Manual Method for Measuring The External Quantum Efficiency for Solar Cells. *E3S Web Conf.* **2021**, *229*, 01005. https://doi.org/10.1051/e3sconf/202122901005.
(139) Laquai, F.; Andrienko, D.; Deibel, C.; Neher, D. *Charge Carrier Generation, Recombination, and Extraction in Polymer–Fullerene Bulk Heterojunction Organic Solar Cells.*; Springer, Cham; Vol. 272.

(140) Karki, A.; Vollbrecht, J.; Gillett, A. J.; Selter, P.; Lee, J.; Peng, Z.; Schopp, N.; Dixon, A. L.; Schrock, M.; Nádaždy, V.; Schauer, F.; Ade, H.; Chmelka, B. F.; Bazan, G. C.; Friend, R. H.; Nguyen, T.-Q. Unifying Charge Generation, Recombination, and Extraction in Low-Offset Non-Fullerene Acceptor Organic Solar Cells. *Advanced Energy Materials* **2020**, *10* (29), 2001203. https://doi.org/10.1002/aenm.202001203.
(141) Sze, S. M.; Li, Y.; Ng, K. K. *Physics of Semiconductor Devices*; John Wiley & Sons, 2021.
(142) Wagner, L.; Schygulla, P.; Herterich, J. P.; Elshamy, M.; Bogachuk, D.; Zouhair, S.; Mastroianni, S.; Würfel, U.; Liu, Y.; Zakeeruddin, S. M.; Grätzel, M.; Hinsch, A.; Glunz, S. W. Revealing Fundamentals of Charge Extraction in Photovoltaic Devices through Potentiostatic Photoluminescence Imaging. *Matter* **2022**, *5* (7), 2352–2364. https://doi.org/10.1016/j.matt.2022.05.024.
(143) Parkhomenko, H. P.; Shalenov, E. O.; Umatova, Z.; Dzhumagulova, K. N.; Jumabekov, A. N. Fabrication of Flexible Quasi-Interdigitated Back-Contact Perovskite Solar Cells. *Energies* **2022**, *15* (9), 3056. https://doi.org/10.3390/en15093056.
(144) Le Corre, V. M.; Duijnstee, E. A.; El Tambouli, O.; Ball, J. M.; Snaith, H. J.; Lim, J.; Koster, L. J. A. Revealing Charge Carrier Mobility and Defect Densities in Metal Halide Perovskites via Space-Charge-Limited Current Measurements. *ACS Energy Lett.* **2021**, *6* (3), 1087–1094. https://doi.org/10.1021/acsenergylett.0c02599.
(145) Han, X.; Wang, X.; Feng, J.; Huang, H.; Zhu, Z.; Yu, T.; Li, Z.; Zou, Z. Carrier Mobility Enhancement in (121)-Oriented CsPbBr3 Perovskite Films Induced by the Microstructure Tailoring of PbBr2 Precursor Films. *ACS Appl. Electron. Mater.* **2021**, *3* (1), 373–384. https://doi.org/10.1021/acsaelm.0c00909.
(146) Yang, D.; Yang, R.; Ren, X.; Zhu, X.; Yang, Z.; Li, C.; Liu, S. (Frank). Hysteresis-Suppressed High-Efficiency Flexible Perovskite Solar Cells Using Solid-State Ionic-Liquids for Effective Electron Transport. *Advanced Materials* **2016**, *28* (26), 5206–5213. https://doi.org/10.1002/adma.201600446.
(147) Wu, X.; Li, H.; Wang, K.; Sun, X.; Wang, L. CH3NH3Pb1−xEuxI3 Mixed Halide Perovskite for Hybrid Solar Cells: The Impact of Divalent Europium Doping on Efficiency and Stability. *RSC Adv.* **2018**, *8* (20), 11095–11101. https://doi.org/10.1039/C7RA12754E.
(148) Poglitsch, A.; Weber, D. Dynamic Disorder in Methylammoniumtrihalogenoplumbates (II) Observed by Millimeter-wave Spectroscopy. *J. Chem. Phys.* **1987**, *87* (11), 6373–6378. https://doi.org/10.1063/1.453467.
(149) Feng, Y.; Liu, R.; Li, F.; Jin, M.; Du, Q.; Rong, Y.; Hu, H.; Wang, M.; Li, Y.; Shen, Z.; Liu, Y.; Li, H.; Chen, C. A Synergistic Co-Passivation Strategy for High-Performance Perovskite Solar Cells with Large Open Circuit Voltage. *Journal of Materials Chemistry C* **2022**, *10* (35), 12699–12707. https://doi.org/10.1039/D2TC02632E.
(150) Guo, R.; Bao, C.; Gao, F.; Tian, J. Double Active Layers Constructed with Halide Perovskite and Quantum Dots for Broadband Photodetection. *Advanced Optical Materials* **2020**, *8* (17), 2000557. https://doi.org/10.1002/adom.202000557.
(151) Jia, P.; Qin, L.; Zhao, D.; Tang, Y.; Song, B.; Guo, J.; Li, X.; Li, L.; Cui, Q.; Hu, Y.; Lou, Z.; Teng, F.; Hou, Y. The Trapped Charges at Grain Boundaries in Perovskite Solar Cells. *Advanced Functional Materials* **2021**, *31* (49), 2107125. https://doi.org/10.1002/adfm.202107125.
(152) Brus, V. V.; Schopp, N.; Ko, S.-J.; Vollbrecht, J.; Lee, J.; Karki, A.; Bazan, G. C.; Nguyen, T.-Q. Temperature and Light Modulated Open-Circuit Voltage in Nonfullerene Organic Solar Cells with Different Effective Bandgaps. *Advanced Energy Materials* **2021**, *11* (4), 2003091. https://doi.org/10.1002/aenm.202003091.
(153) Tress, W.; Yavari, M.; Domanski, K.; Yadav, P.; Niesen, B.; Baena, J. P. C.; Hagfeldt, A.; Graetzel, M. Interpretation and Evolution of Open-Circuit Voltage, Recombination, Ideality Factor and Subgap Defect States during Reversible Light-Soaking and Irreversible Degradation of Perovskite Solar Cells. *Energy Environ. Sci.* **2018**, *11* (1), 151–165. https://doi.org/10.1039/C7EE02415K.

(154) Brus, V. V.; Proctor, C. M.; Ran, N. A.; Nguyen, T.-Q. Capacitance Spectroscopy for Quantifying Recombination Losses in Nonfullerene Small-Molecule Bulk Heterojunction Solar Cells. *Advanced Energy Materials* **2016**, *6* (11), 1502250. https://doi.org/10.1002/aenm.201502250.
(155) Kirchartz, T.; Deledalle, F.; Tuladhar, P. S.; Durrant, J. R.; Nelson, J. On the Differences between Dark and Light Ideality Factor in Polymer:Fullerene Solar Cells. *J. Phys. Chem. Lett.* **2013**, *4* (14), 2371–2376. https://doi.org/10.1021/jz4012146.
(156) Fahrenbruch, A.; Bube, R. *Fundamentals Of Solar Cells: Photovoltaic Solar Energy Conversion*; Elsevier, 2012.
(157) Kirchartz, T.; Nelson, J. Meaning of Reaction Orders in Polymer:Fullerene Solar Cells. *Phys. Rev. B* **2012**, *86* (16), 165201. https://doi.org/10.1103/PhysRevB.86.165201.
(158) Lei, Y.; Xu, Y.; Wang, M.; Zhu, G.; Jin, Z. Origin, Influence, and Countermeasures of Defects in Perovskite Solar Cells. *Small* **2021**, *17* (26), 2005495. https://doi.org/10.1002/smll.202005495.
(159) Ball, J. M.; Petrozza, A. Defects in Perovskite-Halides and Their Effects in Solar Cells. *Nat Energy* **2016**, *1* (11), 1–13. https://doi.org/10.1038/nenergy.2016.149.
(160) Brus, V. V. Light Dependent Open-Circuit Voltage of Organic Bulk Heterojunction Solar Cells in the Presence of Surface Recombination. *Organic Electronics* **2016**, *29*, 1–6. https://doi.org/10.1016/j.orgel.2015.11.025.
(161) Vollbrecht, J.; Brus, V. V. On the Recombination Order of Surface Recombination under Open Circuit Conditions. *Organic Electronics* **2020**, *86*, 105905. https://doi.org/10.1016/j.orgel.2020.105905.
(162) Mohamad Noh, M. F.; Arzaee, N. A.; Safaei, J.; Mohamed, N. A.; Kim, H. P.; Mohd Yusoff, A. R.; Jang, J.; Mat Teridi, M. A. Eliminating Oxygen Vacancies in SnO2 Films via Aerosol-Assisted Chemical Vapour Deposition for Perovskite Solar Cells and Photoelectrochemical Cells. *Journal of Alloys and Compounds* **2019**, *773*, 997–1008. https://doi.org/10.1016/j.jallcom.2018.09.273.
(163) Zhang, F.; Ma, W.; Guo, H.; Zhao, Y.; Shan, X.; Jin, K.; Tian, H.; Zhao, Q.; Yu, D.; Lu, X.; Lu, G.; Meng, S. Interfacial Oxygen Vacancies as a Potential Cause of Hysteresis in Perovskite Solar Cells. *Chem. Mater.* **2016**, *28* (3), 802–812. https://doi.org/10.1021/acs.chemmater.5b04019.
(164) Abdi-Jalebi, M.; Andaji-Garmaroudi, Z.; Cacovich, S.; Stavrakas, C.; Philippe, B.; Richter, J. M.; Alsari, M.; Booker, E. P.; Hutter, E. M.; Pearson, A. J.; Lilliu, S.; Savenije, T. J.; Rensmo, H.; Divitini, G.; Ducati, C.; Friend, R. H.; Stranks, S. D. Maximizing and Stabilizing Luminescence from Halide Perovskites with Potassium Passivation. *Nature* **2018**, *555* (7697), 497–501. https://doi.org/10.1038/nature25989.
(165) Yang, J.-N.; Song, Y.; Yao, J.-S.; Wang, K.-H.; Wang, J.-J.; Zhu, B.-S.; Yao, M.-M.; Rahman, S. U.; Lan, Y.-F.; Fan, F.-J.; Yao, H.-B. Potassium Bromide Surface Passivation on CsPbI3-xBrx Nanocrystals for Efficient and Stable Pure Red Perovskite Light-Emitting Diodes. *J. Am. Chem. Soc.* **2020**, *142* (6), 2956–2967. https://doi.org/10.1021/jacs.9b11719.
(166) Abdi-Jalebi, M.; Andaji-Garmaroudi, Z.; Pearson, A. J.; Divitini, G.; Cacovich, S.; Philippe, B.; Rensmo, H.; Ducati, C.; Friend, R. H.; Stranks, S. D. Potassium- and Rubidium-Passivated Alloyed Perovskite Films: Optoelectronic Properties and Moisture Stability. *ACS Energy Lett.* **2018**, *3* (11), 2671–2678. https://doi.org/10.1021/acsenergylett.8b01504.
(167) Dong, Q.; Chen, M.; Liu, Y.; Eickemeyer, F. T.; Zhao, W.; Dai, Z.; Yin, Y.; Jiang, C.; Feng, J.; Jin, S.; Liu, S. (Frank); Zakeeruddin, S. M.; Grätzel, M.; Padture, N. P.; Shi, Y. Flexible Perovskite Solar Cells with Simultaneously Improved Efficiency, Operational Stability, and Mechanical Reliability. *Joule* **2021**, *5* (6), 1587–1601. https://doi.org/10.1016/j.joule.2021.04.014.
(168) Li, M.; Yang, Y.-G.; Wang, Z.-K.; Kang, T.; Wang, Q.; Turren-Cruz, S.-H.; Gao, X.-Y.; Hsu, C.-S.; Liao, L.-S.; Abate, A. Perovskite Grains Embraced in a Soft Fullerene Network

Make Highly Efficient Flexible Solar Cells with Superior Mechanical Stability. *Advanced Materials* **2019**, *31* (25), 1901519. https://doi.org/10.1002/adma.201901519.
(169) Yakubovsky, D. I.; Arsenin, A. V.; Stebunov, Y. V.; Fedyanin, D. Y.; Volkov, V. S. Optical Constants and Structural Properties of Thin Gold Films. *Opt. Express, OE* **2017**, *25* (21), 25574–25587. https://doi.org/10.1364/OE.25.025574.
(170) Zhang, X.; Qiu, J.; Qiu, J.; Qiu, J.; Li, X.; Li, X.; Zhao, J.; Zhao, J.; Liu, L.; Liu, L. Complex Refractive Indices Measurements of Polymers in Visible and Near-Infrared Bands. *Appl. Opt., AO* **2020**, *59* (8), 2337–2344. https://doi.org/10.1364/AO.383831.
(171) Collin, S.; Rousset, J.; Coutancier, D.; Yaiche, A.; Rives, S.; Jutteau, S.; Bodeux, R.; Raoult, E. Optical Characterizations and Modelling of Semitransparent Perovskite Solar Cells for Tandem Applications. *36th European Photovoltaic Solar Energy Conference and Exhibition* **2019**, 757–763. https://doi.org/10.4229/EUPVSEC20192019-3BV.2.53.
(172) Shalenov, E. O.; Seitkozhanov, Y. S.; Valagiannopoulos, C.; Ng, A.; Dzhumagulova, K. N.; Jumabekov, A. N. Performance Evaluation of Different Designs of Back-Contact Perovskite Solar Cells. *Solar Energy Materials and Solar Cells* **2022**, *234*, 111426. https://doi.org/10.1016/j.solmat.2021.111426.
(173) Anwar, F.; Mahbub, R.; Satter, S. S.; Ullah, S. M. Effect of Different HTM Layers and Electrical Parameters on ZnO Nanorod-Based Lead-Free Perovskite Solar Cell for High-Efficiency Performance. *International Journal of Photoenergy* **2017**, *2017*, e9846310. https://doi.org/10.1155/2017/9846310.
(174) Casas, G. A.; Cappelletti, M. A.; Cédola, A. P.; Soucase, B. M.; Peltzer y Blancá, E. L. Analysis of the Power Conversion Efficiency of Perovskite Solar Cells with Different Materials as Hole-Transport Layer by Numerical Simulations. *Superlattices and Microstructures* **2017**, *107*, 136–143. https://doi.org/10.1016/j.spmi.2017.04.007.

Appendix

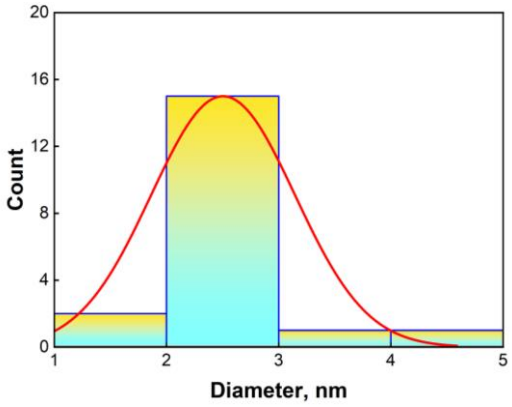

Figure A4.1: Particle size distribution diagram for SnO_2 QDs

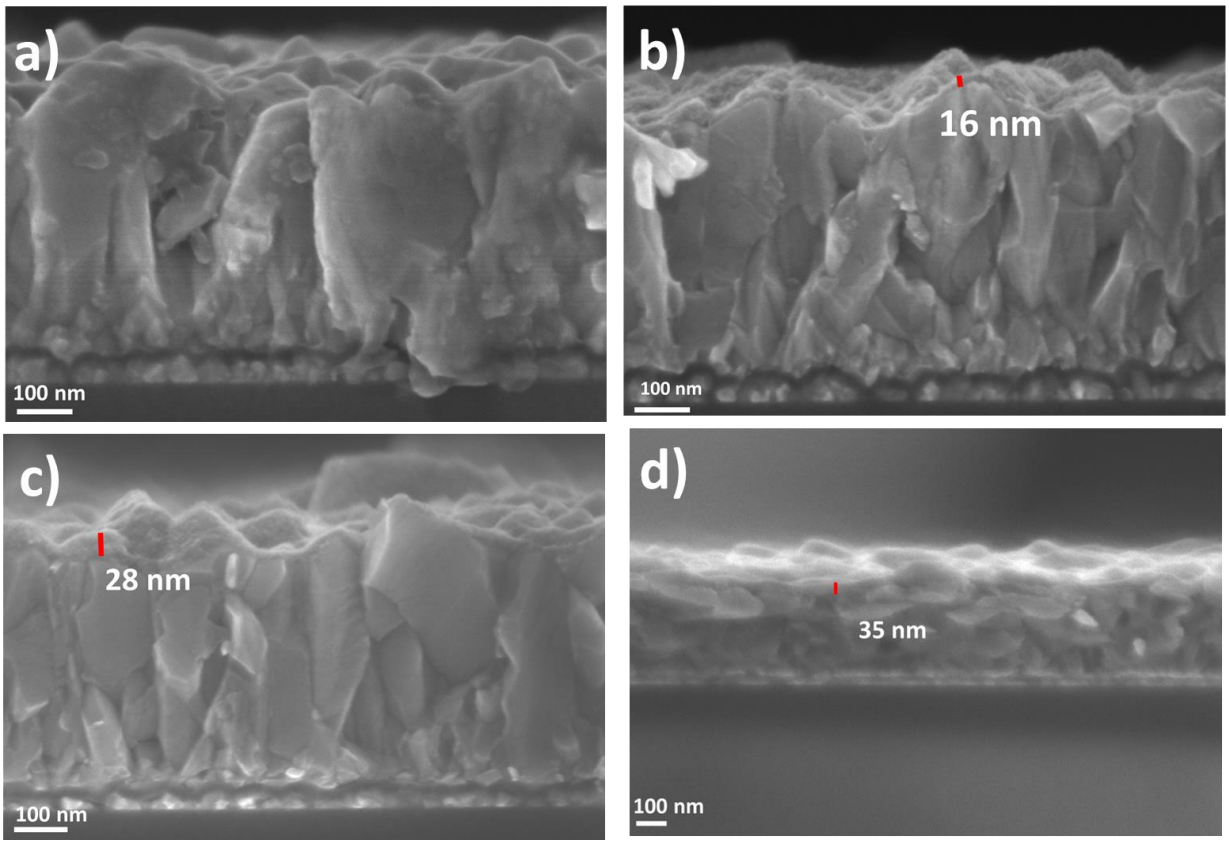

Figure A4.2: SEM cross-section images with (a) 1 wt%, (b) 1.5 wt%, (c) 2.5 wt%, and (d) 3 wt% SnO_2 QD based ETLs inks on glass/FTO

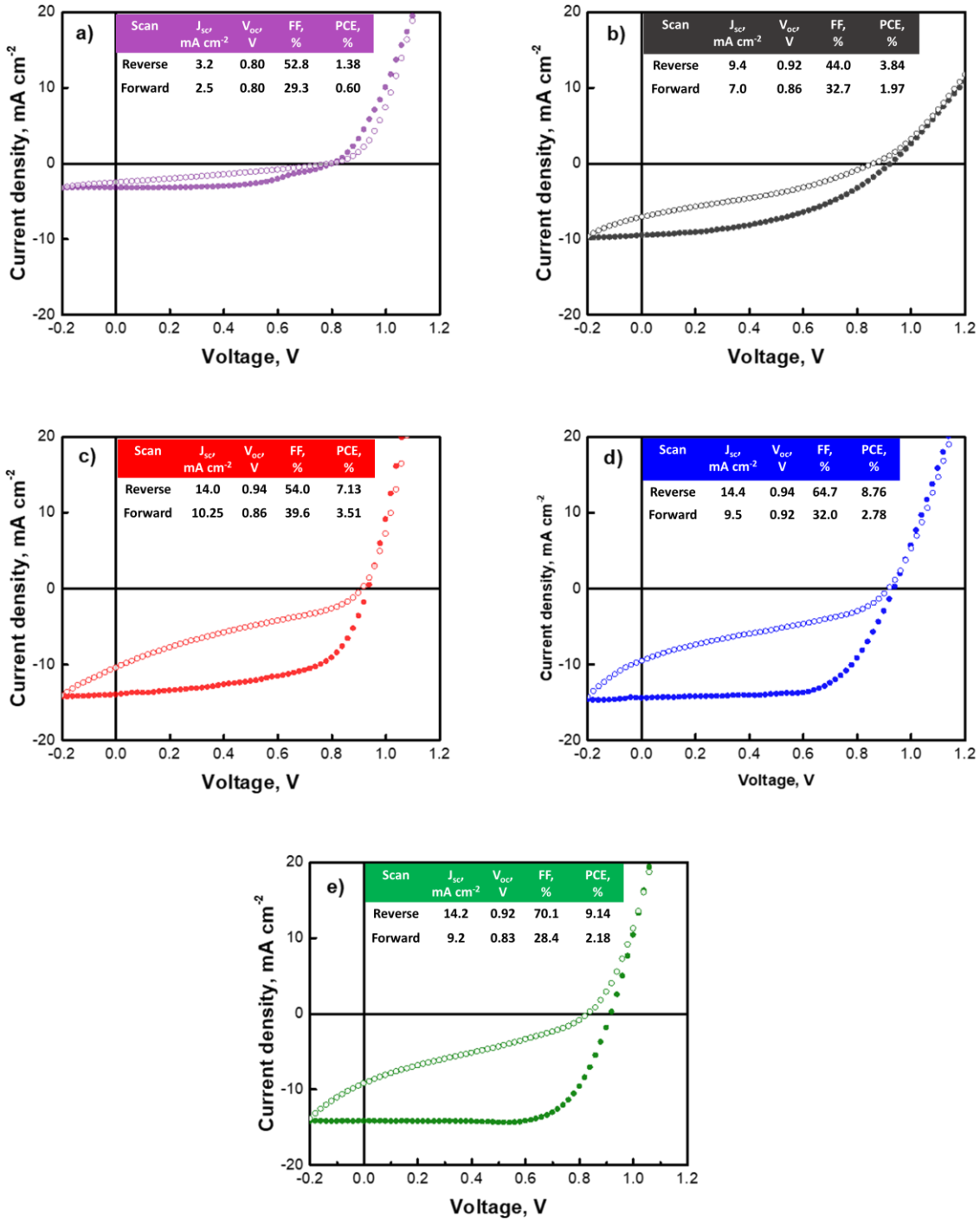

Figure A4.3: *J-V* curves of top-performing devices featuring (a) ETL0, (b) ETL1, (c) ETL2, (d) ETL4, and (e) ETL5

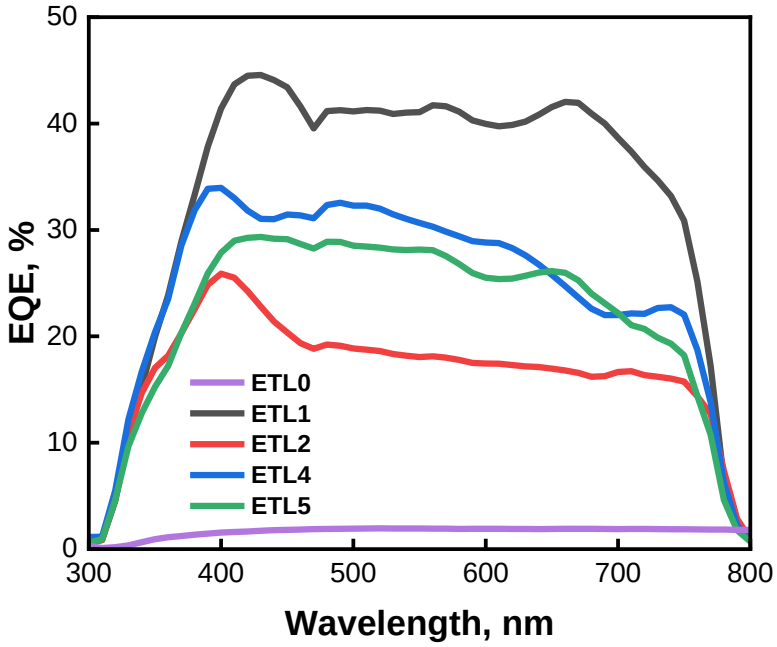

Figure A4.4: EQE spectra of champion devices with (a) ETL0, (b) ETL1, (c) ETL2, (d) ETL4, and (e) ETL5

Table A5.1: Slot-die coating parameters for fabrication of FPSC functional layers

Coating Parameters	**ETL**	**Perovskite**	**HTL**
Chuck Heating (°C)	25	25	25
Chuck Coating Speed (cm min^{-1})	130	80	80
Pump Rate (ml min^{-1})	0.35	0.15	0.15
Annealing Temperature (°C)	140	100	------
Annealing Time (min)	30	10	------
Coating Window	221	221-222	222-223

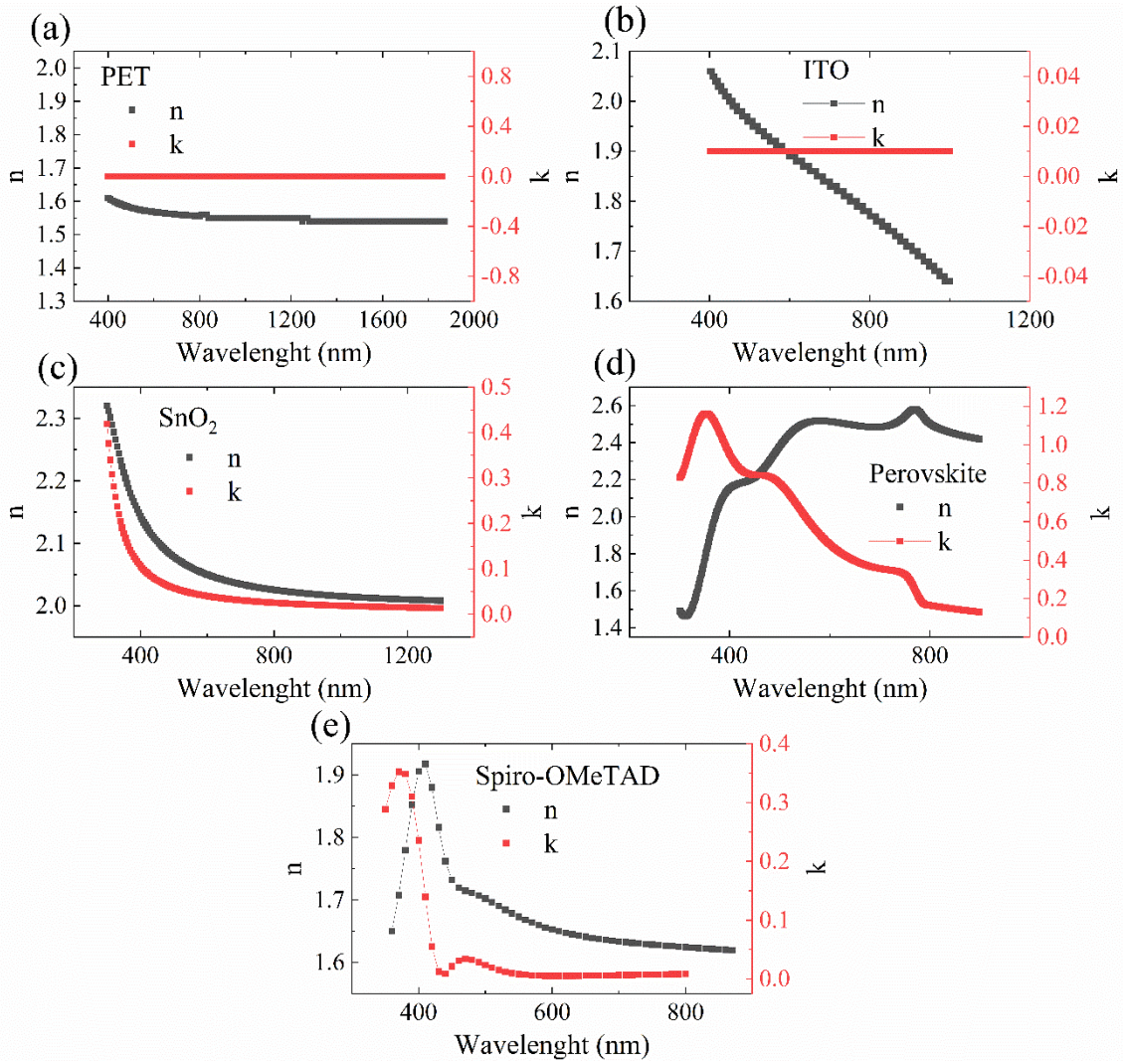

Figure A5.1: Spectral dependences of refractive index (*n*) and extinction coefficient (*k*) in PET, ITO, SnO_2, $MAPbI_3$, and Spiro-MeOTAD [169–171]

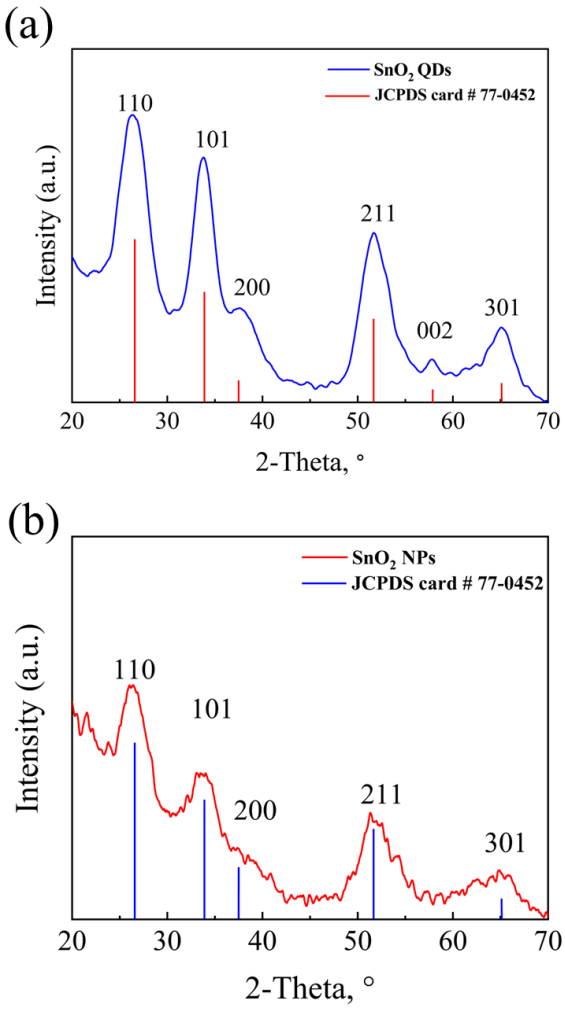

Figure A5.2: XRD patterns of SnO_2 (a) QDs and (b) NPs

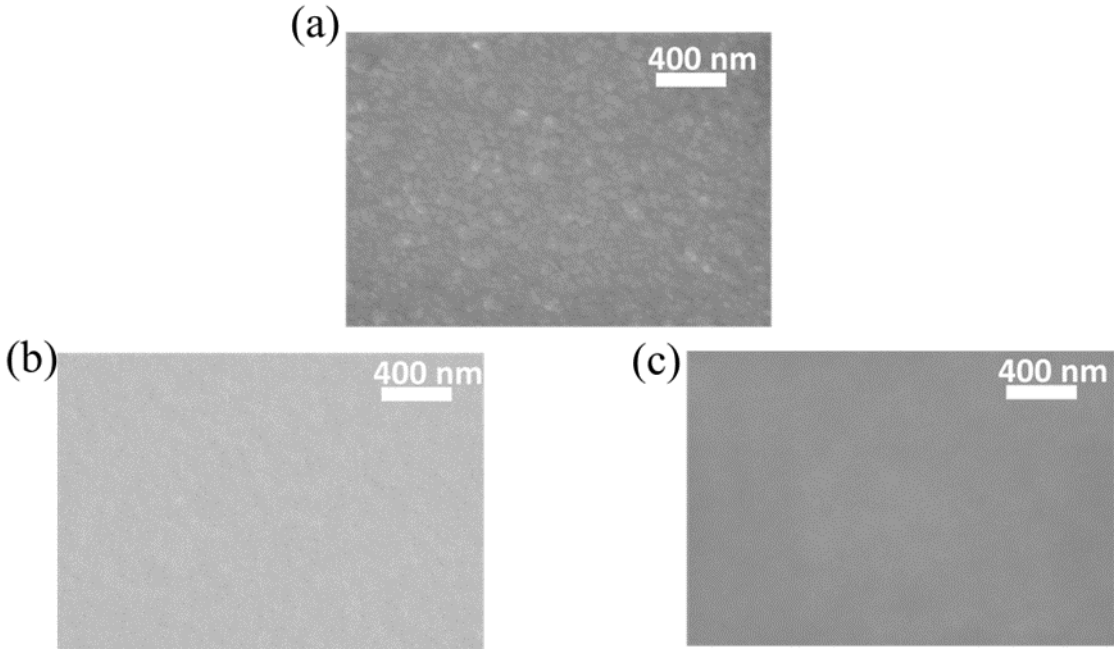

Figure A5.3: SEM top-view images of (a) PET/ITO, (b) SnO_2 QD-based ETL on PET/ITO, and (c) SnO_2 NP-based ETL on PET/ITO at 100 kX magnifications

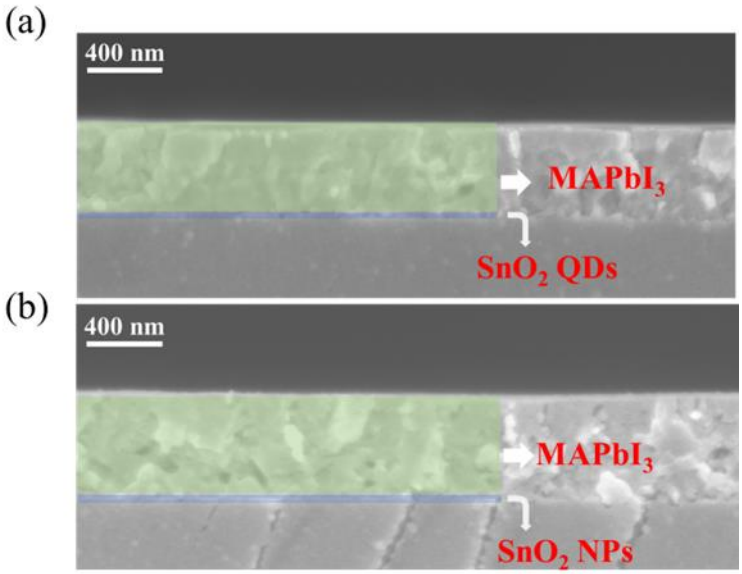

Figure A5.4: SEM cross-section images of FPSCs on glass with SnO_2 (a) QD- and (b) NP-based ETLs at 30 kX magnification

Table A5.2: Statistical values for solar cells performance parameters of 45 (each) well-performing FPSCs with SnO_2 QD- and SnO_2 NP-based ETLs

ETLs	Scan Direction	J_{sc} (mA cm^{-2})	V_{oc} (V)	FF (%)	PCE (%)	R_S (Ω cm^2)	R_{Sh} (kΩ cm^2)
SnO_2 QDs	Reverse	15.66 ± 1.08	0.94 ± 0.02	67.71 ± 3.32	9.98 ± 0.72	7.65 ± 0.75	3.73 ± 0.95
	Forward	13.91 ± 1.44	0.93 ± 0.02	50.00 ± 6.52	6.53 ± 1.20	11.28 ± 3.03	1.73 ± 0.11
SnO_2 NPs	Reverse	15.02 ± 0.95	0.92 ± 0.02	64.20 ± 3.50	8.89 ± 0.66	8.92 ± 1.23	3.00 ± 0.66
	Forward	13.99 ± 0.96	0.92 ± 0.03	55.59 ± 7.58	7.19 ± 1.19	10.56 ± 2.61	2.00 ± 0.52

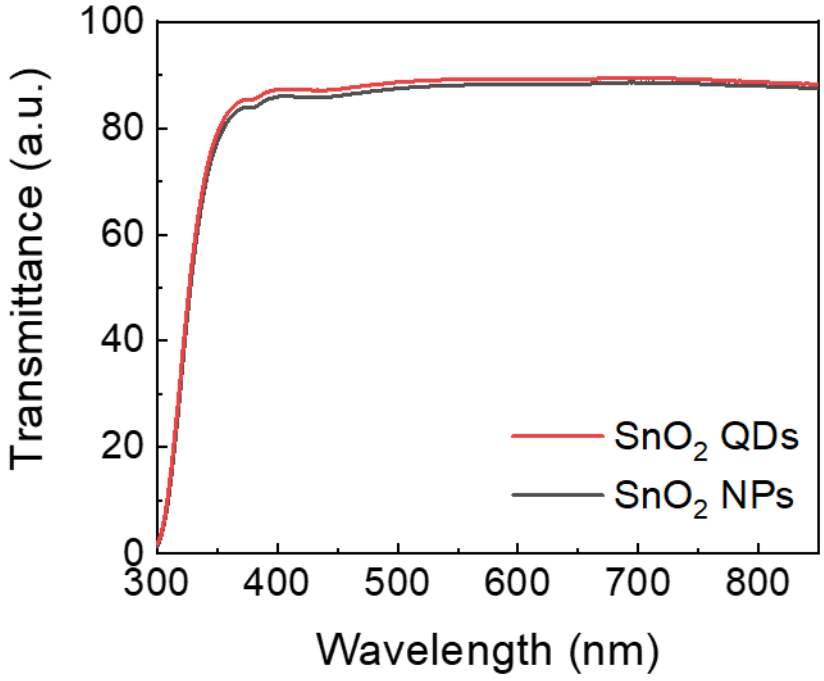

Figure A5.5: UV-Vis transmittance spectra of SnO_2 QD- and SnO_2 NP-based ETLs on glass

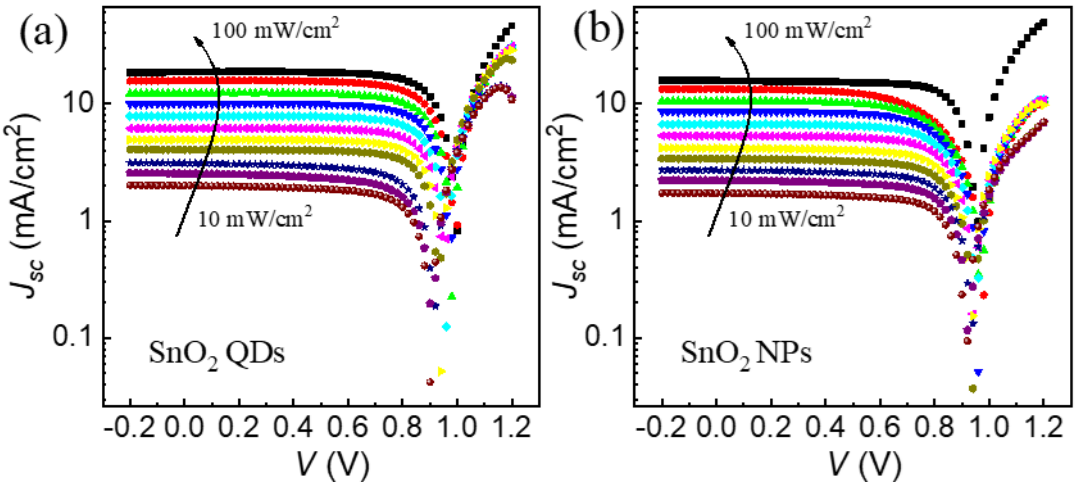

Figure A5.6: *J-V* curves of FPSCs with SnO_2 (a) QD- and (b) NP-based ETLs at varying light intensity

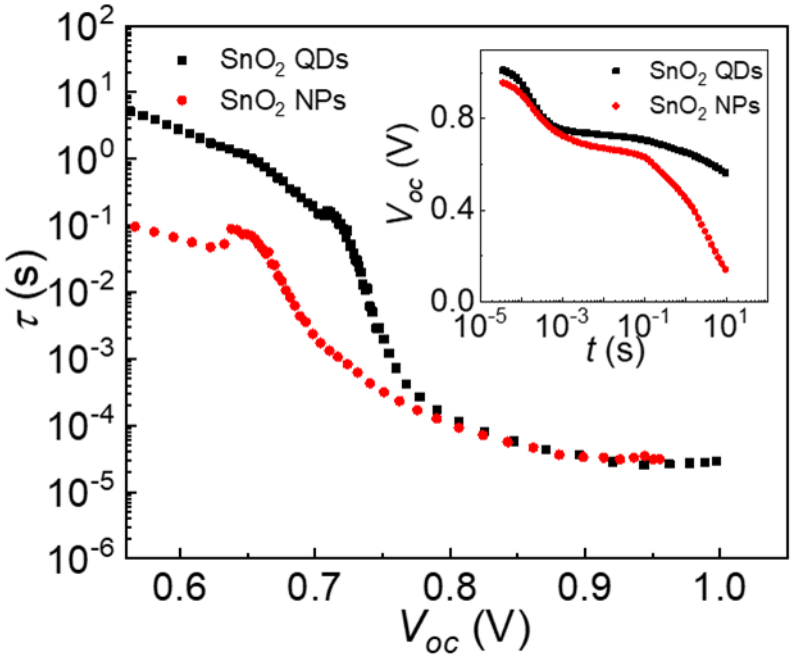

Figure A5.7: Dependences of charge carrier lifetime on V_{oc} in FPSCs with SnO_2 QD- and SnO_2 NP-based ETLs. The inset image shows the OCVD curves of devices

Table A5.3: Physical parameters of device functional layers used in numerical simulation experiments

Parameters	**ETL**		**Perovskite**		**HTL**	
	SnO_2 QDs	**SnO_2 NPs**	**SnO_2 QDs**	**SnO_2 NPs**	**SnO_2 QDs**	**SnO_2 NPs**
Electron lifetime (s)	-	-	3×10^{-5}	3×10^{-5}	-	-
Electron mobility ($cm^2\ V^{-1}\ s^{-1}$)	20 [172]	20 [172]	6.1×10^{-4}	6.4×10^{-4}	2×10^{-4} [173,174]	2×10^{-4} [173,174]
Hole mobility ($cm^2\ V^{-1}\ s^{-1}$)	10 [172]	10 [172]	6.1×10^{-5}	6.4×10^{-5}	2×10^{-4} [173,174]	2×10^{-4} [173,174]
Surface recombination speed ($cm\ s^{-1}$)	-	-	8.5×10^{2}	1×10^{3}	-	-
Acceptor concentration (cm^{-3})	0	0	1×10^{12}	1×10^{12}	8×10^{18}	8×10^{18}
Donor Concentration (cm^{-3})	1×10^{14}	1×10^{15}	0	0	0	0

The density of States in the conduction band (cm^{-3})	2.2×10^{18} [172]	2.2×10^{18} [172]	9×10^{17}	4.5×10^{18}	2.5×10^{18} [173]	2.5×10^{18} [173]
The density of States in the valance band (cm^{-3})	2.2×10^{19} [172]	2.2×10^{19} [172]	9×10^{21}	9×10^{21}	1.8×10^{19} [173]	1.8×10^{19} [173]
Relative permittivity	9 [172]	9 [172]	30 [172]	30 [172]	3 [173]	3 [173]
Band gap (V)	3.7 [172]	3.7 [172]	1.55 [172]	1.55 [172]	3.2 [173,174]	3.2 [173,174]
Electron affinity (V)	4.23 [172]	4.23 [172]	3.9 [172]	3.9 [172]	2.1 [173]	2.1 [173]